The Hofstadter Butterfly and Quantum Interferences in Modulated 2-Dimensional Electron Systems

vorgelegt von

Martin C. Geisler

aus Viersen

Contents

List of Figures

Symbol table

a, b	Superlattice periods
$a_B^\star$	Effective Bohr radius
$\mathbf{A}(\mathrm{r}) = xB\mathbf{e}_y$	Vector field in the Landau gauge
A	Unit cell area of the modulation potential in real space
$A_{\mathrm{BZ}} = K_a^2$	Area of the first Brillouin zone
A_{F}	Area enclosed by an electron orbit in k-space
A_j	Area enclosed by electron orbit type j in k-space
A_{L}	Area enclosed by the lens shaped orbit in k-space
A_{QI}	Area enclosed by a quantum interference in k-space
$A_{\mathrm{SdH}} = \pi k_{\mathrm{F}}^2$	Area of the Fermi circle of the unmodulated system in k-space
α	Set of indices (k_x, k_y, j)
$\alpha_{\mathrm{V}} = |V_x^{\mathrm{eff}}|/|V_y^{\mathrm{eff}}|$	Ratio of effective potential strengths
α_0	Phase of cyclotron motion
$\alpha_{\mathbf{q}}$	Part of the Fourier component $V_{\mathbf{q}} = V_0 \cdot \alpha_{\mathbf{q}}$
$\mathbf{B} = B\mathbf{e}_z$	Magnetic field
B_0^{qm}	Critical magnetic field for tunneling in the quantum mechanical picture
B_0^{cl}	Critical magnetic field for tunneling in the classical picture
$c_\lambda(\alpha)$	Coefficients for the eigenstate of the magnetic lattice
$\mathbb{C}$	Set of complex numbers
d	Depth of etched nm-scale holes
D	Distance between the heterostructure surface and the 2DEG
$D(E)$	Density of states
$D_n(E)$	Density of states contribution of Landau level n
$\delta(\ldots)$	Delta distribution
$\Delta(1/B)$	$1/B$-periodicity
$\Delta(1/B)_j$	$1/B$-periodicity corresponding to orbit type j
$\Delta(1/B_{\mathrm{CO}})$	$1/B$-periodicity of the commensurability oscillation
$\Delta E_{\mathbf{q}}$	Energy gap

$\Delta\eta$	Electron phase difference due to tunneling
$\Delta\varphi$	Electron phase difference due to the magnetic flux
Δk_x, Δk_y, Δk	Uncertainty in k-space
$\Delta\rho$	Height of a commensurability peak
$\Delta\sigma_{\mu\mu}$	Band conductivity
Δx, Δy	Uncertainty in real space
e	Elementary charge
$\mathbf{E}$	Electrical field
E	Energy
$\tilde{E}$, $\tilde{E}_\alpha$	Normalized energy scale for the Hofstadter butterfly
$\hat{E}_{\mathbf{R}}$	Gauge transformation
E_C	Conduction band energy
E_F	Fermi energy
E_n	Landau level energy
E_z	Energy dispersion in growth direction
$\varepsilon(\mathbf{q})$	Dielectric constant
$\eta = \pi/(ak_F)$	Abbrevation, used in $A_L(k_F, a)$
η_{23}, $\eta_{2'3'}$	Electron phase due to tunneling
$\eta_V = V_0/E_F$	Dimensionless potential amplitude
F_L	Lorentz force
F_V	Force due to the modulation potential
$FFT(f(t))$	Fast Fourier transformation
$\varphi_{23}, \varphi_{2'3'}$	Electron phase due to the magnetic flux
φ_r, φ_t	Phase of reflected and transmitted waves
$\Phi = B \cdot A$	Magnetic flux through one superlattice unit cell
$\Phi_0 = h/e$	Flux quantum
Φ_C	Flux penetrating a cyclotron orbit
g	Minigap index
g_s	Spin degeneracy
Γ_0	Collision broadening of a Landau level
h	Planck's constant
$\hbar$	$h/2\pi$
$\hbar\omega_c$	Cyclotron energy
H	Hamiltonian
$\mathrm{Han}(t)$	Hanning function
$|\langle i|j\rangle|^2$	transition probabilities
I	Electrical current
I_0	Part of a transition probability
I_1	Amplitude of the oscillating part of a transition probability

I_{ON}	LED current variable
j, j'	Subband index
J_0	Bessel function of the first kind
$\mathbf{k} = (k_x, k_y)$	Wave vector in two dimensions
k_{F}	Fermi wave vector
K	Dimensionless Landau band coupling parameter
$K_a = 2\pi/a$	Reciprocal superlattice vector
$K_b = 2\pi/b$	Second reciprocal vector for a rectangular superlattice
k_a, k_b	Commensurability oscillation indices for rectangular superlattices
$l_{\mathrm{B}} = \sqrt{\hbar/eB}$	Magnetic length
L	Distance between the voltage probes of a Hall bar
L/W	Geometry factor
$L_n(X)$	Laguerre polynomial of order n
L_y	Sample size in y-direction
λ	Index of the commensurability oscillations
λ_{F}	Fermi wavelength
λ_{LED}	Wavelength
$\lambda_{\mathrm{mfp}} = v_{\mathrm{F}} \tau_{\mathrm{tr}}$	Mean free path
l, m	Index numbers
m^*	Effective mass
m_0	Free electron mass
$\hat{M}_{\mathbf{R}}$	Magnetic translation operator
μ	Electron mobility
n	Orbital quantum number
$|n, \alpha\rangle$	Eigenstates for the magnetic lattice
$|n, k_y + \lambda K_a\rangle$	Landau eigenstates
n_i	Number of subbands below a minigap
n_{L}	Landau level degeneracy
n_{Φ_0}	Flux quantum density
$n_{\mathbf{q}}^{\mathrm{tunnel}}$	Tunnel events over a gap with probability P_{q}
$n_{\mathbf{q}}^{\mathrm{non-tunnel}}$	Same for non-tunneling events
n_{s}	Electron density
n_x, n_y	Integer numbers for $\mathbf{q} = (n_x K_a, n_y K_b)$
$\mathbb{N}^+$	1,2,3,...
$\mathbb{N}$	0,1,2,...
$N(E)$	Filled states per unit area below the minigap at energy E
N_{subband}	Number of states per unit area in one subband
ν	Filling factor
ω_{c}	Cyclotron angular frequency

p, p_i	Number of flux quanta per q unit cells for $p/q = \Phi/\Phi_0$
q, q_i	p flux quanta per q unit cells for $p/q = \Phi/\Phi_0$
$\mathbf{p}$	Electron momentum
P, $P_\mathbf{q}(k_\mathrm{F}, K_a, V_0^2/B)$	Tunneling probability
P_{23}, $P_{2'3'}$	Single trajectory probability
$P_\mathrm{total}(B)$	Round-trip probability for an orbit
$p, p_{23}, p_{2'3'} \in \mathbb{C}$	Probability densities for tunneling events
$q \in \mathbb{C}$	Probability density for a non-tunneling event
$\Psi(\mathbf{r})$, $\Psi_{n,x_0,k_y}(\mathbf{r})$	Electron wave function
$\psi_{n,x_0}(x)$	Harmonic oscillator wave function
π_1, π_2	Periodicities of $1/B$ oscillations
$Q_\mathbf{q}(k_\mathrm{F}, K_a, V_0^2/B)$	Probability for absence of tunneling
$\mathbf{q} = (n_x K_a, n_y K_b)$	Reciprocal lattice vectors
$\mathbf{q}_1, \mathbf{q}_2$	Reciprocal lattice vectors of interference points
$q = \|\mathbf{q}\|$	Length of a reciprocal lattice vector
$\mathbf{q}_x = (K_a, 0)$	Special reciprocal lattice vectors
$\mathbf{q}_y = (0, K_b)$	
$\|r\rangle$	Reflected wave function
$\mathbf{r}(t)$	Classical electron trajectory
$\mathbf{r}_\mathrm{gc}(t)$	Guiding center motion
$\mathbf{r}_\mathrm{cyc}(t)$	Cyclotron motion
$\mathbf{R}, \mathbf{R}'$	Superlattice vector
$\mathbf{R} = (X, Y)$	Cyclotron orbit guiding center coordinate
R_c	Cyclotron radius
R_{xx}	Longitudinal resistance
R_{xy}	Hall resistance
$\hat{\rho}$	Resistivity tensor
ρ_0	Drude zero field resistivity
$\rho_{xx} = \rho_{yy}$	Longitudinal resistivity for an isotropic system
$\rho_{xy} = -\rho_{yx}$	Hall resistivity for an isotropic system
σ	Hall conductance contribution of a partially filled Landau band
$\hat{\sigma}$	Conductivity tensor
σ_Gauss	Gaussian width
σ_hl	Radius of etched nm-scale holes
$\sigma_{xx} = \sigma_{yy}$	Longitudinal conductivity for an isotropic system
$\sigma_{xy} = -\sigma_{yx}$	Hall conductivity for an isotropic system
$\sigma_{\mu\mu}^\mathrm{sc}$	Scattering conductivity
T	Temperature
$\|t\rangle$	Transmitted wave function

τ_0	Total quantum scattering time
τ_{tr}	Momentum relaxation time
$\hat{T}_{\mathbf{R}}$	Translation operator
$\theta_{\mathbf{q}}$	Incident Bragg scattering angle
$\mathbf{v}_{\text{avg}}$	Velocity of the guiding center
v_{F}	Fermi velocity
$\mathbf{v}_{\text{g}}$	Group velocity
V_0	Amplitude of the modulation potential
V_0^{cl}	Amplitude of the modulation potential, estimated using the classical picture for magnetic breakthrough
V_0^{qm}	Amplitude of the modulation potential, estimated using the quantum mechanical picture for magnetic breakthrough
$V(x), V(x,y), V(\mathbf{r})$	Modulation potential
V_x, V_y	Modulation potential amplitudes in x- and y-direction
$V_x(x), V_y(y)$	Modulation potentials in x- and y-direction
$V_{\text{eff}}(\mathbf{R})$	Effective potential of the guiding center drift model
$V_x^{\text{eff}}(B), V_y^{\text{eff}}(B)$	Effective modulation strengths
V_{B}	Schottky barrier
V_{G}	Gate voltage
$V_{\mathbf{q}}$	Fourier component of the modulation potential
V_{xx}	Longitudinal voltage
V_{xy}	Hall voltage
W	Hall bar width
w	Quantum number in the Diophantic equation
x_0	Center coordinate of the harmonic oscillator
$\chi(y)$	Normalized plane wave
x, y	Coordinates
X, Y	Cyclotron orbit guiding center coordinates
z	Coordinate orthogonal to the sample surface
$\mathbb{Z}$	Set of rational numbers

Abbrevations

1D	One-dimensional
2D	Two-dimensional
2DEG	Two-dimensional electron gas

ac	Alternating current
AFM	Atomic force microscope
BNSC	Boron nitride silicon carbide, material for crucibles
BZB	Brillouin zone boundary
CAD	Computer aided design
CGAL	Computational geometry algorithms library [1]
CO	Commensurability oscillations
dc	Direct current
DOS	Density of states
DX center	Defect present typically in III-V alloys when doped with n-type impurities
FFT	Fast Fourier transformation
LED	Light emitting diode
LEDA	Library of efficient data types and algorithms [2]
MBE	Molecular beam epitaxy
MIBK	Methyl iso-butyl ketone, electron beam resist developer
PMMA	polymethyl methacrylate, electron beam resist
SCBA	Self consistent Born approximation
SdH	Shubnikov-de Haas

1 Introduction

Imagine an artificial crystal in which all spatial degrees of freedom are modulated in a periodic fashion, just as in a real crystal, but with the added benefit of having full control over the periodicity and geometry of this modulation. Since lattice characteristics which are purely geometrical are the basis for many effects encountered in solid state physics, an artificial crystal would permit access to a whole class of physical effects which are difficult or even impossible to study using real crystals. The fabrication of an adequate 3D artificial crystal is still impractical, so researchers use two-dimensional electron systems on which a periodic 2D electric potential is superimposed [3–5]. Due to the reduced dimensionality, additional effects may arise, like strong electron-electron correlations or a different screening behavior. These will, however, not be considered here.

One effect expected for an artificial crystal is the formation of an **artificial miniband structure** as a result of the reduced size of the new Brillouin zone and the minigaps which emerge at the new Brillouin zone boundaries. Since the band structure determines the propagation of electrons inside a crystal, this may be used to tune transport and optical properties for a range of applications. Effects of this artificial band structure can be studied using magnetotransport: in a magnetic field, electrons participating in transport move on Fermi contours in k-space. Electrons on *closed* Fermi contours give rise to oscillations in the magnetoresistance with a periodicity characteristic of the area encircled by the electron [6]. For an unmodulated sample, Shubnikov-de Haas oscillations arise [7]. They correspond to the circular free-electron Fermi contour in k-space. Oscillations due to the smaller closed Fermi contours in an artificial band structure are, however, not easily observed in magnetotransport: When a finite magnetic field is applied, tunneling across the small energy gaps on the Brillouin zone boundaries, known as magnetic breakthrough, makes larger closed electron orbits possible by combining Fermi contour sections belonging to different occupied minibands. Such a larger orbit, characteristic of a 2D artificial modulation, was observed only recently [8] in a magnetotransport measurement. Here we revisit this effect and find a whole range of possible closed orbits, which demonstrates the high quality of our samples.

Another, hitherto unexplored, quantum mechanical effect in 2D artificial crystals is the **quantum interference** of a single electron wave after traveling along two different paths. In solid state physics, one can study this phenomenon by fabricating a mesoscopic, loop shaped Aharonov-Bohm interferometer [9]. There, the interfering electron paths are fixed in real space and consequently the area they enclose is also fixed. The phase difference an electron picks up along the two paths changes linearly with the applied magnetic field B. This leads to B-periodic magnetotransport oscillations. Could one "construct" such an interferometer in k-space? It would change its real space size with $1/B$ to stay constant in reciprocal space. This would lead to oscillations in $1/B$ in the magnetoresistance. Exactly such a system was found by Stark and Friedberg [10]. They observed $1/B$-periodic magnetoresistance oscillations due to a quantum interference in magnesium. By inspecting the Fermi surfaces of magnesium, they found the interfering paths responsible for the observed oscillation. These paths are weakly coupled by magnetic breakthrough across two small energy gaps of different size and on different Brillouin zone boundaries. A simpler interference than Stark and Friedberg's was observed for an artificially 1D-modulated sample [11–13], but was at first interpreted as a consequence of modulation-induced Landau level broadening. Only recently it was realized that it is also explainable by interferences in k-space [14]: The 1D modulation creates energy gaps only in one k-vector direction. The possible quantum interferences are limited to paths coupled by tunneling over gaps which have the same size and lie on the same Brillouin zone boundary. Due to this restriction, the interfering paths are easily spotted. The first observation of quantum interferences characteristic of a 2D artificial crystal is presented in this work: We found novel quantum interferences of paths which couple across two energy gaps of different size and/or position in k-space. This is also the case for the interference in the original paper of Stark and Friedberg. In contrast to their interference, where no intermediate tunneling is necessary, our interferometers, however, incorporate many tunneling events on each arm. To pick among the large set of possible interferometers the most probable ones, we developed a Monte Carlo simulation. Its output agrees largely with the experimental data. Using this simulation, we can examine the band structure and even think about designing interferometers in k-space by applying the necessary artificial modulation potential in real space.

Apart from the artificial band structure and its consequences, the artificial crystal lends itself to the study of other spectacular quantum mechanical effects, like the **Hofstadter butterfly spectrum**, which has been studied theoretically for half a century [15–18] and which was first plotted by Douglas Hofstadter in 1976 [19]. The butterfly is the pictorial representation of the fractal energy spectrum of a periodic 2D electron system in an external magnetic field. It is caused by the competition of two characteristic area scales: The area containing exactly one flux quantum $\Phi_0 = h/e$ and the unit cell of the artificial crystal. Unfortunately, the conditions for the Hofstadter butterfly are quite stringent: The

flux through one unit cell has to be of the order of the flux quantum, which amounts to magnetic fields $B > 60000\,\mathrm{T}$ for typical semiconductor lattices. Magnetic fields of this magnitude are unaccessible with today's facilities. So, one strategy has been to use artificial superlattices with a much larger unit cell, enabling in principle the observation of the butterfly at moderate fields of $B \approx 1\,\mathrm{T}$. This situation is equivalent to the *nearly free electron* case of a very weak modulation potential acting on a Landau quantized electron system [17, 20]: Each Landau level is broadened and subdivided into minibands according to the Hofstadter butterfly spectrum over an energy range proportional to the modulation potential strength. We only mention here that Hofstadter originally considered the opposite limit of a *tight binding* electron system in a relatively weak magnetic field. It can be shown, however, that both limits ultimately lead to the same energy spectrum [17]. Unfortunately, due to a lack in sample quality, the undisputed experimental observation of even the largest features in the Hofstadter butterfly remained elusive until recently [21, 22]. This observation was able to resolve the most prominent features associated with the butterfly spectrum. Here we go one step beyond that work and present an indication of the fractal properties of the spectrum, thanks to improvement in sample quality which increases the resolution by one order of magnitude. The unperturbed spectrum assumed above is, however, somewhat idealized: in reality, coupling of the Landau bands becomes important at lower magnetic fields, which may slightly distort or even rearrange the observed spectrum [23]. The improvements in sample quality mentioned above allow us to verify this rearrangement experimentally, and hence study the hitherto experimentally unexplored region away from the nearly free electron limit.

The guiding principle throughout this work was to bridge the gap between theory and experiment by comparing both side by side. The most important figures in this thesis feature direct comparisons of experimental data and theoretical calculations, which coincide surprisingly well.

The structure of the thesis is as follows:

- In *chapter 2*, we introduce the properties of an unmodulated two-dimensional electron system, along with the Quantum Hall Effect.

- In *chapter 3*, we present the fundamental concepts necessary to discuss 1D- and 2D-modulated 2D electron systems: the competition of two characteristic length scales, the modulation period and the magnetic length, leads to semiclassical commensurability oscillations in the longitudinal magnetoresistance of 1D-modulated samples. For the high magnetic field limit and a 2D modulation, this competition leads to a quantum mechanical phenomenon: the Hofstadter butterfly spectrum. We highlight its influence on magnetotransport measurements, in particular on the

quantized Hall conductance. For the weak magnetic field limit, we start with the miniband structure due to the artificial modulation and discuss Fermi contours and their modifications due to magnetic breakthrough. We describe how closed electron trajectories are manifested in magnetotransport.

- In *chapter 4*, we present the optimized sample fabrication procedure and measurement technique used for the various devices in this work.

- In *chapter 5*, the fractal Hofstadter butterfly energy spectrum is unveiled, using the quantized Hall conductivity as a probe. The long searched-for rearrangement and deformation of this spectrum due to Landau band coupling is presented.

- In *chapter 6*, quantum interferences characteristic of a 2D artificial crystal and the set of most probable electron orbits are measured and explained quantitatively for the first time. We use Fourier-transformed magnetotransport data for a range of electron densities to identify oscillations in comparison with Monte Carlo simulations which were developed in this work.

- In *chapter 7*, we vary the lattice geometry: both a smaller lattice period and a Lieb lattice are studied in light of quantum interferences. An unexpected avoided cross over of two oscillations is found. The sensitivity of the quantum interferences to the modulation potential shape is confirmed, and new interferences are discovered. In the second part, we verify a recent theoretical prediction for rectangular lattices experimentally. We observe a characteristic non-monotonic dependence of the commensurability oscillation amplitudes on the applied *B*-field, which is unknown for square lattices.

- We conclude in *chapter 8* with a summary and outlook.

- In the *appendices*, details of the sample fabrication, measurement and analysis are given.

Some of the results of this thesis have already been published:

- *Detection of Landau Band Coupling Induced Rearrangement of the Hofstadter Butterfly*, M. C. Geisler, J. H. Smet, V. Umansky, K. von Klitzing, B. Naundorf, R. Ketzmerick and H. Schweitzer, Physical Review Letters, **92**, 256801 (2004)

- *Detection of Landau band coupling induced rearrangement of the Hofstadter butterfly*, M. C. Geisler, J. H. Smet, V. Umansky, K. von Klitzing, B. Naundorf, R. Ketzmerick and H. Schweitzer, Physica E, **25**, 227 (2004)

- *Experimental Evidence for Predicted Magnetotransport Anomalies in Rectangular Superlattices*, M. C. Geisler, S. Chowdhury, J. H. Smet, L. H. Höppel, V. Umansky, R. R. Gerhardts and K. von Klitzing, Physical Review B, **72**, 045320 (2005)

2 The two-dimensional electron gas

As seen in the introduction, a possibility to create an artificial lattice is to start with a two-dimensional electron system and apply a modulation in the remaining two spatial degrees of freedom. In this work an $Al_xGa_{1-x}As$/GaAs heterostructure incorporating a two-dimensional electron gas (2DEG) is used as the starting point. Its composition and properties are the subject of the following chapter.

2.1   The heterostructure

The AlGaAs/GaAs heterostructure is produced by Vladimir Umansky at the Weizmann Institut of Science in Israel using molecular beam epitaxy (MBE). With MBE crystalline layers of different materials can be deposited onto a substrate with nearly atomic precision [24]. The layer sequence is depicted at the top of Fig. 2.1.

An $Al_{0.36}Ga_{0.64}As$ spacer is grown onto an (100)-GaAs substrate. While the lattices of GaAs and $Al_xGa_{1-x}As$ are nearly perfectly matched, the work functions and band gaps are different. Donors are introduced into the AlGaAs barrier layer using modulation doping. To this end a short superlattice of $Al_{0.36}Ga_{0.64}As$ quantum wells with AlAs barriers and Si-delta doping is grown. Electrons will move from the silicon doped layers to the energetically lower lying states in the GaAs and create a confinement potential at the heterostructure interface as shown in the bottom of Fig. 2.1. This potential at the heterostructure interface, which must be calculated by solving the Schrödinger and Poisson equations self-consistently, quantizes the electron motion in the growth direction, so only two spatial degrees of freedom are left [25].

Since the donors are spatially separated from the heterostructure interface and since the sample is grown in an MBE chamber with excellent hight vacuum, electron scattering in

δ–doped
Al$_{0.36}$Ga$_{0.64}$As   AlAs   Growth direction

GaAs   Al$_{0.36}$Ga$_{0.64}$As   GaAs

9nm   8nm   10nm   25nm
cap   modulation   spacer
              doping

E

E$_F$

silicon   Z   first subband
δ–doping

E$_c$
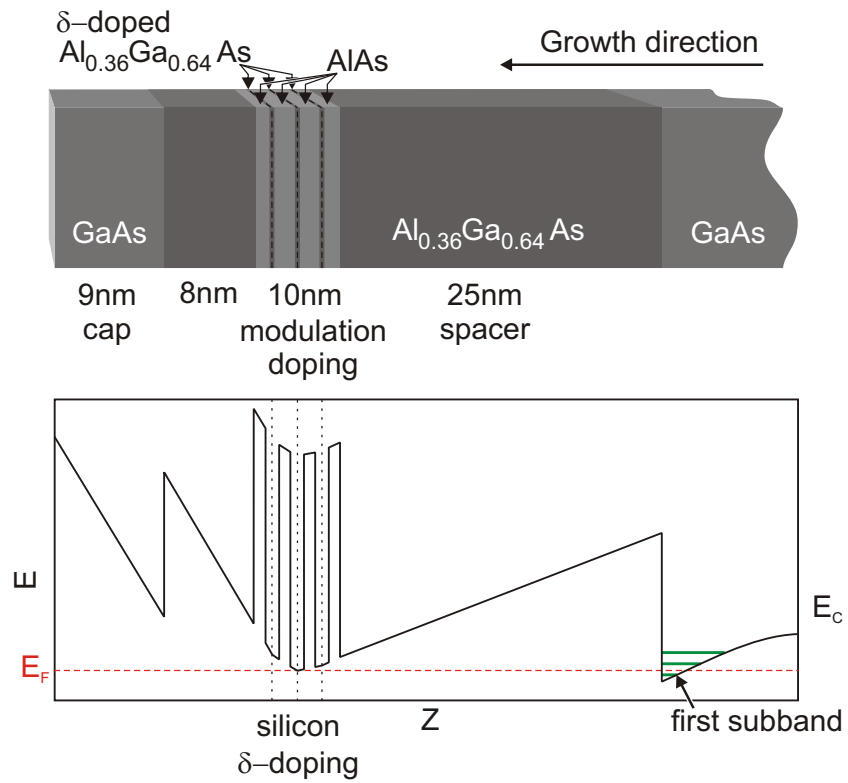
Figure 2.1:
Top figure shows the growth sequence of heterostructure #5-74, which was mainly used in this work. Below is a schematic of the conduction band profile. At $T = 0$ all states up to the Fermi energy E_F are occupied. E_F lies such that only the lowest subband is occupied.

the 2DEG is small. When illuminating the sample, a small parallel conduction layer may appear in the quantum wells containing the dopants. These parallel conduction layers screen the donor potential and further reduce scattering. High mobilities on the order of $3.4 \cdot 10^6 \text{cm}^2/\text{Vs}$ are achieved in this way, which are needed in the experiments presented in the later chapters.

The layer of $\text{Al}_{0.36}\text{Ga}_{0.63}\text{As}$ closest to the top surfaces reduces leakage when using a gate. Finally the structure is capped with GaAs to avoid oxidization of the AlGaAs layers underneath when the sample is exposed to air.

2.2   Properties of the 2DEG

As already mentioned above, the electron motion is quantized in the z-direction. For low temperatures and electron densities, only the lowest subband is occupied as depicted in Fig. 2.1. So a two-dimensional electron gas in the strict sense of the word is formed with the energy dispersion

$$E = \frac{\hbar^2 k_\text{x}^2 + \hbar^2 k_\text{y}^2}{2m^*} + E_\text{z} \, , \tag{2.1}$$

in the effective mass approximation. Here E_z is the energy of the first subband and (k_x, k_y) is the wave vector. In the conduction band of GaAs the electrons have a mass $m^* = 0.067 m_0$, with m_0 being the free electron mass. At $T = 0$, all states within the contour of constant energy E_F are occupied. Each state is doubly degenerate due to the spin degree of freedom. The electron density may then be written as

$$n_\text{s} = \frac{m^*}{\pi \hbar^2} (E_\text{F} - E_\text{z}) \, . \tag{2.2}$$

The density of states $D(E)$ is constant and reads

$$D(E) = \frac{\text{d}n_\text{s}}{\text{d}E} = \frac{m^*}{\pi \hbar^2} \, . \tag{2.3}$$

The Fermi wavevector takes on the form

$$k_\text{F} = \sqrt{2\pi n_\text{s}} \tag{2.4}$$

and can be used to calculate the Fermi wavelength

$$\lambda_\text{F} = \frac{2\pi}{k_\text{F}} \, . \tag{2.5}$$

The latter is a fundamental length scale in the problem. For instance to observe quantum mechanical effects due to an applied modulation potential, the modulation period a should to be of the order of λ_F.

2.3   The 2DEG in a magnetic field

In an external, homogeneous magnetic field, $\boldsymbol{B} = B\boldsymbol{e}_z$, perpendicular to the 2DEG the classical orbit of an electron with energy E_F is the circular cyclotron orbit with radius

$$R_c = l_B^2 k_F \tag{2.6}$$

and angular frequency $\omega_c = eB/m^*$. Here, l_B is referred to as the magnetic length and a characteristic length scale in the system:

$$l_B = \sqrt{\frac{\hbar}{eB}} \ . \tag{2.7}$$

Quantum mechanically, the magnetic field quantizes the electron energy spectrum into equidistant Landau energy levels as shown in Fig. 2.2 [26]. They result when solving the time independent Schrödinger equation $H_{\text{hom}}\Psi(\boldsymbol{r}) = E\Psi(\boldsymbol{r})$ in the presence of a magnetic field. In this case, the Hamiltonian reads

$$H_{\text{hom}} = \frac{1}{2m^*}(\boldsymbol{p} + e\boldsymbol{A})^2 \ . \tag{2.8}$$

We will use the Landau gauge $\boldsymbol{A} = xB\boldsymbol{e}_y$. With this gauge, the canonical momentum p_y is a constant of motion and we may look for solutions of the form $\Psi(\boldsymbol{r}) = \chi(y)\psi(x)$ with $\chi(y)$ being a normalized plane wave $L_y^{-1/2}\exp(ik_y y)$. Here, L_y is the sample size. The problem reduces to a solution of

$$\left[-\frac{\hbar}{2m^*}\frac{\partial^2}{\partial x^2} + \frac{m^*\omega_c^2}{2}(x - x_0)^2 \right] \psi_{n,x_0}(x) = E_n \psi_{n,x_0}(x) \ , \tag{2.9}$$

for $\psi_{n,x_0}(x)$. This is a harmonic oscillator equation centered around $x_0 = -l_B^2 k_y$. It has the eigenenergies

$$E_n = \hbar\omega_c \left(n + \frac{1}{2} \right) \ . \tag{2.10}$$

The eigenfunction corresponding to Landau level n with energy E_n encompasses an area with radius

$$R_c = l_B \sqrt{2n+1} \, , \qquad (2.11)$$

which is identical to the classical cyclotron radius 2.6. Each Landau level is $n_L = g_s n_{\Phi_0} = g_s eB/h$-fold degenerate as E_n is independent of the center coordinate x_0 or k_y. The system is assumed spin degenerate, so $g_s = 2$. In experiment, spin is only resolved at $B > 1.1$ T for the samples at hand. So we can write the density of states as

$$D(E) = n_L \sum_n \delta(E - E_n) \, . \qquad (2.12)$$

Here the Landau levels enter as δ-distributions with a distance $\hbar \omega_c$ in energy. The number of filled Landau levels for a certain electron density n_s is given by the *filling factor*,

$$\nu = \frac{g_s n_s}{n_L} = \frac{h n_s}{eB} \, . \qquad (2.13)$$

It decreases with increasing magnetic field as illustrated in Fig. 2.2(a-c). When crossing an even integer filling factor $\nu/2 \in \mathbb{N}^+$, the partially filled level is completely depopulated and the Fermi energy E_F jumps to the next lower level, creating the sawtooth behavior indicated in red in the lower panel of Fig. 2.2.

At exact even filling, all Landau levels below the Fermi energy are completely filled, so no excitation within a Landau level is possible. Hence the energetically lowest lying excitation is the one of an electron from the uppermost filled Landau level to the next higher empty level. The Fermi energy lies in a real density of states gap. With disorder, this gap turns into a mobility gap only, as we will see next.

2.3.1 Effects of disorder

The coulomb potential of the randomly distributed donor atoms and other sources of disorder in a sample lead to potential fluctuations. These modify the density of states in Eqn. 2.12 to a continuously varying function of the energy, which has maxima around the center of Landau levels at half filling and minima in between (Fig. 2.2c'). As a second effect of the potential fluctuations, only a part of the electronic states can extend their wavefunction across the whole sample. They are called *extended states* and are found whenever a Landau level is half filled. The remaining states are *localized states* [27]. The energy ranges where only localized states are available represent a mobility gap [28]. This mobility gap reappears together with the minima in the density of states periodically
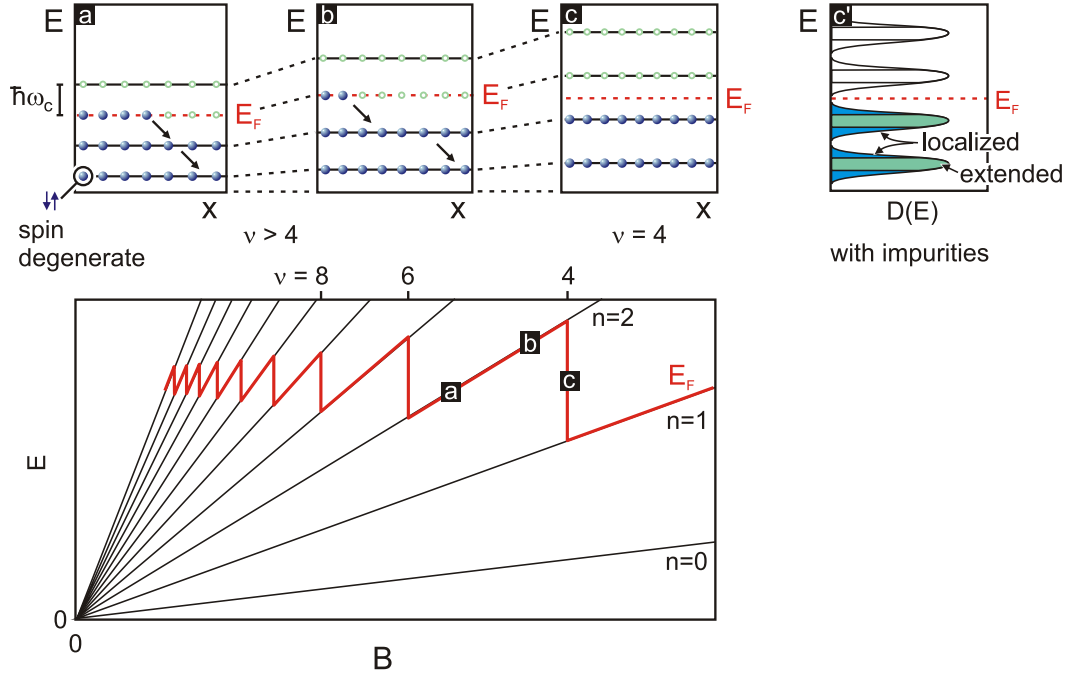
Figure 2.2:
   (a)-(c): Landau levels are depopulated with increasing magnetic field. Bottom: The Landau fan chart with Fermi energy in red. The positions of the top graphs are marked with a-c. The picture is valid assuming spin degeneracy. (c'): Disorder broadened Landau levels. Around even integer filling, the Fermi energy lies in a mobility gap.

around even integer filling factors. Using Eqn. 2.13 this periodicity can be expressed in $1/B$,

$$\Delta\left(\frac{1}{B}\right) = \frac{e}{hn_{\text{s}}} \; . \tag{2.14}$$

The oscillating density of states and the reappearing mobility gap have important consequences for the magnetotransport quantities ρ_{ij} as discussed in the next section.

2.4 Transport measurements

In the course of this thesis it will become apparent that modifications in the density of states, quantum interferences and topological effects due to the applied modulation poten-

tial are observable in the magnetotransport properties. The starting point for a transport measurement is a 2DEG shaped into a Hall bar with width W as displayed in the inset of Fig. 2.3. A current I is driven through the sample and both the longitudinal voltage V_{xx} and Hall voltage V_{xy} are measured. The distance between adjacent potential probes is equal to L. The geometry independent specific resistivities are

$$\rho_{xx} = R_{xx}/(L/W) \quad \text{and} \tag{2.15}$$
$$\rho_{xy} = R_{xy}. \tag{2.16}$$

They can be calculated from the measured voltages as $R_{xx} = V_{xx}/I$ and $R_{xy} = V_{xy}/I$. The Hall conductivity σ_{xy} in Fig. 2.3 is obtained from the measured resistivities via an inversion of the resistivity tensor $\hat{\rho}$

$$\sigma_{xy} = (\hat{\rho}^{-1})_{xy} = \frac{-\rho_{yx}}{\rho_{xx}\rho_{yy} - \rho_{xy}\rho_{yx}} \approx \frac{\rho_{xy}}{\rho_{xx}^2 + \rho_{xy}^2}. \tag{2.17}$$

The above equation is exact for isotropic systems for which ρ_{xx} equals ρ_{yy} and for which the Onsager-Casimir principle [29–31] holds with $\sigma_{xy} = -\sigma_{yx}$ and hence $\rho_{xy} = -\rho_{yx}$.

We will now discuss the ρ_{xx}- and σ_{xy}-behavior expected for unmodulated two-dimensional electron gases. Neglecting Landau quantization, the longitudinal resistivity reads

$$\rho_{xx} = \frac{1}{n_s e \mu}, \tag{2.18}$$

in the Drude model [32, 33] and does not depend on B. The Hall resistivity linearly increases with B

$$\rho_{xy} = \frac{B}{en_s}. \tag{2.19}$$

Formula 2.18 is used to determine the mobility $\mu = e\tau_{tr}/m^*$ of the sample. τ_{tr} is the momentum relaxation time of an electron at the Fermi energy. From the mobility the transport mean free path

$$\lambda_{mfp} = v_F \tau_{tr} = \frac{\hbar k_F \mu}{e} \tag{2.20}$$

can be estimated. Here we used the Fermi velocity $v_F = \hbar k_F/m^*$. For the modulated devices in this work, the mean free path is $\lambda_{mfp} = 35 \, \mu m$ after illumination. This is even larger than the sample width of $20 \, \mu m$. The unmodulated samples have a larger mean free path of $\lambda_{mfp} = 49 \, \mu m$ after illumination.

2.4.1 Shubnikov-de Haas oscillations

As stated in section 2.3, due to Landau quantization the density of states at the Fermi energy, $D(E_F)$, is oscillating in $1/B$ for a fixed electron density n_s. This affects the longitudinal transport resistivity ρ_{xx}: Current transport along the applied electric field in a perpendicular magnetic field is possible only if electrons scatter between different eigenstates $\Psi_{n,x_0,k_y}(\boldsymbol{r})$. At low temperatures, the occupied initial and the empty final state of the scattering process have to be at the Fermi energy. Thus the number of such scattering events is proportional to the square of the density of states at E_F. The same is true for the longitudinal conductivity found using the self consistent Born approximation (SCBA) as in Refs. [34–36]. When simplified for the case of short range scatterers and for $T \rightarrow 0$, it reads

$$\sigma_{\mu\mu}^{sc}(E_F, T = 0) = \frac{e^2}{\hbar} \sum_n (2n+1) \left[2\pi l_B^2 D_n(E) \Gamma_0 \right]^2 . \tag{2.21}$$

Here, $D_n(E)$ is the density of states contribution of Landau level n and Γ_0 is the collision broadening. This longitudinal conductivity and thus also the longitudinal resistivity ρ_{xx} share the same $1/B$-oscillatory behavior as $D(E_F)$. These are the *Shubnikov-de Haas oscillations* (SdH) [7] observed in the ρ_{xx} trace of Fig. 2.3. For high enough magnetic fields, ρ_{xx} will even drop to zero (in Fig. 2.3 for $B > 1$ T) in the limit $T \rightarrow 0$ and the longitudinal transport becomes dissipationless.

The Shubnikov-de Haas oscillations are used to determine the electron density in experiment. They can also be accounted for when imposing the Bohr-Sommerfeld quantization rule [37] on the closed cyclotron orbits of electrons. The flux $\Phi_C = \pi R_c^2 B$ penetrating a cyclotron orbit must be an integer multiple of a flux quantum. Using equation 2.6 and 2.7 this transforms into an oscillation period

$$\Delta \left(\frac{1}{B} \right) = \frac{2\pi e}{\hbar} \frac{1}{A_F} . \tag{2.22}$$

Here, $A_F = \pi k_F^2$ is the area enclosed by the cyclotron orbit in k-space. The oscillation period in equation 2.22 is identical to the one found in equation 2.14.

2.4.2 Quantum Hall effect

Using Eqns. 2.13, 2.19 and 2.17, the classical Hall conductivity can be rewritten as

$$\sigma_{xy} = \nu \cdot e^2 / h . \tag{2.23}$$

When the Shubnikov-de Haas minima approach zero ($\rho_{xx} \rightarrow 0$) near even integer filling factors, the Hall conductivity deviates from the classical result (2.23) and is instead quantized for a finite ν-region to the integer multiple of e^2/h. The resulting plateaus in σ_{xy} can be seen in Fig. 2.3. The quantized plateau conductance is independent of sample properties like geometry, electron density and sample material. This quantization of the Hall conductance in connection with a vanishing longitudinal resistivity is the celebrated *Quantum Hall effect* [38].

To explain the finite width of the plateaus, several models exist. Many rely on the localized states introduced in section 2.3.1: In the Kubo-formalism, where conductivities are calculated as the linear response to an external field, the conductivity σ_{xx} is governed only by states at the Fermi energy, while for σ_{xy} all states below the Fermi energy contribute. However, the localized states do not contribute to the transport at zero temperature. Thus σ_{xx} and consequently ρ_{xx} vanish if E_F is between two Landau levels, where only localized states are available. At the same time σ_{xy} is constant with a quantized value. If, however, the Fermi energy moves through extended states, σ_{xx} is finite and σ_{xy} changes.

Irrespective of the model used for the conductivity, Laughlin was even able to demonstrate that the Hall conductivity quantization is a general consequence of gauge invariance and the existence of a mobility gap [28].

Other models rely on edge channels which arise due to the bending of Landau levels to higher energies at the sample edges [39, 40]. Each of the ν filled Landau levels produces a dissipationless one-dimensional edge channel where it crosses the Fermi energy. When the Fermi energy is between two Landau levels in the bulk, it lies in the region of localized states. So an applied current can only flow in the dissipationless edge channels and backscattering across the bulk is suppressed [41]. The voltage drop between potential probes on the same side of a sample is zero and so is ρ_{xx}. The voltage drop due to the fact that each edge channel contributes a conductivity e^2/h can be measured between the two sample sides as Hall voltage. This translates again to a quantization of σ_{xy} to a plateau for the range of localized states in the bulk.

The above models are however not consistent with recent measurements of the potential distribution in Hall samples using atomic force microscopy [42]. Newer work which is consistent with these experiments does not rely on localization but only on screening effects and the inhomogeneity due to the electron-depletion regions near the sample edges: Siddiki *et al.* [36] point out that screening effects create incompressible strips, in which the Fermi level is in a Landau gap. No elastic impurity scattering is possible there and locally σ_{xx} will vanish for low temperatures. Hence an applied current will flow in these incompressible strips. This leads to a vanishing longitudinal and quantized Hall
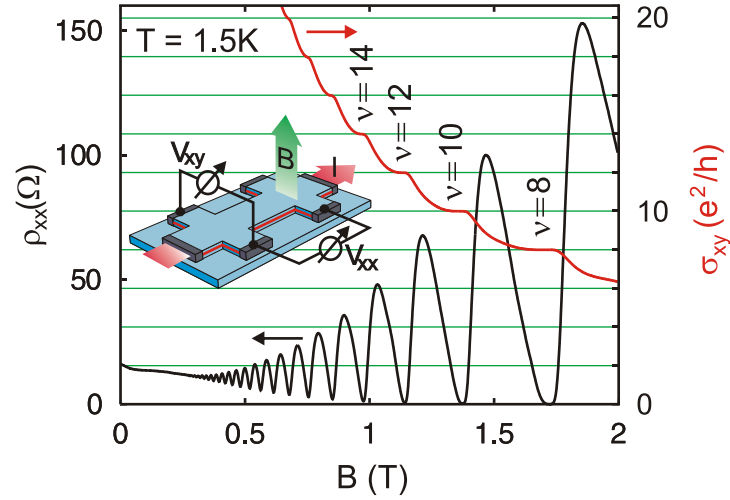
Figure 2.3:
The measured longitudinal resistivity ρ_{xx} and the Hall conductivity σ_{xy} (calculated from ρ_{xx} and ρ_{xy}) of a 2D electron gas are plotted versus the magnetic field. ρ_{xx} shows Shubnikov-de Haas oscillations first and at higher fields the integer Quantum Hall effect. σ_{xy} is quantized near even integer filling factors ν in units of $2e^2/h$. Inset: A Hall bar sample with applied current I and exposed to a perpendicular magnetic field B. Both the longitudinal voltage V_{xx} and the Hall voltage V_{xy} are measured to obtain ρ_{xx} and ρ_{xy}.

conductances as long as such an incompressible strip exists in the sample. This model differs from the edge channel picture since at most one incompressible strip exists at each sample side. Also, the current is transported in the same direction on both sample sides. When no incompressible strip is present, the current is flowing through the bulk of the sample.

3 The modulated two-dimensional electron gas

Quantum mechanical and semiclassical commensurability effects arise when a 2D electron gas is simultaneously exposed to a periodic modulation potential with strength V_0 and a uniform perpendicular magnetic field B. These effects originate from the competition of two length scales, namely the modulation period and the magnetic length. In this chapter this problem will be studied for a weak modulation potential $V_0 \ll E_F$ and in two limiting cases: (1) the strong magnetic field limit for which the Landau quantized electron system is weakly perturbed by a modulation potential $(V_0 \ll \hbar\omega_c)$ and (2) the weak magnetic field case $(\hbar\omega_c \ll V_0)$ where the field perturbs the miniband structure produced by the applied modulation.

Typical magnetotransport data for a modulated sample are shown in Fig. 3.1. Compared to the unmodulated sample in Fig. 2.3 many additional features are visible. In particular, three regions are of interest for this chapter: The positive magnetoresistance around $B = 0$, the quantum interferences for weak magnetic fields and the Hofstadter Butterfly for stronger magnetic fields. In this chapter, we will lay out the theoretical basis to treat each of these regions in the remaining chapters in more detail.

3.1   Strong magnetic field regime

In strong magnetic fields, a weak one-dimensional periodic modulation potential broadens the discrete Landau levels into bands. For a two-dimensional modulation these bands are subdivided further into subbands and minigaps that result in the Hofstadter Butterfly.
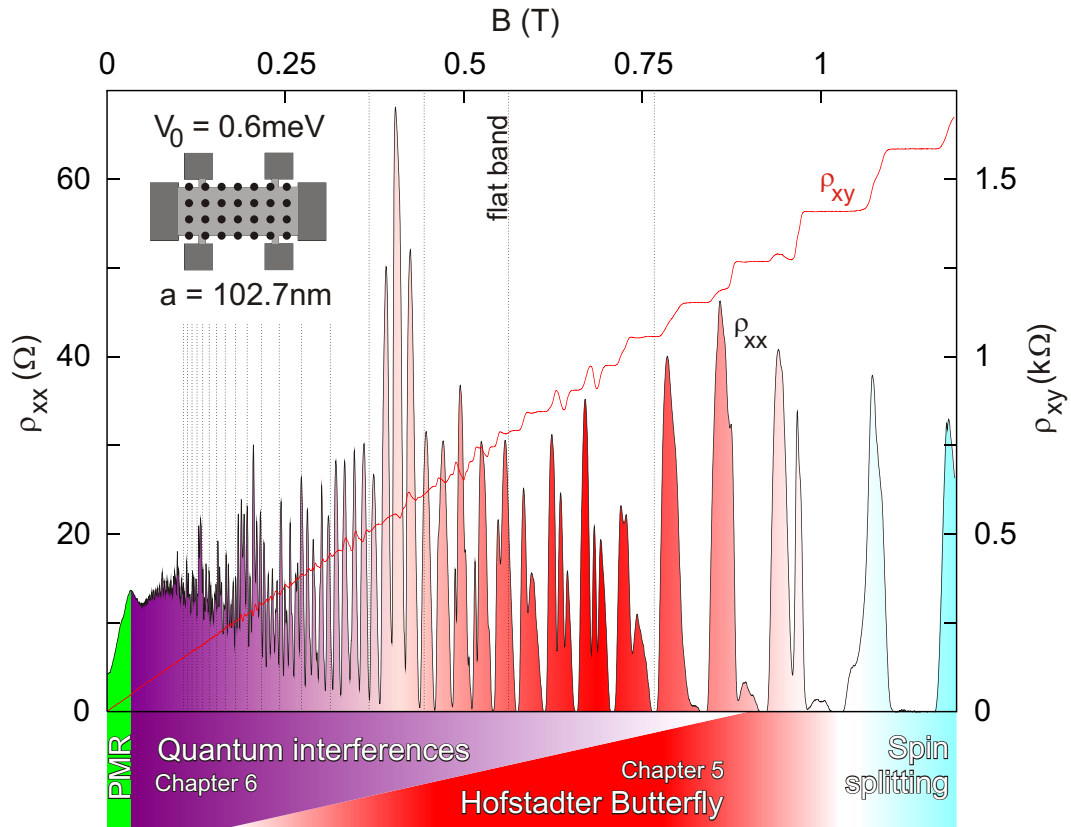
Figure 3.1:

The longitudinal and Hall resistivities for a modulated sample with period 102.7 ± 0.5 nm. The electron density is $n_s = 4.32 \cdot 10^{11} \text{cm}^{-2}$. The inset shows the sample geometry. Spin splitting is only resolved at higher magnetic fields $B > 1$ T (as indicated with the blue color). The positive magnetoresistance (green; section 3.2.5), the quantum interference region (magenta; section 3.2.1 and chapter 6), the Hofstadter butterfly region (reg; section 3.1.2 and chapter 5) and the flat band conditions (dotted; section 3.1.1) are discussed in more detail in the text.

3.1.1 Commensurability oscillations

The commensurability oscillations are visible in experiments on samples with one-dimensional modulation for both high ($\hbar\omega_c \gg V_0$) and low B-fields ($\hbar\omega_c \ll V_0$). Here they are however introduced using an approach only valid in the high field limit. This approach is useful in the later discussion of effects for two-dimensional modulations.

When the Landau quantized two-dimensional electron system is subjected to a weak ($V_0 \ll E_F$ and $V_0 \ll \hbar\omega_c$) one-dimensional modulation of the form

$$V(x) = (V_0/2)\cos(K_a x) \tag{3.1}$$

with $K_a = 2\pi/a$, the macroscopic degeneracy of the Landau states is lifted as displayed in Fig. 3.3b. The Landau levels with orbital index $n = 0, 1, \ldots$ are broadened into bands and the energy of the corresponding states,

$$E_n(x_0) = \hbar\omega_c \left(n + \frac{1}{2}\right) + \frac{1}{2}V_0 \cos(K_a x_0) e^{-\frac{1}{4}K_a^2 l_B^2} L_n\left(\frac{1}{2}K_a^2 l_B^2\right) , \tag{3.2}$$

now depends on the center coordinate $x_0 \in [0; a]$ (cf. Fig. 3.3b). In this expression, $L_n(X)$ is the Laguerre polynomial of order n and $\hbar\omega_c$ is the cyclotron energy. The resulting Landau bands are depicted in Fig. 3.2b. They have a magnetic field dependent oscillatory width. This width shrinks to zero whenever $L_n(\frac{1}{2}K_a^2 l_B^2) = 0$. At these fields the original degeneracy is restored. For a Landau band with index n, the Laguerre polynomial has exactly n zeroes. These are called the *flat band conditions*. They can be approximated for large n by

$$2R_c = a\left(\lambda - \frac{1}{4}\right) \tag{3.3}$$

with $\lambda \in \mathbb{N}^+$. The maximal bandwidth is obtained when $2R_c = a(\lambda + \frac{1}{4})$.

The corresponding eigenstates give rise to a *band conductivity* contribution $\Delta\sigma_{yy}$ [13,43–46], as the group velocity in the direction of the equipotential lines of the modulation potential,

$$\mathbf{v}_g = -\frac{1}{m^*\omega_c}\frac{dE_n}{dx_0}\hat{\mathbf{e}}_y = \frac{1}{\hbar}\frac{dE_n}{dk_y}\hat{\mathbf{e}}_y , \tag{3.4}$$

is no longer zero. This additional conductivity $\Delta\sigma_{yy}$ adds to the usual *scattering conductivity* σ_{yy}^{sc} of the unperturbed Landau states. The longitudinal resistivity ρ_{xx} is enhanced accordingly:

$$\rho_{xx} = \frac{\sigma_{yy}}{\sigma_{xx}\sigma_{yy} - \sigma_{xy}\sigma_{yx}} \approx \frac{\sigma_{yy}}{\sigma_{xy}^2} . \tag{3.5}$$
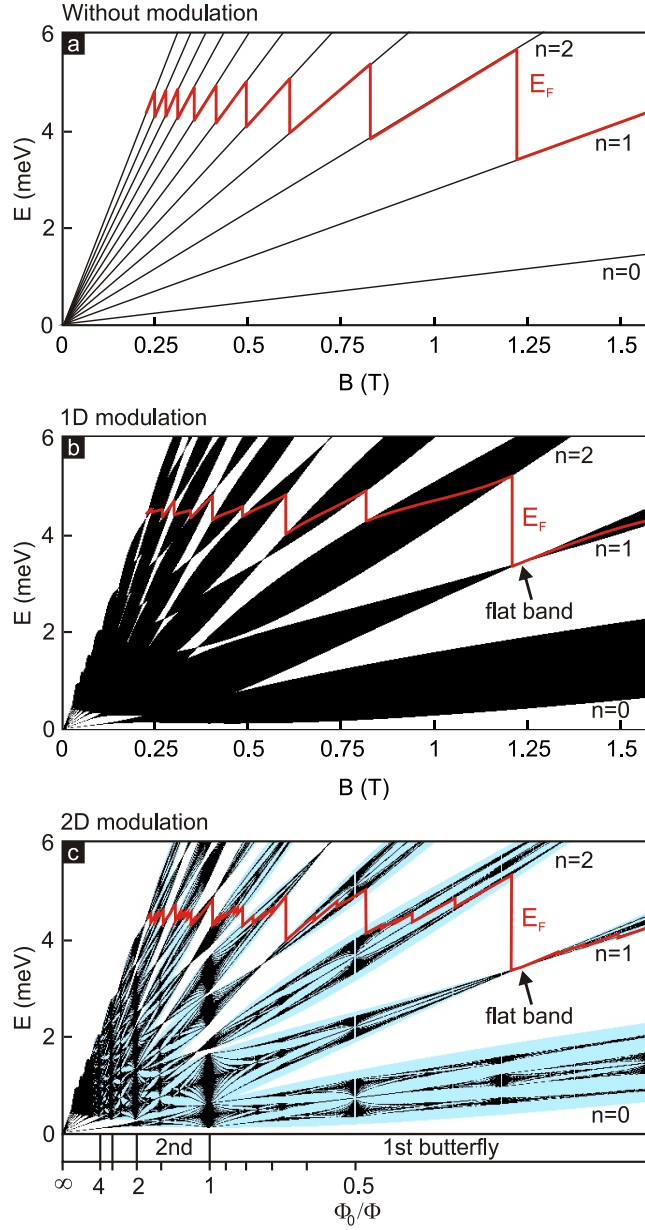
Figure 3.2:
  (a) The Landau fan chart of an unmodulated system. The red line shows E_F for a fixed electron density as a function of B. (b) Same as a) but in presence of a weak 1D modulation potential. Landau levels are broadened into bands with vanishing bandwidth only at the flat band conditions. (c) light blue: again the Landau bands of b). black: The Landau fan for a 2D weak ($V_0 = 0.15$ meV) modulation with period $a = 100$ nm in the single band approximation. The Landau bands break up into repeated Hofstadter butterflies. Additional jumps in E_F are present due to the internal structure. For low B both b) and c) are unphysical since $V_0 \ll \hbar\omega_c$ does not hold and thus the single band approximation is not applicable: E.g. no gaps are expected for $B < 0.25$ T, rather all Landau bands are vigorously mixed by coupling effects.
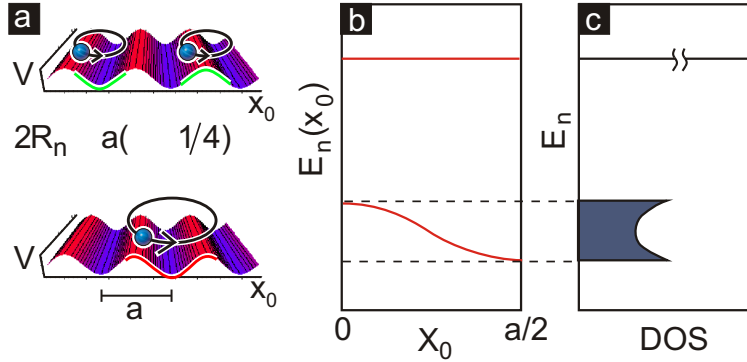
Figure 3.3:
a) Top: For the flat band condition $2R_c = a(\lambda - 1/4)$ the modulation potential average over one cyclotron orbit is independent of x_0. Bottom: The average is changing with x_0. b) The dispersion relation in the top panel is degenerate. c) The resulting density of states. Van-Hove singularities arise due to the flat dispersion at $x_0 = 0, a/2$.

Hence, the oscillatory Landau band width results in $1/B$-periodic ρ_{xx}-oscillations often referred to as *commensurability* or Weiss *oscillations* (CO) [11, 12].

The scattering conductivity on the other hand describes the electron transport in the direction of the applied electric field as a result of disorder-induced scattering of electrons. We know from section 2.4.1 that this scattering is increased for a large density of states at the Fermi energy. The density of states is maximal at flat band as seen in Fig. 3.3c. At these positions the scattering conductivity $\sigma_{\mu\mu}^{sc}$ and thus the longitudinal resistivity is increased. The resulting commensurability oscillations in $\rho_{\mu\mu}$ are in antiphase with the band conductivity commensurability oscillations.

The resistivity ρ_{xx} is dominated by the band conductivity so that the antiphase commensurability oscillations can only be seen in ρ_{yy}, where no band conductivity contribution needs to be considered, since the corresponding $\Delta\sigma_{xx}$ is zero. Both types of commensurability oscillations have been observed in experiment [11, 13].

For a two-dimensional modulation potential,

$$V(x,y) = \frac{V_0}{4}\left[\cos(K_a x) + \cos(K_a y)\right] , \tag{3.6}$$

additional intricate quantum mechanical effects arise. They will be the subject of the next section.

3.1.2   Hofstadter Butterfly

The energy spectrum of a two-dimensional periodic quantum system has a sensitive dependence on the magnetic flux $\Phi = B \cdot A$ through the periodic unit cell with area $A = a^2$. This is a consequence of the competition of the two characteristic area scales of the system, the unit cell area A and the area Φ_0/B one flux quantum $\Phi_0 = h/e$ occupies. These area scales are in frustration but one can solve for the spectrum whenever they are commensurable, that is their ratio Φ/Φ_0 is a rational number p/q corresponding to p flux quanta per q unit cells, with p and q being natural numbers which share no common factor. Additionally, the modulation potential has to be in either the strong ($V_0 \gg E_F$ and $V_0 \gg \hbar\omega_c$) or weak limit ($V_0 \ll E_F$ and $V_0 \ll \hbar\omega_c$).

The first case is the *tight binding limit*. In its simplest manifestation the electron energy spectrum consists of one cosine band. An applied weak perpendicular magnetic field splits this band into subbands. The number of subbands and their degeneracy depends sensitively on the ratio Φ/Φ_0 [16, 17, 17, 19, 47].

The second limit is the so called *nearly free electron* case. Fig. 3.2c displays the modifications to the discrete Landau level spectrum induced by a 2D periodic potential if coupling among Landau levels is neglected. A weak one-dimensional modulation lifts the macroscopic degeneracy of each Landau level and broadens it to a band with a field dependent bandwidth as discussed in the previous section. When a modulation in the second direction is added, this Landau band again splits as displayed in Fig. 3.2c due to the additional Bragg scattering. The resulting subbands are governed by the inverse ratio $\Phi_0/\Phi = q/p$ [17, 20].

For both limits the allowed states, plotted against Φ/Φ_0 for the tight binding limit or Φ_0/Φ for the nearly free electron case as abscissa, form the appealing *Hofstadter butterfly spectrum* in Fig. 3.4. The spectrum is fractal. It emerges in a variety of contexts.

To observe this spectrum experimentally, the tight binding limit is not suitable, since it is applicable to situations where the conduction band at the Fermi energy is energetically well separated from all other bands. Although the semiconductor crystal, which has a lattice constant of the order of Ångstroms, produces well separated bands at the Fermi energy, the static magnetic fields of 30 T available to experimentalists correspond only to a flux $\Phi \approx 10^{-4}\Phi_0$ per unit cell. The Hofstadter spectrum on the other hand is best visible around $\Phi/\Phi_0 = 1/2$. This flux ratio is attainable for an artificial superlattice modulation with period $a \approx 100$ nm at a moderate magnetic field of 0.8 T. It is however very difficult to realize a strong artificial modulation with sufficiently high uniformity.
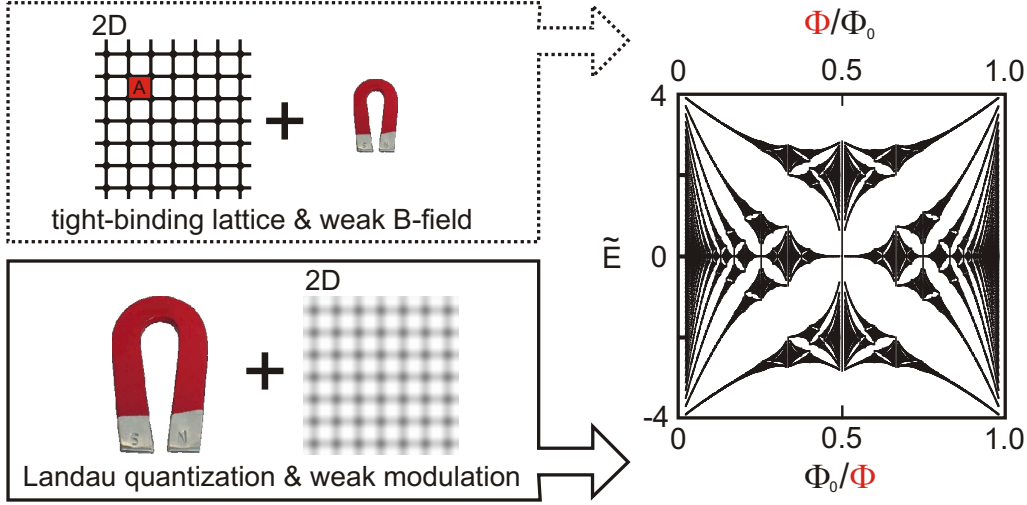
Figure 3.4:

The Hofstadter butterfly energy spectrum for both limiting cases. The abscissa is Φ/Φ_0 for the tight binding limit and Φ_0/Φ for nearly free electrons. The allowed values $\tilde{E}$ will be explained later in the context of Eqn. 3.10.

The nearly free electron limit on the other hand is experimentally accessible in weakly modulated 2DEGs and will be exclusively considered in the following. To get an understanding of the band splitting in this limit, the symmetries of the single-electron Hamiltonian

$$H = \frac{1}{2m^*}\left[\mathbf{p} + e\mathbf{A}\left(\mathbf{r}\right)\right]^2 + V\left(\mathbf{r}\right) \tag{3.7}$$

of the modulated system in a magnetic field are determined as described in [48,49]. As in Eqn. (2.8), the Landau gauge will be used. We consider the square modulation potential (3.6), which is weak enough to ensure that coupling of Landau bands can be neglected. This modulation potential is invariant under a translation $\mathbf{R} = l \cdot a\mathbf{e}_x + m \cdot a\mathbf{e}_y$ by multiple superlattice periods ($l, m \in \mathbb{N}$). The corresponding translation operator

$$\hat{T}_{\mathbf{R}} = exp\left(\frac{i}{\hbar}\mathbf{R}\cdot\mathbf{p}\right) \tag{3.8}$$

does not commute with the Hamiltonian H of the system since the translation $\hat{T}_{\mathrm{R}}$ shifts the argument of the vector field $\mathbf{A}(\mathbf{r} + \mathbf{R})$. This is a pure quantum mechanical effect. It can be compensated for by a subsequent gauge transformation $\hat{E}_{\mathbf{R}} = exp\left[\frac{ie}{\hbar}\mathbf{r}\cdot\mathbf{A}(\mathbf{r})\right]$. The combined *magnetic translation operator* [48, 50, 51] $\hat{M}_{\mathbf{R}} = \hat{E}_{\mathbf{R}}\hat{T}_{\mathbf{R}}$ then commutes with the Hamiltonian H. This magnetic translation operator generally does not commute with itself, but gives rise to an additional phase, for instance
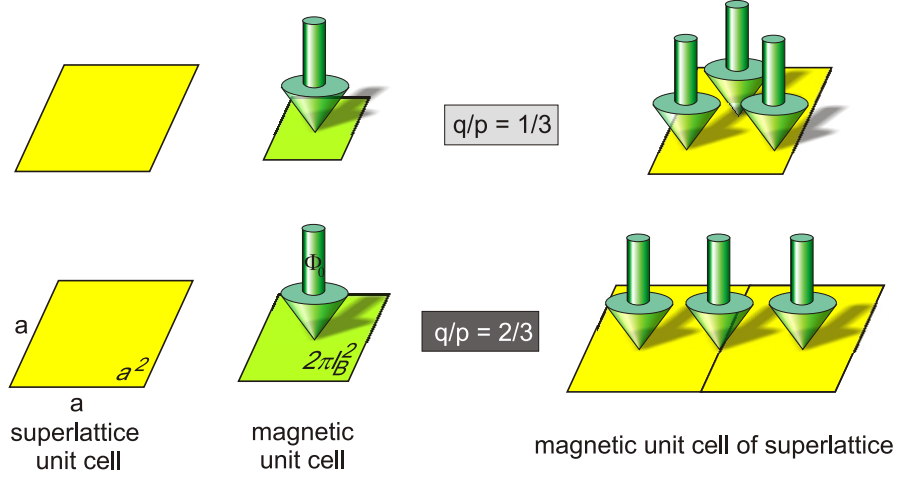
Figure 3.5:
 Examples of how the superlattice unit cell and magnetic unit cell form a magnetic unit cell of the superlattice.

$\hat{M}_{a\mathbf{e}_x}\hat{M}_{a\mathbf{e}_y} = \hat{M}_{a\mathbf{e}_y}\hat{M}_{a\mathbf{e}_x}\exp(-i2\pi\Phi/\Phi_0)$ for the translations along the two basis vectors of the superlattice. One can write this as $\hat{M}_{a\mathbf{e}_x}\hat{M}_{a\mathbf{e}_y}\hat{M}_{a\mathbf{e}_x}^{-1}\hat{M}_{a\mathbf{e}_y}^{-1} = \exp(-i2\pi\Phi/\Phi_0)$, so a translation of the wavefunction around a square with sidelength a produces an additional phase equal to the number of magnetic flux quanta through this square multiplied by 2π. This is the well-known Aharonov-Bohm effect [52]. Nevertheless, one can define for a rational flux ratio $\Phi/\Phi_0 = p/q$ a corresponding *magnetic lattice* with a q-times enlarged unit cell which is penetrated by an integer number of p flux quanta Φ_0. Examples for this are given in Fig. 3.5. For all translations $\mathbf{R}' = n \cdot (qa)\mathbf{e}_x + m \cdot a\mathbf{e}_y$ on this magnetic lattice the magnetic translation operator commutes with itself, since the additional phase is simply a multiple of 2π. We can then choose eigenfunctions $|n,\alpha\rangle$ which simultaneously diagonalize H and $\hat{M}$ and obey the periodic boundary condition enforced by the magnetic lattice. These are found in the course of Ref. [49] to be coupled Landau states $|n,k_y + \lambda K_a\rangle$ with center coordinates shifted by integer multiples of $l_B^2 K_a$, so they can be written as

$$|n,\alpha\rangle = \sum_{\lambda=-\infty}^{\infty} c_\lambda(\alpha)|n,k_y + \lambda K_a\rangle. \tag{3.9}$$

These eigenstates are classified by the corresponding Landau level index n and the set of quantum numbers $\alpha = (k_x, k_y, j)$ with the vector $\mathbf{k}$ defined in the magnetic Brillouin zone and a subband index $j = 1,\ldots,p$. Thus for a certain flux ratio $\Phi/\Phi_0 = p/q$ each Landau band splits into p subbands, which are separated by minigaps and can be shown to be q-fold degenerate [53]. For the simple potential (3.6) the coefficients $c_\lambda(\alpha)$ are

independent of *n* and are given by *Harpers equation* [15, 17, 53–55]

$$\frac{1}{2}V_0\cos(\lambda l_{\mathrm{B}}^2 K_a^2 - K_a x_0)c_\lambda(\alpha) + \frac{1}{4}V_0[c_{\lambda+1}(\alpha) + c_{\lambda-1}(\alpha)] = -\tilde{E}_\alpha c_\lambda(\alpha). \quad (3.10)$$

This equation can be solved for the values of $\tilde{E}_\alpha$ which range from -4 to 4. Their allowed values $\tilde{E}$ for a certain Φ_0/Φ are precisely what the Hofstadter spectrum in Fig. 3.4 shows. Thus the eigenenergies (3.2) take for the two-dimensional case the form

$$E_n = \hbar\omega_{\mathrm{c}}(n + \tfrac{1}{2}) + \frac{1}{8}V_0\tilde{E}\mathrm{e}^{-\frac{1}{2}\pi\Phi_0/\Phi}L_n(\,\pi\Phi_0/\Phi)\,, \quad (3.11)$$

as depicted in Fig. 3.2c. Note that the Hofstadter butterfly is an internal structure common to all Landau bands, independent of their orbital index *n*, since the $c_\lambda(\alpha)$ are independent of *n*. Moreover, this pattern of subbands and minigaps is repeated for $\Phi_0/\Phi > 1$ periodically with period unity. However, the degeneracy of all subbands will increase with each repetition.

An important property of the butterfly spectrum for the experimental observation of the minigaps inside a Landau band is the *clustering* of subbands into groups. Starting with a given flux ratio p/q, p subbands exist. For a nearby flux ratio $p'/q' \approx p/q$ with $p' > p$, the p' subbands will group into p clusters close to the p bands of the first flux. If scattering of electrons at random impurities is taken into account, the density of states $D(E)$ calculated from the butterfly spectrum will be broadened and all but the biggest minigaps in between such clusters of subbands will smear out [20]. Thus the gaps visible to experiment will stay the same on a finite flux range. This enables the spectroscopy of the Hofstadter spectrum by magnetotransport measurements, where the magnetic field changes slightly when moving through the spectrum at a fixed electron density.

Magnetoresistivities

Although the density of states can be accessed more directly by magnetization [56, 57] and capacitance measurements [58, 59], a transport experiment yields additional information in the Hall conductance σ_{xy}, as will be explained in the next paragraph. The measured longitudinal conductivity $\sigma_{yy} = \sigma_{yy}^{\mathrm{sc}} + \Delta\sigma_{yy}$ has two contributions as already discussed in section 3.1.1. If the collision broadening is so small that the modulation-induced splitting is resolved, the overlap of subbands $j \neq j'$ with the same Landau index *n* is small. The band conductivity contributed by the narrow subbands is strongly suppressed compared to the one for the case when the subband splitting is totally smeared out due to collision broadening [4, 49, 60]. Consequently, the scattering conductivity
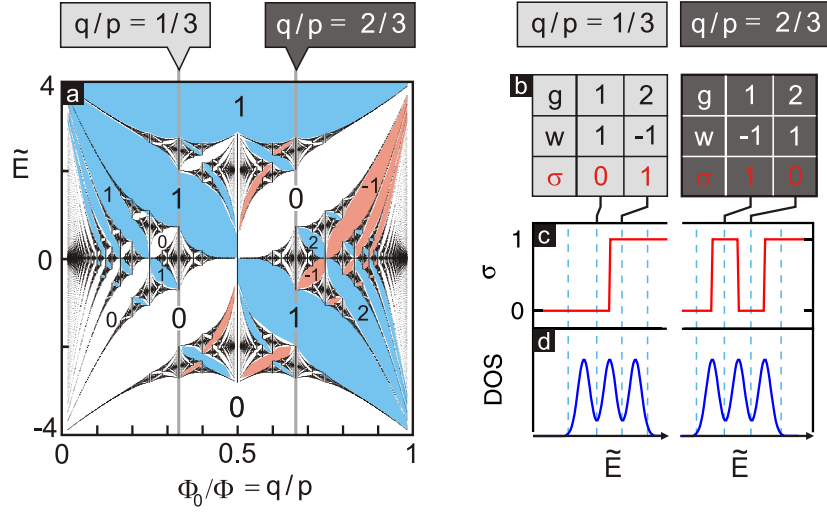
Figure 3.6:
Hall conductivities from the Diophantic equation: (a) The Hofstadter butterfly. Hall conductance contributions in units of $2e^2/h$ of the partially filled Landau band are indicated in some gaps. (b) The numbers solving Eqn. 3.13 for $\Phi_0/\Phi = 1/3$ and $2/3$, (c) the Hall conductivity contribution σ and (d) the density of states for these values of

$\sigma_{\mu\mu}^{\mathrm{sc}}(E_{\mathrm{F}}, T = 0) \propto D(E_{\mathrm{F}})^2$ (see Eqn. 2.21) will dominate the transport. Therefore the measured total conductivity σ_{yy} will reflect changes in the density of states $D(E)$. Hence additional minima in the Shubnikov-de Haas peaks of ρ_{xx} are indicators of a resolved subband splitting and thus of the Hofstadter spectrum.

While these additional minima in ρ_{xx} only tell us about the existence of a minigap, the value of the Hall conductance, which will be discussed next, depends also on the corresponding minigap index. Using this additional information, observed minigaps can be correlated to their position in the spectrum.

Hall conductivity

In accordance with Laughlin's general gauge invariance argument for noninteracting electrons [28], which we used already in section 2.4.2, the Hall conductivity is not only quantized in the Landau gaps between adjacent Landau bands but also when the Fermi energy is located inside a minigap. As for the unmodulated system, each of the n completely filled spin-degenerate Landau levels contributes a conductivity $2e^2/h$ to the total

Hall conductivity $\sigma_{xy} = 2e^2/h \cdot n$. Thouless [61] has shown that the contribution $\sigma \cdot 2e^2/h$ of a partially filled band to the total Hall conductance,

$$\sigma_{xy} = (n+\sigma) \cdot 2\frac{e^2}{h} \ , \tag{3.12}$$

varies in a non-trivial manner from minigap to minigap [23,61–63]. It can be obtained for the g-th minigap and a given flux ratio $\Phi_0/\Phi = q/p$ by solving a *Diophantic equation*[1],

$$g = wq + \sigma p, \ \ |w| \leqslant p/2, \tag{3.13}$$

with $g, p, q \in \mathbb{N}$ and $w, \sigma \in \mathbb{Z}$. This equation is solved for illustrative purposes for two values of $\Phi_0/\Phi = q/p = 1/3$ and $2/3$ marked by grey lines in Fig. 3.6a. For both cases, the spectrum consists of $p = 3$ subbands. When the Fermi energy moves through the subbands, the density of states reflects the threefold splitting as seen in Fig. 3.6d. For each of the values Φ_0/Φ and for each minigap ($g = 1$ and $g = 2$) the w- and σ-values, which solve Eqn. 3.13, are listed in Fig. 3.6b. The resulting Hall conductance contribution of the partially filled band is plotted in Fig. 3.6c. The discussed minigaps and others have been labeled with their Hall conductance contribution σ in units of $2e^2/h$ in Fig. 3.6a.

---

[1] Named after Diophantus of Alexandria, approx. 250 AD.

3.2   Weak magnetic field regime

In this section we introduce what effect a weak artificial modulation potential ($V_0 \ll E_F$) has on the dispersion relation and Fermi contours of a two-dimensional electron gas. After treating the simpler case of a one-dimensional periodic potential modulation, the two-dimensional case, of relevance here, will be studied. There, as in a natural crystal, electrons are Bragg reflected at the Brillouin zone boundaries (BZB) of the artificial lattice and energy gaps open up. Both closed and open electron orbits appear. An additional weak magnetic field ($\hbar\omega_c \ll V_0$) enables tunneling across gaps at the BZB. This produces an entire new network of electron paths, which can be studied using magnetotransport experiments.

3.2.1   The miniband structure

We know from Eqn. 2.1 that the electrons, which form the two-dimensional electron gas at a heterostructure interface, are quasi-free and have a paraboloidal dispersion in k_x and k_y. The influence of the underlying semiconductor crystal potential is entirely absorbed in the effective mass m^*. A cut of this paraboloid with the $k_y = 0$ plane, the dispersion in k_x, is depicted in the left panel of Fig. 3.7b.

When adding a one-dimensional modulation potential with period a in the x-direction as in Eqn. 3.1, the translational invariance is lifted and electrons will experience Bragg reflection at the Brillouin zone boundaries $k_x = j \cdot K_a/2 = j \cdot \pi/a$ with $j \in \{\pm 1, \pm 2, \pm 3, ...\}$. Since the applied modulation is weak compared to the Fermi energy E_F, the parabolic dispersion is modified only in the vicinity of the Brillouin zone boundaries, where small energy gaps open up. These gaps separate the parabolic dispersion into *minibands* of the artificial modulation potential. The term miniband indicates that these bands are superposed on the underlying band structure of the heterostructure lattice. Away from the Brillouin zone boundaries the dispersion is nearly unchanged from the unmodulated case [65]. This behavior is seen in the periodic zone scheme of the middle panel of Fig. 3.7b, which is created by repeating all sections of the parabolic dispersion at integer multiples of reciprocal superlattice vectors K_a.

For a two-dimensional modulation, the band structure is more complicated, since gaps open up in both the k_x- and k_y-direction and the resulting sections are repeated along both directions at reciprocal lattice vectors $\mathbf{q} = K_a \cdot (n_x, n_y)$, with $n_x, n_y \in \mathbb{N}$. To find the gap
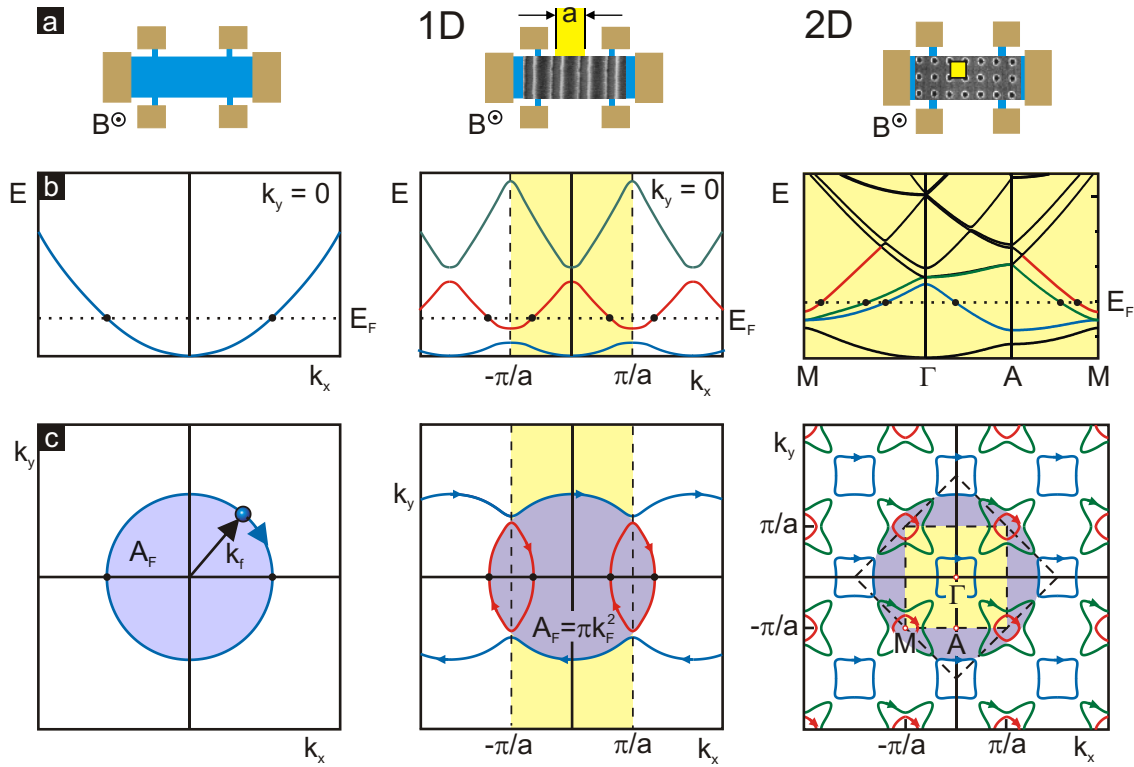
Figure 3.7:
Dispersion relation and periodic zone scheme for no modulation, 1D and 2D modulation. Left panel: The free electron case. Middle panel: One dimensional modulation. Right panel: Two dimensional modulation. a) Sample structure sketch. b) The dispersion relation. A dotted line represents the Fermi energy. The modulation opens up gaps at Brillouin zone boundaries. The band structure in the right panel is based on Fig. 4 in Ref. [64]. c) The periodic zone scheme, depicting Fermi contours in *k*-space. Arrows indicate the chirality of the orbits imposed by the applied magnetic field. Brillouin zones are marked in yellow. For the right panel the second Brillouin zone is demarcated with dashed lines.
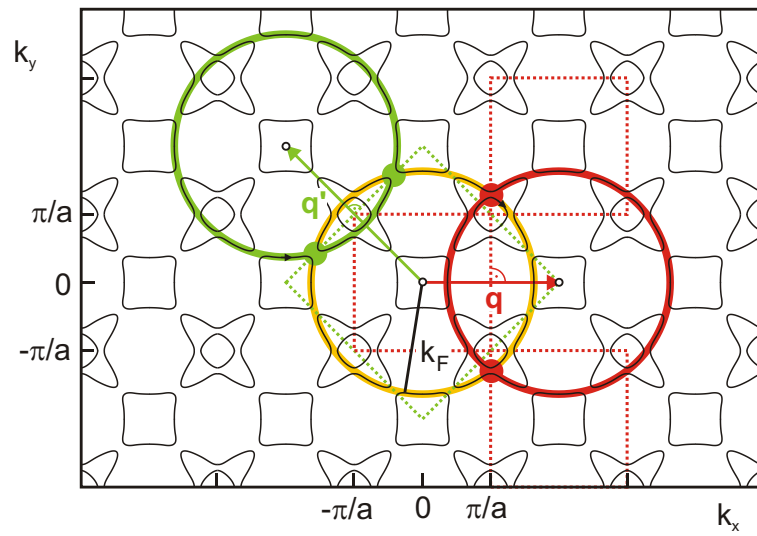
Figure 3.8:
Gap positions in the periodic zone scheme for the 2D modulation case. Large red dots mark the intersections of two Fermi circles with distance $\mathbf{q} = K_a \cdot (1,0)$. The intersections are on the first Brillouin zone boundary (dotted red line). Green dots mark the intersections for $\mathbf{q}' = K_a \cdot (-1,1)$. They are on the boundary of the second Brillouin zone (dotted green line).

positions, we need the Fourier expansion of the modulation potential

$$V(\mathbf{r}) = \sum_{\mathbf{q} \neq 0} V_{\mathbf{q}} \exp(i\mathbf{q} \cdot \mathbf{r}) \,. \tag{3.14}$$

Gaps appear at Brillouin zone boundaries perpendicular to reciprocal lattice vectors $\mathbf{q} \neq 0$ with non-zero Fourier components $V_{\pm\mathbf{q}}$. This is demonstrated in Fig. 3.8 for the first (red; $\mathbf{q} = K_a \cdot (1,0)$) and second (green; $\mathbf{q}' = K_a \cdot (-1,1)$) Brillouin zone. The size of these energy gaps can be estimated to be [65]

$$\Delta E_{\mathbf{q}} = 2|V_{\mathbf{q}}| \,. \tag{3.15}$$

Cuts along first $(\Gamma - A - M)$ and second $(M - \Gamma)$ Brillouin zone boundaries through the band structure are plotted in the right panel of Fig. 3.7b. Here, non-zero second order Fourier components are included in the modulation potential and are e.g. responsible for the degeneracy lifting (splitting into two lines) along the $M - \Gamma$ direction.

The important properties in the discussion of a modulation potential $V(\mathbf{r})$ are both its shape and its overall strength. To separate these two properties, we express all Fourier components $V_{\mathbf{q}}$ in terms of an additional parameter V_0:

$$V_{\mathbf{q}} = V_0 \cdot \alpha_{\mathbf{q}} \,. \tag{3.16}$$

For instance for Eqn. 3.6, we have $V_{K_a \cdot (\pm 1, 0)} = V_{K_a \cdot (0, \pm 1)} = V_0 \cdot 1/4$. The single modulation potential strength parameter V_0 can now be treated independently from the modulation potential shape, which is determined by the relative sizes of the $\alpha_{\mathbf{q}}$.

3.2.2   Fermi contours

For a given electron density n_s we can calculate the Fermi energy E_F (cf. Fig.3.7b) and plot the k-space Fermi surfaces with constant energy $E = E_\mathrm{F}$ for the three discussed cases illustrated in Fig.3.7c. Only electrons on these contours are relevant in dc-transport experiments. For the unmodulated case in the left panel, the Fermi contour is just the Fermi circle with radius k_F. In the presence of a perpendicular magnetic field B the electrons will travel in a certain direction (blue arrow) on this constant energy contour. The corresponding real space trajectory is rotated by $\pi/2$ and scaled with $l_\mathrm{B}^2 = \hbar/(eB)$. The quantization of this real space electron trajectory leads to Shubnikov-de Haas oscillations in the longitudinal transport resistivity as explained in section 2.4.1. and produces $1/B$-periodic oscillations with a period (Eqn. 2.22)

$$\Delta \left(\frac{1}{B} \right) = \frac{2\pi e}{\hbar} \frac{1}{A_\mathrm{F}} \tag{3.17}$$

which depends on the enclosed area A_F. This is true for arbitrarily shaped areas. So by analyzing the $1/B$-periodicity of oscillations in the longitudinal magnetotransport, one can determine the area enclosed by the corresponding Fermi contour.

For a one-dimensional modulation, open undulating and closed trajectories emerge. Examples are the blue and red trajectories in the middle panel of Fig. 3.7c. They are separated by gaps at the boundary of the first Brillouin zone marked in yellow. The red closed trajectory is smaller than the one for the unmodulated case. It will thus manifest itself by a larger $1/B$-period in the magnetotransport oscillations.

For a two-dimensional modulation more open and closed trajectories may show up. The three even smaller closed trajectories (red, green, and blue) in the right panel of Fig. 3.7c should be visible as three superposed $1/B$-oscillations in magnetotransport.

Summing up, one can observe the influence of the modulation potential on the Fermi contours using a magnetotransport experiment by analyzing the periodicity of $1/B$-periodic oscillations.

3.2.3 Magnetic breakthrough

When increasing the magnetic field B, the semiclassical picture used up to now no longer holds. Quantum mechanical tunneling across gaps at the Brillouin zone boundary becomes possible. This is called *magnetic breakthrough*. It discloses an entire network of alternative closed electron paths which produce additional $1/B$-periodic oscillatory features. In a simple model, the magnetic field introduces an uncertainty in real space proportional to the magnetic length $\Delta x \approx \Delta y \approx l_B$. This corresponds to an uncertainty in reciprocal space $\Delta k_x > 1/\Delta x \approx 1/l_B$. If this Δk gets larger than the gaps introduced by the modulation potential, tunneling becomes significant [65]. A proper calculation leads to a tunnel probability [66–69]

$$P = \exp\left(-\frac{B_0^{\mathrm{qm}}}{B}\right) = \exp\left(-\frac{\pi \Delta E_{\mathbf{q}}^2}{4\hbar \omega_c E_F \sin(2\theta_{\mathbf{q}})}\right) =: P_{\mathbf{q}}(k_F, K_a, V_0^2/B) , \qquad (3.18)$$

if the modulation potential is weak ($V_0 \ll E_F$). This probability depends on the energy gap $\Delta E_{\mathbf{q}} \approx 2|V_{\mathbf{q}}|$ (3.15), and the incident Bragg scattering angle $\theta_{\mathbf{q}}$. For a weak modulation potential, the size of the gap in k-space (Fig. 3.9b) can be estimated as follows: $\Delta k \approx \Delta E/|\partial E/\partial \mathbf{k}| \approx \Delta E/\hbar v_F$. Here we used the dispersion of a free two-dimensional electron gas. Both the gap Δk as well as the scattering angle $\theta_{\mathbf{q}}$ are illustrated in Fig. 3.9b for the simple one-dimensional case.
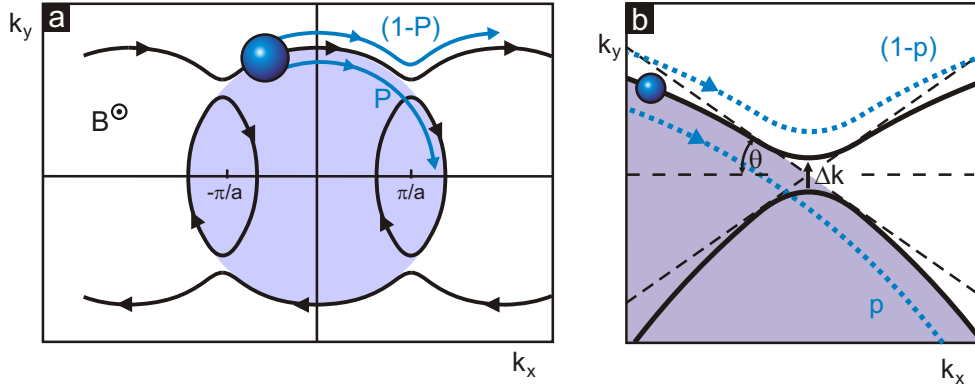
Figure 3.9:
a) Magnetic breakthrough between neighboring Fermi contours of a 1D modulated electron system enables the lower blue trajectory with a probability P. There, the electron tunnels across the gap at the Brillouin zone boundary. b) The Bragg scattering angle θ enters the tunneling probability P. The energy gap ΔE is accompanied by a corresponding change Δk in k-space.

The non-standard notation $P_{\mathbf{q}}(k_{\mathrm{F}}, K_a, V_0^2/B)$ is introduced in Eqn. 3.18 to separate the parameter $\mathbf{q}$ specifying a certain gap from all other parameters, which are identical for all gaps: The parameters k_{F} and K_a determine the geometrical properties of the network of repeated Fermi circles. They also control where and with which angle $\theta_{\mathbf{q}}$ the circles with distance $\mathbf{q}$ will intersect in k-space. The energy gaps $\Delta E_{\mathbf{q}}$ at these intersections enter the probability as $\Delta E_{\mathbf{q}}^2 \approx (2V_{\mathbf{q}})^2$ (cf. Eqn. 3.15). As discussed in section 3.2.1, we introduce a modulation potential strength parameter V_0 and express the Fourier components as $V_{\mathbf{q}} = V_0 \cdot \alpha_{\mathbf{q}}$. Since V_0 is independent of $\mathbf{q}$, we can use it to collect the energy gap dependence together with the remaining magnetic field dependence in the parameter V_0^2/B. Note that a change in the potential modulation amplitude can be compensated for by a suitable change in the magnetic field. The dependence on the modulation potential shape, described by the parameters $\alpha_{\mathbf{q}}$, is absorbed in the symbol $P_{\mathbf{q}}$, which is different for each gap parameter $\mathbf{q}$.

3.2.4   The network model

To understand the implications of magnetic breakthrough, we revert to the *network model* devised by Pippard: An entire network of electron paths is created by the combination of all sections of the Fermi contours and different tunneling events. For a given magnetic field, the electron trajectory will lie on this network with a statistical distribution given

by the tunnel probabilities at each energy gap. The complete network will give rise to several $1/B$-periodic oscillatory features in the longitudinal resistivity [68, 70, 71]. Pippard, however, pointed out that no adequate theory of the conductivity of such a coherent network for a two-dimensional modulation has been devised [72]. Nevertheless, for the case of a one-dimensional modulation, the network model is shown to provide the same result as a full quantum mechanical calculation [73].

Instead of solving the two-dimensional network problem, we focus first on individual closed trajectories in this network. As the magnetic field is swept, some closed trajectories become dominant while others are unlikely. The most probable trajectories are seen in experiment as $1/B$-oscillations in the longitudinal resistivity, just as described in section 3.2.2. These $1/B$-oscillations will be the subject of section 6.3. Two path quantum interferences present in the network model are taken into account later in section 6.4. The most probable quantum interferences give rise to additional $1/B$-oscillations in ρ_{xx}. This two step approach will prove successful to explain the $1/B$-oscillations observed in experiment.

3.2.5 Positive Magnetoresistance

Magnetic breakthrough has also consequences near zero field, where it limits the *positive magnetoresistance*: Below $B \approx 0.03$ T a positive magnetoresistance peak in ρ_{xx} is seen in Fig. 3.1. This peak already arises for a one-dimensional modulation $V(x) = (V_0/2)\cos(Kx)$, but only for transport along the direction of the modulation (ρ_{xx}). It can be explained in terms of the undulating runaway trajectories (e.g. in blue in the middle panel of Fig. 3.7c). They dominate the transport, if tunneling is not significant. The corresponding real space trajectories run along the y-direction. Electrons traveling along these open trajectories produce an additional contribution to the conductivity $\Delta\sigma_{yy}$ and hence an increase of ρ_{xx} [74–76]. This positive magnetoresistance will saturate when tunneling gets significant. We will use the following criterion: $P > e^{-1}$. Using Eqn. 3.18 the critical magnetic field at which $P > e^{-1}$ can be estimated as [66–69]

$$B_0^{\text{qm}} \approx \frac{\pi^2 m^* e a V_0^2}{h^2 v_{\text{F}}} \, . \tag{3.19}$$

Here, the approximations $\sin(2\theta) \approx K_a/k_{\text{F}}$ and $\Delta E \approx V_0$ were used. They hold for $k_{\text{F}} \gg K_a$, which is valid for the samples at hand.

This model qualitatively describes the positive magnetoresistance, but the simpler model of classical magnetic breakthrough [76–78] is better suited to explain the available exper-

imental data on one-dimensional modulation [76]. Electrons feel both the Lorentz force $F_{\mathrm{L}} = -ev_{\mathrm{F}}B$ and a force $F_{\mathrm{V}} = -\mathrm{d}V(x)/\mathrm{d}x = (V_0/2)K_a\sin(K_a x)$ due to the modulation potential. The latter drives the electrons back onto open trajectories. This again enhances the conductivity σ_{yy}. The resulting positive magnetoresistance will saturate at a magnetic field

$$B_0^{\mathrm{cl}} = \frac{\pi V_0}{eav_{\mathrm{F}}}\,,\tag{3.20}$$

where the two forces F_{L} and F_{V} are equal [77].

Although both models hold only for one-dimensional modulation, Eqn. 3.20 has been used on occasion to roughly estimate the amplitude of the potential modulation V_0 even for two-dimensional modulation. This is discussed further in appendix E.

4 Sample preparation and measurement procedures

To unveil the Hofstadter energy spectrum or quantum interferences typical for two-dimensional lattices, both the sample fabrication and the measurement techniques have to be optimized: A prerequisite is a shallow heterostructure design offering a high mobility. In addition, fabrication procedures for short period lateral superlattices with minimal impact on sample quality are developed. For the measurement, a self-adapting illumination process is devised and finally an optimized data analysis is used. Here, we will discuss each of these ingredients in more detail.

4.1 Optimized fabrication of modulated samples

4.1.1 The heterostructure

For the observation of signatures of the butterfly spectrum both mobility and two-dimensional modulation amplitude need to be sufficiently large. The size of the minigaps in the Hofstadter butterfly is proportional to the modulation amplitude. A large modulation amplitude ensures that the minigaps are big enough to be detected. To ensure that disorder induced broadening does not smear out these minigaps, the total quantum scattering time τ_0 should be large. First signs of the butterfly spectrum were seen in samples with a mobility larger than $1.5 \cdot 10^6 \text{cm}^2/\text{Vs}$ for typical modulation amplitudes ($V_0 \approx 4\% E_\text{F} \approx 0.6\text{meV}$) also used in this work.

Since the modulation is applied at the surface by a periodically displaced gate (see section 4.1.3), the final modulation amplitude felt by the electrons is sensitive to the depth of the

two-dimensional electron gas. In order to get a large modulation, shallow heterostructures are thus needed. High mobility heterostructures typically have the donor layer as far away from the two-dimensional electron gas as possible. This avoids scattering of electrons in the two-dimensional electron gas by the random potential of the ionized donor atoms. To optimize for both properties is difficult. In the heterostructure #5 − 74[1] mainly used here this is solved by growing several delta doped quantum wells above the GaAs-AlGaAs interface as illustrated in Fig. 2.1. When illuminated, the persistent photoconductivity effect not only increases the density of the two-dimensional electron gas, but also produces some parallel conduction in these wells. It improves screening of the random potential and the mobility is enhanced by as much as a factor of three: The mobility rises from $1 \cdot 10^6 \text{cm}^2/\text{Vs}$ to $3.4 \cdot 10^6 \text{cm}^2/\text{Vs}$. These samples also show excellent Schottky barrier behavior at low temperatures, which is instrumental to tune the electron density with an applied gate voltage. The samples do have one disadvantage though. Their electron density and mobility reacts very sensitively and also non-monotonously to the strength and duration of the illumination. A computerized control of the illumination process was able to solve this problem as demonstrated in section 4.3.2.

Samples were fabricated from 5.9 mm times 6.1 mm big pieces of the shallow (100)-GaAs/AlGaAs heterostructure. One each piece, 6×5 Hall bars are fabricated at the same time. The Hall bars are oriented along the [011] direction of the heterostructure. Hall bars along this direction have a slightly lower mobility [79], but exhibit the largest modulation strength. This is further discussed in section 4.1.3.

The two cleavage directions can be distinguished using the big wafer flat. It is is parallel to the $[01\bar{1}]$ direction as depicted in Fig. 4.1. If the rest of the wafer is too small to see the flat, the backside of the heterostructure still shows an etched pattern caused during wafer lapping. It consists of ovals whose long axis is aligned along the [011] direction.

4.1.2   Hall bar fabrication

To measure the longitudinal and Hall resistances in a magneto-transport measurement, Hall bar geometries are fabricated. The sample is spin coated with a thin layer of photo resist and subsequently exposed with ultra violet light through an optical lithography mask to define the mesa structure shown in blue in Fig. 4.1 The mask consists of a glass

---

[1] The heterostructure is grown by Dr. V. Umansky, from the Braun Submicron Research Center at the Weizmann Institute of Science in Rehovot, Israel
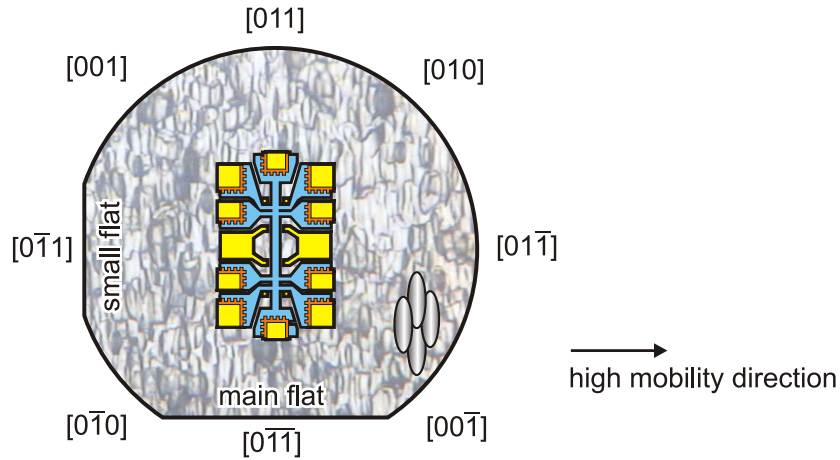
Figure 4.1:

The Hall bar mask and the crystal directions. Both the wafer flats and the ovals on the backside of the wafer indicate the crystal direction. A not-to-scale microscopic image of the backside of sample #5 − 74 and the Hall bar orientation used are shown. The different optical lithography steps for Hall bar production are laid on top of each other using the colors blue (mesa), orange (ohmic contacts), and yellow (bond pads).

plate coated with chrome in those areas where the resist should be left unexposed[2]. After exposure, the resist is developed and only the mesa structure stays coated. A 70 nm deep wet chemical etch removes the two-dimensional electron gas in the uncoated area (second step of Fig. 4.2). After removing the remaining resist, a second lithography step defines windows which will later form the ohmic contacts (orange in Fig. 4.1). Remaining photo resist in these windows is removed by 30 seconds of O_2 plasma. Any oxide layer on the exposed heterostructure surface is then removed by dipping the sample for 2 minutes in semicoclean, 5 seconds in water, 5 seconds in hydrochloric acid (30%) and 1 second in water. Next 5 nm nickel, an eutectic mixture consisting of approximately 130 nm germanium and 250 nm gold, and finally 40 nm of nickel are thermally evaporated on the piece. Metal on top of the resist layer is lifted off by placing the sample in an acetone bath. When heating the sample in forming gas mixture to 300 °C for 60 seconds and subsequently to 440 °C for 30 seconds, these metals are annealed into the material and provide ohmic contacts to the two-dimensional electron gas [80]. During a third optical lithography step, approximately 20 nm chromium and 100 nm gold are deposited in the yellow areas in Fig. 4.1 to complete the contact pads for easy wire bonding to a chip carrier.

---

[2] The masks necessary for all steps in the production of a Hall bar are typically combined side by side in one CAD file and given to "Masken Lithographie & Consulting GmbH, Jena" to produce one physical glass mask. In the course of this work, several Hall bar masks were designed.

As grown wafer

2DES →

AlGaAs

GaAs

Mesa definition

Patterning ohmic contacts

Writing e-beam pattern in PMMA resist

Deposition of metal gate
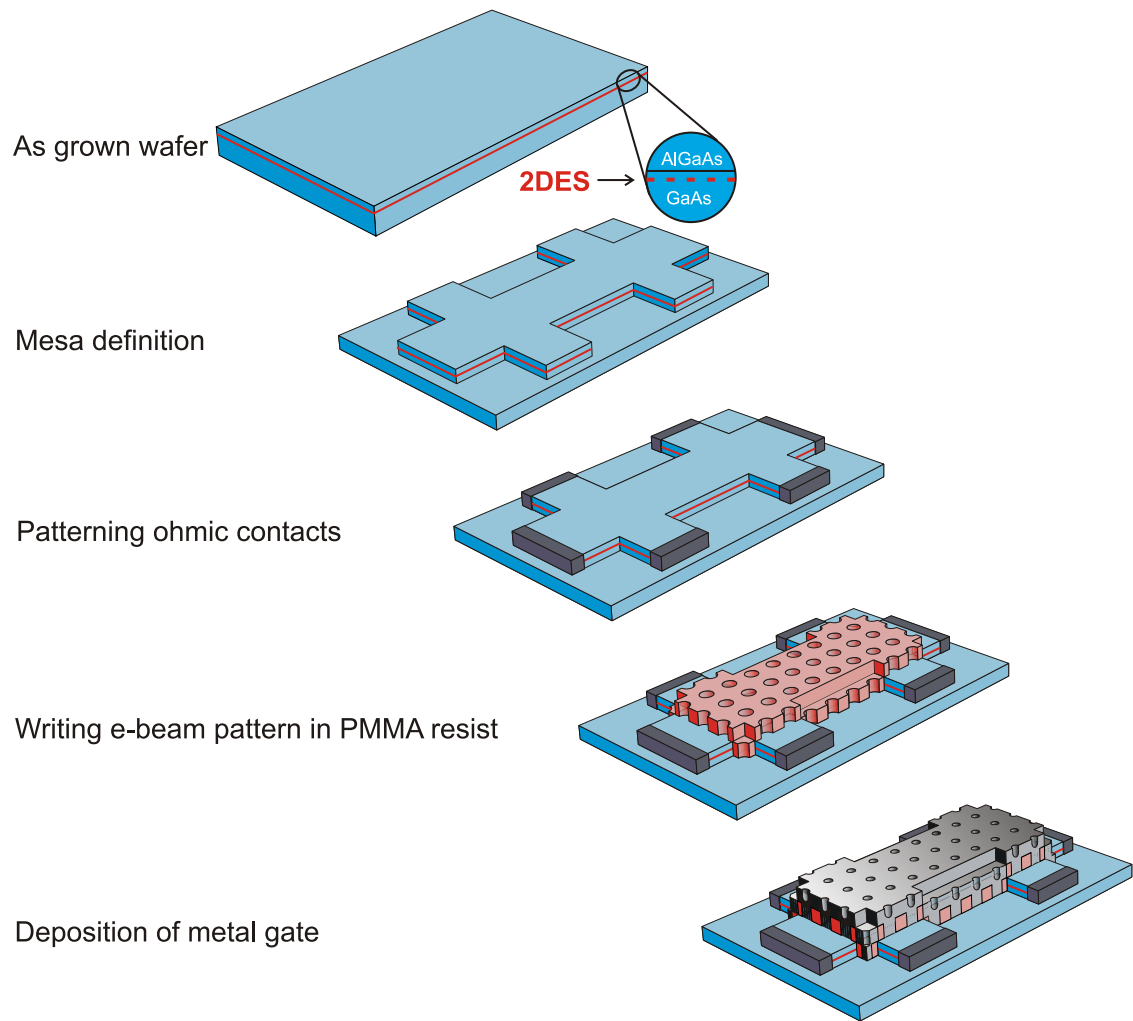
Figure 4.2:
   Fabrication steps to produce a Hall bar geometry with a two-dimensional lateral superlattice.

4.1.3   Gate fabrication

To achieve a sub-micrometer weak periodic electric potential modulation at the position of the two-dimensional electron gas, different methods are available. To create a permanent modulation, a resist layer on the sample surface is patterned in a periodic fashion. The photo-resist is either exposed with two holographic illuminations using the interference pattern produced with two coherent laser beams [11, 81]. Periodicities on the order of 200 nm are achieved with this procedure. Smaller periodicities of the order of 100 nm can be obtained with electron beam lithography of a polymethyl methacrylate (PMMA) resist. In both cases, the patterns are developed and must be etched or metalized to be effective. Another possibility is to use in-situ holographic illumination and exploit the persistent photoconductivity effect. When illuminated, deep traps in the doped AlGaAs layers of the heterostructure, so called DX centers, are ionized and give up their electrons to the two-dimensional electron system. These DX centers stay ionized at temperatures below 100 K. They generate a local increase in electron density [82, 83]. This density modulation is reversible and disappears when the sample is warmed up.

In this work a metallic gate patterned with e-beam lithography is used since it enables electron density tuning and provides the necessary periodicities of 100 nm and smaller. Etched samples were produced but not considered since the potential modulation strength decreased considerably when illuminated. This is a crucial drawback. The heterostructure #5 − 74 exhibits a steep mobility increase with illumination. Only the gated samples allow to exploit this property as illustrated in Fig. 4.3. They provide at the same time sufficient modulation strength and high mobility, if all processing steps are carefully optimized as detailed below. Unrivaled mobilities above $3.4 \cdot 10^6 \mathrm{cm}^2/\mathrm{Vs}$ are obtained for processed samples after illumination.

Electron beam lithography

As a first step, the Hall bars are cleaned and spin coated with a layer of polymethyl methacrylate (PMMA)[3] resist. After baking, this resist is exposed in the active region of the Hall bars with a 100 nm period square lattice of dots using an acceleration voltage of 50 kV for the samples used in chapters 5 and 6. The pattern is then developed[4] into a lattice of holes. A cartoon version of the patterned resist is depicted in the fourth panel of

---

[3] Also sold under the trademark Plexiglas by the chemical company Rohm and Haas.

[4] The developer is a mixture of methyl iso-butyl ketone (MIBK) and isopropylic alcohol. It solves the exposed, shorter chains of PMMA.
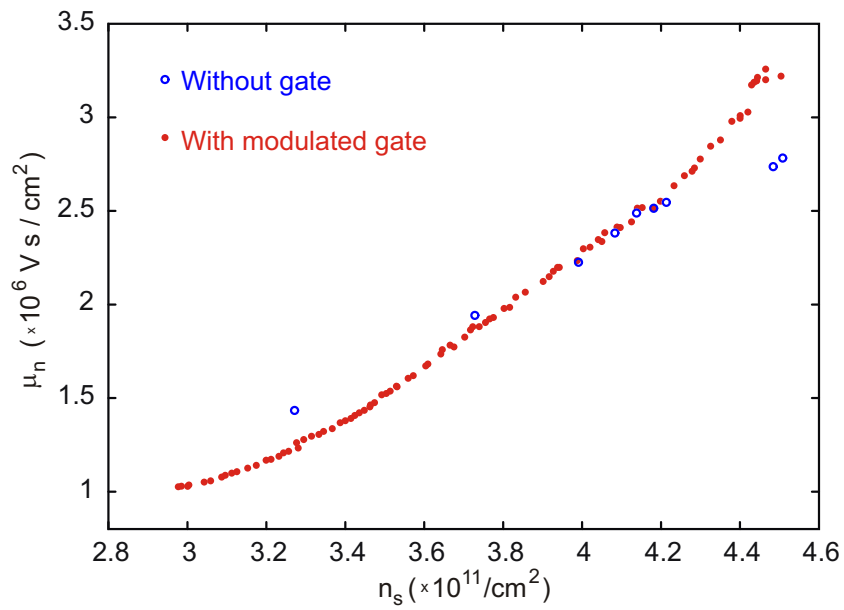
Figure 4.3:
The mobility versus electron density of samples produced from wafer #5 − 74. The ungated sample is measured at 1.4 K and illuminated with a infrared LED from the backside while the gated sample is measured in a dilution fridge at 50 mK and carefully illuminated with a red light LED.

Fig. 4.2. The details of the electron beam lithography process, in particular the one used for the samples of chapter 7, are listed in appendix B.

Essential for the optimization purposes is the availability of reproducible high quality patterns across many different Hall bars and heterostructure pieces. Only when the patterns are comparable in quality, the optimization of the subsequent evaporation steps can be successful. The best samples came out of this optimization process and are used in chapters 5 and 6.

Evaporation preparation

A piece with 6×5 Hall bars is cleaved into up to 16 smaller pieces for finding optimal paramters. The electron beam pattern is treated with an O_2 plasma and one of the smaller pieces is glued with a tiny amount[5] of S1805 photo resist onto a shadow mask holder. It is baked for four minutes at $85\,°C$. A metal shadow mask with etched holes for the gate is aligned with respect to the e-beam patterned Hall bars and fixed flush to the sample surface.

Evaporation

The metal gate is evaporated through the holes of the shadow mask in an ultra high vacuum chamber fitted with an electron beam evaporator. The sample and shadow mask holder are mounted on a cold finger cooled by liquid nitrogen. First an adhesive layer, here chromium, is evaporated. Then a first layer of gold is evaporated followed by two more layers, while the sample is tilted at different angles with respect to the direction of the evaporation source. This complex evaporation sequence appears to be essential to obtain a large modulation strength while retaining the high mobility of the sample.

Modulation strength optimization

To optimize for a large modulation potential strength, the origin of the modulation has to be known. Both anisotropic and isotropic modulation effects exist: The gate exerts a periodical stress on the sample surface. The stress translates into an electrical modulation potential via the piezoelectric effect. This effect is equal in magnitude but opposite in sign

---

[5] Too much photoresist for gluing the sample can result in bad thermal conductivity of the holder to the sample thereby impeding efficient cooling of the sample.
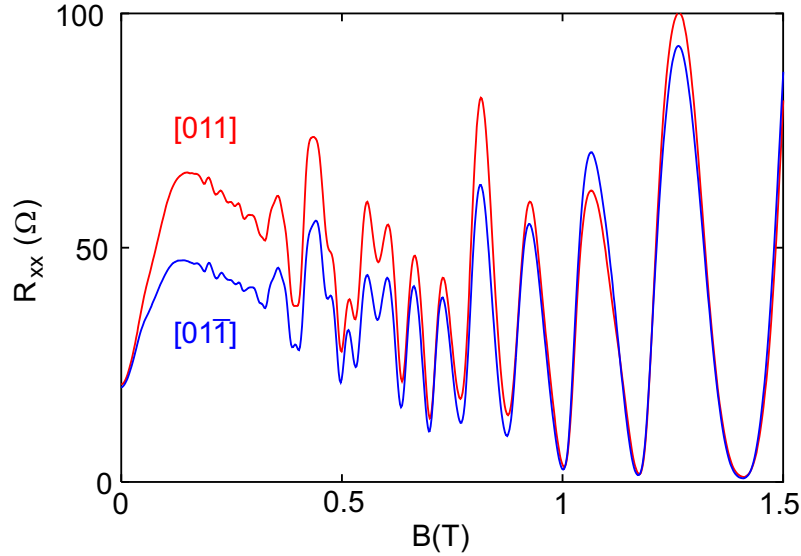
Figure 4.4:
  Magnetotransport data at 1.4 K of Hall bars oriented along the two different cleavage directions. The Hall bars have a square modulation with 100 nm period. The observed commensurability oscillations are similar in amplitude.

in the two cleavage directions $\{011\}$. On the other hand, isotropic effects may arise from Fermi level pinning. Both type of effects play a role in the experiments of Ref. [84]: They pattern a strained InGaAs layer on top of a heterostructure into pillars with 100 nm period. These pillars try to expand the heterostructure, since the lattice constant of InGaAs is 7.2% larger than the one of GaAs [85]. They find larger commensurability oscillations for Hall bars oriented along the $[01\bar{1}]$ direction than for the perpendicular direction. In these samples, the piezoelectric and anisotropic effects add along the $[01\bar{1}]$ direction and subtract in the other. This is different from the behavior we observe in a 100 nm period 2D modulated sample: We detect only a slight increase in commensurability oscillations along the $[011]$ direction (cf. Fig. 4.4). This small difference in the two longitudinal resistances suggests that stress prevails over isotropic effects, like Fermi level pinning. This observation is also supported by measurements on samples where the modulation is aligned along the $\langle 001 \rangle$ directions as discussed in chapter 7.4: No commensurability oscillations are observable for these samples, as expected for a modulation of purely piezoelectric origin, since the piezoelectric effect is absent along the $\langle 001 \rangle$ directions of the GaAs crystal.

Keeping this in mind, we optimized for a large periodical stress on the sample surface:

56

Care is taken to avoid residual water on the semiconductor surface, which may prevent good adhesion of the gate metal during evaporation. The sample is inserted into a load lock chamber which is pumped for one hour down to a pressure of $5 \cdot 10^{-6}$ mbar. Then the sample is inserted into the evaporation chamber. This chamber is pumped for 30 minutes and finally 5 nm of chromium are evaporated while the sample is rotated away to clean the chromium surface of the source and to find suitable evaporation parameters. This further improves the vacuum due to the getter pumping effect of chromium. Only at a high vacuum below $5 \cdot 10^{-9}$ mbar and an H_2O partial pressure below 10^{-9} mbar the sample is being cooled with the help of liquid nitrogen. Best results are achieved if the H_2O partial pressure does not rise above $5 \cdot 10^{-9}$ mbar during the evaporation process.

The cooling with liquid nitrogen enhances the stress exerted by the gate and additionally reduces the gate leakage.

The stress is also increased if the evaporation material has been used a few times already, presumably because surface contamination is reduced.

Mobility optimization

The second important parameter for the experiments is mobility. Evaporating a thick metal gate on the shallow high mobility sample decreases the mobility by as much as a factor of 10.

In order to reduce the impact on the mobility, the appropriate combination of adhesive layer and main gate material has to be selected. Among the material combinations tried (nickel chromium and gold, chromium and gold, only chromium, only gold-palladium, titanium and gold), chromium and gold were identified to be the best option. Moreover, the evaporation angles and thicknesses were optimized to create a large stress on the semiconductor surface (cf. table 4.1).

The electron beam evaporation process exposes the sample to fast secondary electrons which may create defects in the heterostructure and degrade the mobility. Heating of the sample may also occur. It may lead to a moderate flow of the structured PMMA resist layer at temperatures as low as $110\,^{\circ}$C. This affects holes of 100 nm diameter [86]. In vacuum PMMA may get unstable at temperatures of $50\,^{\circ}$C [87].

For these reasons, the electron beam emission current should be reduced to a minimum:

The emission rate controller "Inficon XTC Thin Film Thickness and Rate Monitor" was bypassed and the hardware emission control of the Leybold high voltage supply was

Evaporation Step	Material	Jeol (200 nm) thickness	angle	Leica (90 nm) thickness	angle
1	Chromium	20 nm		15 nm	
2	Gold	40 nm		15 nm	
3	Gold	40 nm	14°	40 nm	14°
4	Gold	40 nm	−10°	40 nm	−12°

Table 4.1:

  The optimized evaporation thicknesses and angles for samples exposed in different lithography systems. The PMMA resist thicknesses are shown in brackets. Angles are measured with respect to the sample surface normal. The decrease in the evaporation angle for the fourth step takes into account the material deposited during previous steps.

used instead. This way, a much finer control over the emission current becomes possible. Very low stable evaporation rates (0.25 Å/s for chromium and 0.7 Å/s for gold) can be achieved.

The evaporation materials were put into crucibles instead of putting them directly into the evaporation hearths. The crucibles prevent thermal contact between the materials and the water-cooled evaporation hearths. The smaller diameter of the crucibles compared to the bare hearth reduces the amount of material needed to get a sufficiently constant evaporation rate. As a result, the electron beam power was dramatically reduced. For chromium, an electrographite crucible[6] is used. Gold is evaporated from a non-conducting boron nitride silicon carbide (BNSC) crucible. It features a small hole in the base to allow for electrical contact so that incident electrons can flow off. The boron nitrite is non-wettable by the evaporation material.

The overall decrease in electron beam power is directly reflected in the increased mobility of the finished gated samples.

4.1.4 Final steps

After evaporating the chromium and gold layers and slowly warming up the sample to room temperature, individual Hall bars are cleaved and glued into chip carriers as depicted in Fig. 4.7. This is done to avoid a degradation of the modulation strength in unbonded Hall bars on the same chip after multiple cooling cycles. To ensure a good adhesion and to avoid bubbles between the sample and the chip carrier, only a small

---

[6] Supplier of the crucibles is "Leybold Optics GmbH, Hanau".
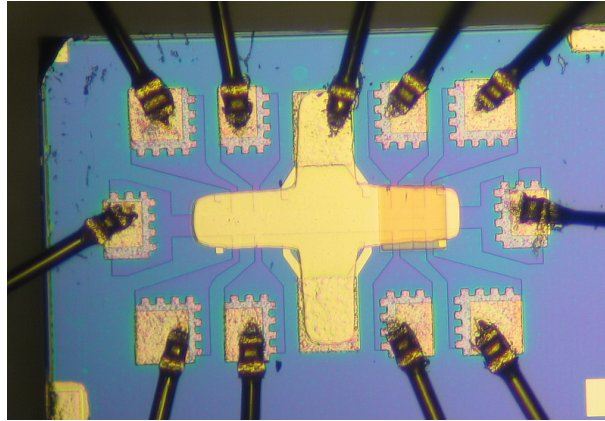
Figure 4.5:
  A microscopic image of sample #5-74/4-B1. During evaporation, the sample was tilted around the horizontal axis. The writing field of the electron beam lithography is seen on the right hand side as a dark square. The surface is still covered with PMMA.

amount of PMMA[7] is used as glue and it is heated for 10 minutes to a temperature of 85 °C and 10 minutes to 160 °C. This procedure is necessary to make bonding through the remaining PMMA layer on the sample surface onto the ohmic contacts possible. A bonded sample is displayed in Fig. 4.5.

4.2   Measurement setup

To measure the Hall and longitudinal magnetoresistances, the chip carrier with the Hall bar is put into a matching socket which is mounted at the end of a rod shaped sample holder. This holder is inserted into the superconducting magnet of a cryostat. Preliminary characterizations are performed in a ^{4}He bath cryostat. When pumping on the liquid surface of the helium bath, its temperature is lowered from 4.2 K to 1.4 K. To measure quantum effects as presented in chapters 5 and 6, lower temperatures are needed. There the sample is cooled down to 50 mK using a ^{3}He/^{4}He dilution refrigerator.

In both cases the longitudinal R_{xx} and Hall resistances R_{xy} are measured using a four point technique, as illustrated in Fig. 4.6: A 13.6 Hz alternating current is drawn between the current contacts and the voltage drops V_{xx} and V_{xy} across the respective potential probes are measured using two "Princeton Applied Research EG&G 5210" lock-in amplifiers.

---

[7] diluted to 7%
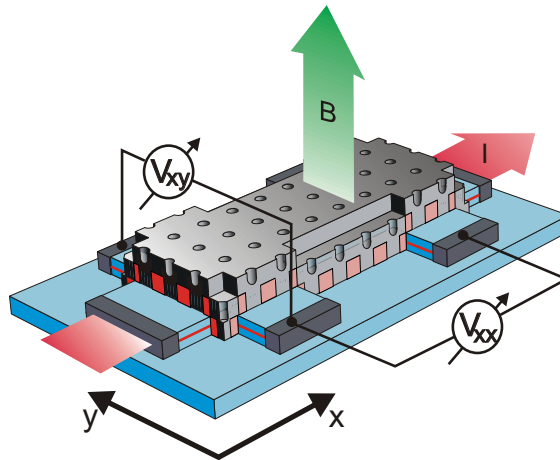
Figure 4.6:

A modulated Hall bar sample with applied current *I* and perpendicular magnetic field *B*. Both the longitudinal voltage V_{xx} and the Hall voltage V_{xy} can be measured.

Each lock-in amplifier is calibrated prior to the experiment by using a quantum Hall plateau measurement as reference. The lock-ins are galvanically isolated from mains by isolation transformers to avoid ground loops. To avoid unnecessary heating, the alternating current is lowered from 100 nA for measurements at 1.4 K to 20 nA for 50 mK. The lock-in amplifiers output $dV_{ii}/dI|_{I=0}$ as an analog signal to multimeters which digitize it and send it to a computer. The bus connections to the computer are galvanically isolated. To characterize samples, the magnetic field is swept from zero to 1.5 T at 0.1 T/min. For measurements at lowest temperatures, slower sweep rates of 0.03 T/min are necessary to catch all of the fine structure contained in the magnetoresistance.

4.3 Electron density variation

For the observation and identification of quantum interferences as described in chapter 6, a wide carrier density range is mandatory. Low densities can be achieved by tuning the gate voltage. A negative voltage decreases the electron density, a positive one may increase it. Large positive voltages can however not be applied because of gate leakage. To access higher densities, we exploit the persistent photoconductivity effect introduced in section 4.1.3. To achieve the highest densities possible, the sample illumination of the sample is optimized by proper placement of the LED and by using a self-adapting illumination sequence.
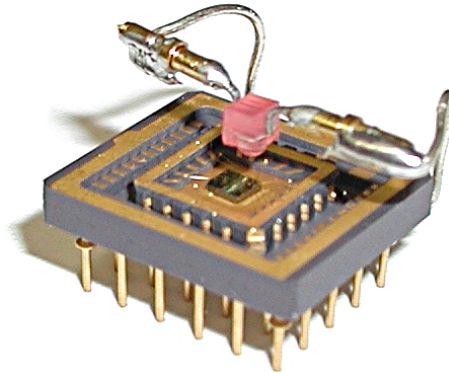
Figure 4.7:
  Geometry used to illuminate the sample with a red LED. The LED is placed directly above the active Hall bar.

4.3.1 LED type and placement

In early experiments the sample was glued onto a transparent glass plate mounted over a hole in the chip carrier to enable illumination from the back side. An infrared LED with a central wavelength $\lambda_{\mathrm{LED}} = 1060$ nm was used to ensure that the photon energy is below the band gap of the GaAs substrate to prevent light absorption in the substrate.

Here, front illumination with a red LED is used instead. Both the electron density and the sample mobility increase appreciably if the gated heterostructure is illuminated through the 140 nm thick Cr/Au gate. This density tunability through a thick gate has also been exploited by another group working on modulated two-dimensional electron gases [88].

For measurements in the dilution refrigerator one has to avoid excessive heating of the mixing chamber due to the LED. Hence, it is vital to place the LED in the center of and at a minimal distance from the measured Hall bar. An off-centered LED may also produce an inhomogeneous density distribution.

4.3.2 Self-adapting illumination process

In contrast to earlier used heterostructures, the samples produced from wafer #5 − 74 change their electron density highly nonlinear when illuminated. When a simple illumination sequence is used to get a series of magnetotransport measurements at varying

electron densities, wide ranges of densities are inevitably skipped. To cover a continuous range of densities, which is necessary for the analysis in chapter 6, a self-adapting illumination process was devised. A computer program determines the actual electron density and decides upon the illumination history and the next target electron density whether the LED power has to be increased or decreased in the following illumination step or wether magnetotransport data can be taken. As an additional benefit, much higher maximal densities are reached than by manual illumination: Small LED currents are used repetitively over a long period of time to reach the target density, so excessive heating is avoided. A more detailed description of the illumination process is given in Appendix C.

4.4   Data analysis

While a single magnetoresistance trace is sufficient for the Hofstadter butterfly discussion in chapter 5, further data analysis is needed for the study of quantum interference phenomena in 2D superlattices: Initially, magnetotransport curves for roughly equidistant steps in electron density are selected automatically from a measurement run. These are splined using base points on a reciprocal magnetic field axis and subsequently Fourier transformed to reveal $1/B$-oscillations. Finally a 2D-colorplot is assembled from the Fourier transforms obtained in this fashion. This colorplot reveals the density dependence of the frequency of each of the $1/B$-periodic oscillations. For this analysis it is essential to avoid artifacts when applying the fast Fourier transformation. The preparation steps necessary to achieve this are outlined in appendix A.

The standard analysis procedure to determine the electron density and other parameters goes as follows:

The longitudinal resistivity $\rho_{xx} = (V_{xx}/I)/(L/W)$ and Hall resistivity $\rho_{xy} = V_{xy}/I$ can be calculated from the measured voltage drops, the applied alternating current I and the geometry factor L/W. A field offset due to trapped flux in the superconducting magnet is corrected for by fitting a parabola to the longitudinal resistivity in the magnetic field range $[-0.01\,\mathrm{T}; 0.01\,\mathrm{T}]$. The apex value is the zero field longitudinal resistivity $\rho_{xx}|_{B=0}$ needed later on.

Next, the electron density n_s can in principle be estimated from both the slope of the Hall resistivity ρ_{xy} (Eqn. 2.19) and the $1/B$-periodicity of the Shubnikov-de Haas oscillations in ρ_{xx} (Eqn. 2.14). The electron density estimates in this work are not obtained from the Hall conductivity, since it might be suppressed at low B [89, 90]. This effect was seen

in recent experiments on weakly modulated samples [22] and is similar to what occurs in antidot experiments [91–93]. Moreover, in our experiments oscillations appear in ρ_{xy} at fields as low as $B \approx 0.1\text{T}$ for low temperatures due to the 2D modulation. Instead, the electron densities are taken from the Shubnikov-de Haas analysis. Since additional $1/B$-oscillations arise due to the 2D modulation (commensurability oscillations and miniband effects), a careful Fourier transformation as presented in appendix A is required to determine the Shubnikov-de Haas $1/B$-period.

Using the estimated electron density, the mobility can be calculated with the help of equation 2.18:

$$\mu = \frac{1}{e n_{\text{s}} \rho_{xx}|_{B=0}} \, . \tag{4.1}$$

As a consistency check, the lattice period

$$a = \frac{2\hbar\sqrt{2\pi n_{\text{s}}}}{e} \Delta\left(\frac{1}{B_{\text{CO}}}\right) \tag{4.2}$$

is determined from the observed commensurability oscillation $1/B$-periodicity $\Delta\left(1/B_{\text{CO}}\right)$ using equation 3.3.

As discussed in section 3.2.5, the modulation amplitude V_0 can be estimated for 1D modulated systems from the saturation field B_0 of the positive magnetoresistance. Using Eqns. 3.20 and 3.19, these estimates are

$$V_0^{\text{cl}} = \frac{\hbar}{\sqrt{2\pi}m^*} \cdot a B_0 \sqrt{n_{\text{s}}} \tag{4.3}$$

and

$$V_0^{\text{qm}} = \left[4\sqrt{2\pi}\,\frac{\hbar^3}{(m^*)^2 e} \cdot \frac{B_0}{a}\sqrt{n_{\text{s}}}\right]^{1/2} \, . \tag{4.4}$$

In appendix E, the suitability of Eqn. 3.20 for the 2D modulated case is motivated by results from the rectangular modulated samples in chapter 7.3. The saturation field of the positive magnetoresistance, B_0, is obtained by fitting a cubic polynomial in the range $[0\,\text{T}; 0.14\,\text{T}]$ to the longitudinal resistivity ρ_{xx}.

5 The Hofstadter Butterfly unveiled

In this chapter clear signatures of the fractal Hofstadter butterfly energy spectrum are presented. Additionally, the rearrangement and deformation of this spectrum due to Landau band coupling is shown for the first time.

5.1   Introduction

Gathering convincing experimental evidence for the Hofstadter butterfly spectrum has turned out to be challenging. A first glimpse of the spectrum was announced in Ref. [21] based on a study of the longitudinal resistivity ρ_{xx} only. Using also the Hall conductivity, precursors for the most prominent of all minigaps in the left and right wing of the butterfly were then reported for the regime where coupling between Landau bands can be ignored [22].

In the present work, the Hall conductance reaches its quantized value for the largest minigaps and many additional smaller minigaps are resolved. These improvements allow to investigate the so far inaccessible intermediate regime where neither the modulation nor the magnetic field can be viewed as a small perturbation and Landau band coupling becomes important.

These main findings will be presented using the single magnetic field sweep trace of ρ_{xx} and ρ_{xy} at the fixed electron density of $n_s = 4.32 \cdot 10^{11} \text{cm}^{-2}$ shown in Fig. 5.1. This measurement was carried out as described in section 4.2. For magnetic fields $B \lesssim 0.03\,\text{T}$, a positive magnetoresistance appears in the longitudinal resistivity ρ_{xx}. From this, the potential modulation strength can be roughly estimated using Eqn. 3.20. We find $V_0 \approx 0.6\,\text{meV} \approx 4\% E_\text{F}$.

To quantitatively understand the measurement, a comparison with the Hofstadter spectrum is mandatory. The Φ_0/Φ-axis on the top of Fig. 5.1 denotes the scope of the relevant Hofstadter butterflies. These butterflies are plotted in Fig. 5.2.

5.2   The major gaps in the butterfly

In this section we will focus on the strong magnetic field regime, where Landau bands are well separated.

Each butterfly has two major minigaps in each wing. They are expected to be observed the easiest. Each Landau band splits exactly into three subbands for the flux ratios $\Phi_0/\Phi = 1/3$ and $2/3$. Due to clustering of subbands, even at neighboring flux ratios subbands are arranged into three groups. The contribution to the Hall conductance of each Landau band goes either through the sequence $\sigma = \{0,0,1,1\}$ or $\sigma = \{0,1,0,1\}$ as the Fermi energy enters the various minigaps for B-fields near these flux ratios, depending on whether the flux ratio Φ_0/Φ is smaller or larger than 0.5. These Hall conductance sequences can easily be calculated using Eqn. 3.13 for the flux ratios $\Phi_0/\Phi = 1/3$ and $2/3$ respectively as demonstrated in section 3.1.2. They are also indicated in Fig. 3.6 and Fig. 5.2.

We will first discuss the more exotic non-monotonic Hall conductance sequence $\sigma = \{0,1,0,1\}$ for the right wing of the first butterfly ($0.5 < \Phi_0/\Phi < 1$ in Fig. 5.2). In the highlighted region between 0.6 and 0.7 T in Fig. 5.1, Landau band $n = 13$ and 14 are gradually populated as the magnetic field is lowered and the Fermi energy crosses the minigaps from the bottom to the top in the butterfly near $\Phi_0/\Phi = 0.6$. The Fermi energy does not trace a vertical line as Φ_0/Φ changes slightly upon lowering the field (for instance for band $n = 13$ Φ_0/Φ varies from 0.56 to 0.6). The Fermi energy jumps abruptly in gapped regions, but otherwise moves towards larger Φ_0/Φ with a slope determined by the number of available states as seen schematically for Landau band $n = 13$ in Fig. 5.2 (green line). This line can be calculated by determining for all flux ratios Φ_0/Φ up to which subband $j \in 1 \ldots p$ the Landau band is filled using Eqn. 5.3 (the electron density n_s is fixed). Since the Landau bands $n = 13$ and 14 are located far away from the flat band conditions marked by the dashed lines in Fig. 5.1, their internal gaps have non-zero width. The primary gaps that cause a three-fold splitting of the bands should be well resolved and we anticipate a clear Hall conductance sequence $\sigma = \{0,1,0,1\}$. To compare with experiment, the expected σ-sequence is plotted on an energy axis while taking the size of gaps in Fig. 5.2 as plateau widths (red trace in Fig. 5.3(b)). Subsequently, this curve is convoluted with a Gaussian of variance $(2.1\%\hbar\omega_\mathrm{c})^2$ to simulate disorder and
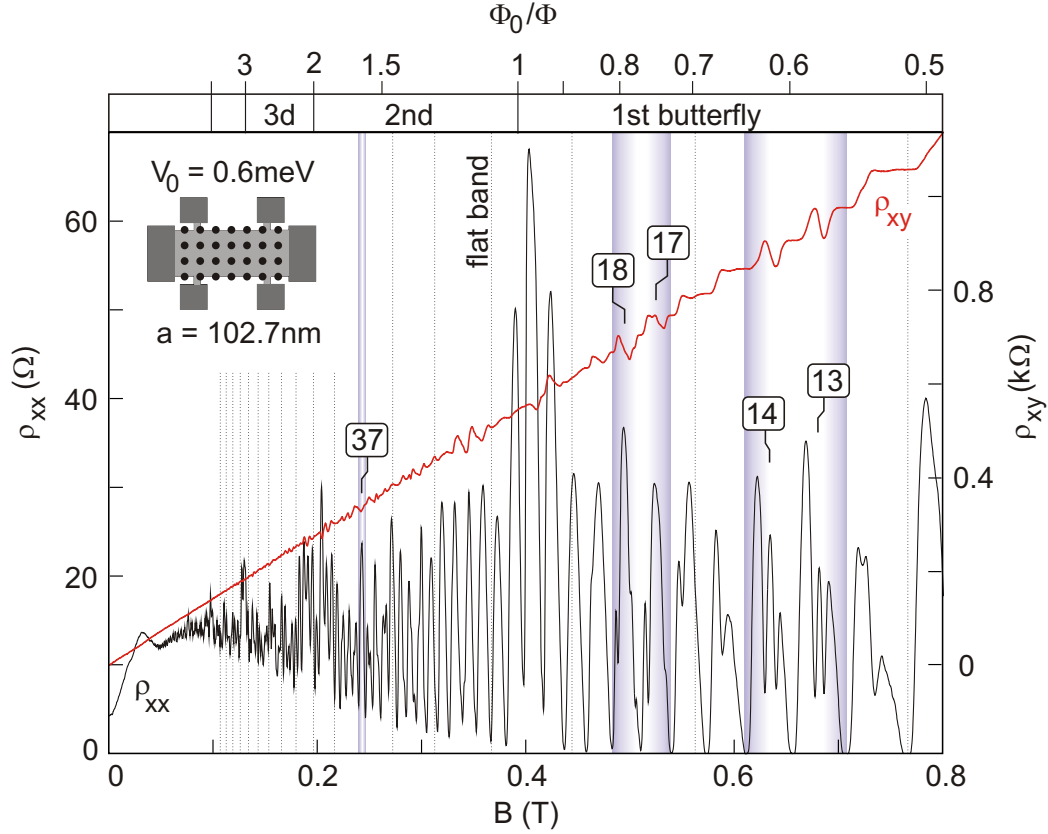
Figure 5.1:
The longitudinal and Hall resistivities for a modulated sample with period 102.7 ± 0.5 nm. The electron density is $n_s = 4.32 \cdot 10^{11} \text{cm}^{-2}$. Dotted lines mark flat band positions. The inset shows the sample geometry. Spin splitting is not resolved. Discussed Landau bands are denoted by their orbital index. The additional features within a Shubnikov-de Haas peak are evidence for a resolved Hofstadter butterfly spectrum. Violet color marks the field regions magnified in Fig. 5.3d), g) and Fig. 5.6. The complex oscillatory behavior at low field will be discussed in chapter 6.
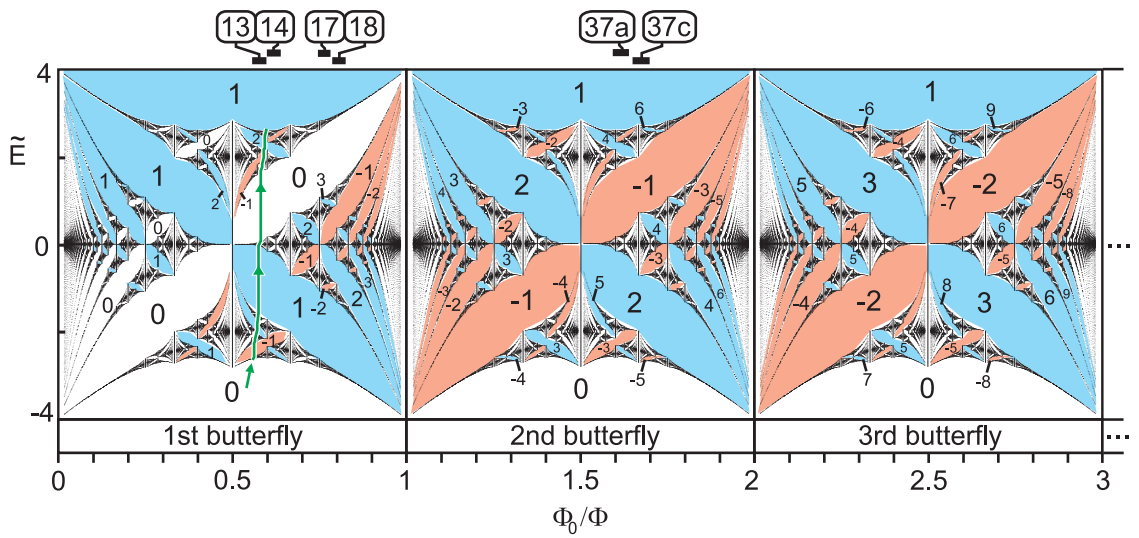
Figure 5.2:

The repeated Hofstadter butterfly as the internal energy spectrum common to all Landau bands. Hall conductance contributions of the partially filled Landau band when the Fermi energy is located in a minigap are indicated for the dominant gaps in units of $2e^2/h$. The green line traces the Fermi energy as Landau Band $n = 13$ is filled with decreasing flux. The Hall conductance contribution goes through the sequence $\sigma = \{0, 1, 0, 1\}$. For other bands the Φ_0/Φ range across which the Fermi energy moves as the band is filled is shown at the top. Φ is the magnetic flux through a superlattice unit cell, $\Phi_0 = h/e$ is the flux quantum.
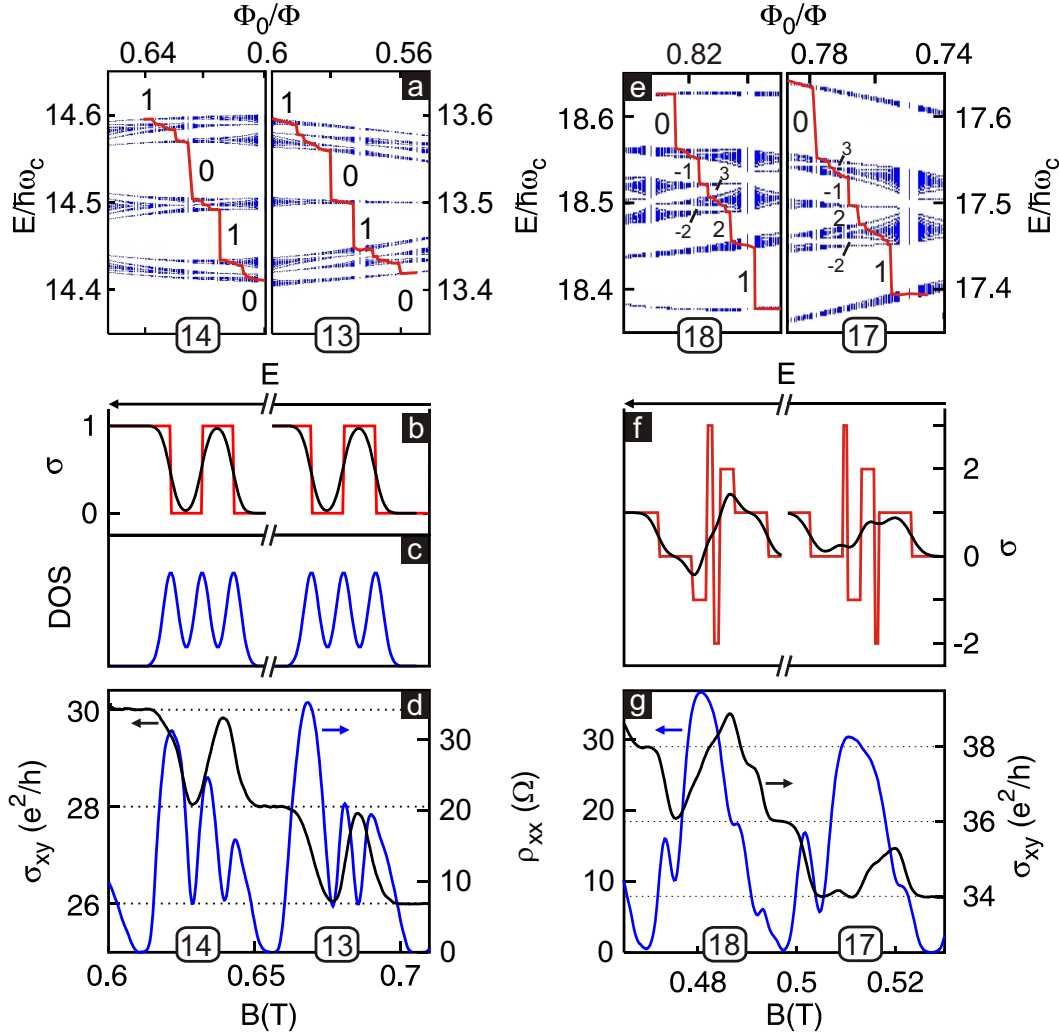
Figure 5.3:

The Hall conductance measurement and corresponding gaps in the butterfly: (a) Fermi energy traces for Landau bands $n = 14$ and 13, showing jumps across gaps and their respective Hall conductance values. (b) Hall conductance contribution σ for the same Landau bands in red, constructed from the biggest gap sizes as plateau widths and their respective Hall conductance values. The black lines are obtained after convolution with a fitted Gaussian of variance $(2.1\% \hbar \omega_c)^2$. (b) Schematic representation of the density of states. (c) The measured Hall conductance (black) and longitudinal resistivity (blue) for bands $n = 13$ and 14. (d) Fermi energy traces for Landau bands $n = 17$ and 18. (e) Same as in (a) but for bands $n = 17$ and 18 and a Gaussian of $(1.8\% \hbar \omega_c)^2$. (f) The experimental ρ_{xx} and σ_{xy} traces for bands $n = 17$ and 18.

temperature broadening (black trace in Fig. 5.3(b)). The variance serves here as a fitting parameter. This at first sight arbitrary procedure was chosen since a calculation of the Hall conductances for the dirty Hofstadter system is currently not available. It only exists for the here not applicable tight binding limit [94]. Motivated by the present work, a publication dealing with our case is however published recently by M. Koshino [95]. The non-monotonic behavior of Fig. 5.3(b) is already apparent in the Hall resistance measurement in Fig. 5.1. Fig. 5.3(d) displays a blown up version of the longitudinal resistivity ρ_{xx} in blue and the Hall conductance σ_{xy} in black. The latter is as usually obtained from the inversion of the resistivity tensor using Eqn. 2.17. This Hall conductance nearly reaches the quantized values in accordance with the curve predicted from the heuristic procedure described above. The quantization is accompanied by deep dips in ρ_{xx} which are due to the two main gaps in the butterfly according to Eqn. 2.21. Both observations are only possible because of the high quality of the device at hand.

In order to observe the Hall conductance contributions $\sigma = \{0,0,1,1\}$ typical for the other,"left" wing of the first butterfly ($\Phi_0/\Phi < 0.5$), magnetic fields higher than $B = 0.8\,\text{T}$ in Fig. 5.1 are needed. However at higher fields complications arise due to spin splitting. Hence, we show a measurement at smaller density n_s in Fig. 5.4 to avoid the issue. The already discussed three-fold splitting and the non-monotonic Hall conductance sequence typical for the "right" wing of the butterfly is observed again in the light blue area. For the other wing we will concentrate on Landau band $n = 8$, marked in pink. The shoulder close to $B = 1\,\text{T}$ together with the two peaks at lower B corresponds to the expected three-fold splitting. The measured Hall conductance is indeed monotonic and stays at the same quantized value during the field range for which the first subband is filled around $1\,\text{T}$. Then the Hall conductance increases abruptly by $2e^2/h$ when the Fermi energy is swept through the second subband. It keeps this quantized value while the third subband is filled. This is in accordance with the predicted $\sigma = \{0,0,1,1\}$-sequence. Note that for an unmodulated two-dimensional electron gas the Hall conductance is quantized only for the magnetic field range of the Shubnikov-de Haas minima in ρ_{xx} and varies continously in between them.

After successfully observing the major gaps in the butterfly using both ρ_{xx} and σ_{xy}, we will follow the same steps for higher order minigaps in order to verify the fractal characteristics of the spectrum.
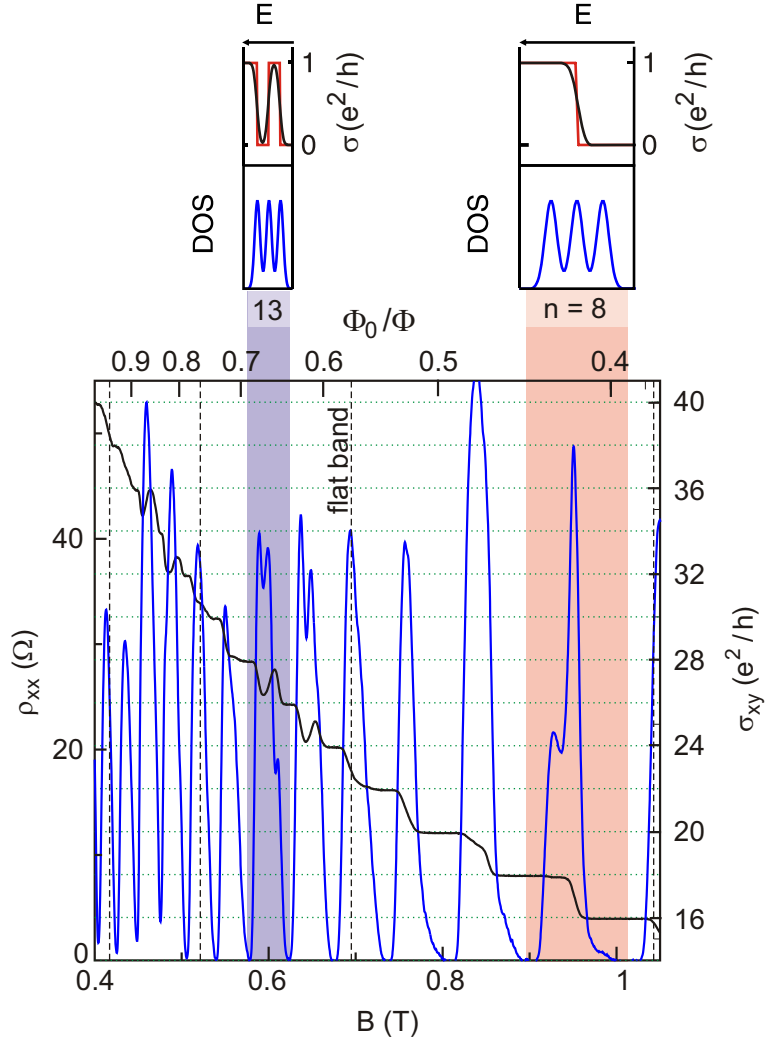
Figure 5.4:
Top: Expected Hall conductance contribution σ and the splitting in the density of states due to the major gaps in the first butterfly. Bottom: Transport data for the same samples as in Fig. 5.1, but at lower density $n_s = 3.95 \cdot 10^{11} \text{cm}^{-2}$ and mobility. Dashed lines mark flat band positions. The Hall conductance behavior is clearly different for $\Phi_0/\Phi \approx 1/3$ (left wing) and $\Phi_0/\Phi \approx 2/3$ (right wing).

5.3 Higher order gaps

Inspection of the fractal energy spectrum in Fig. 5.2 reveals that higher order minigaps of still sizeable but substantially reduced width open up at smaller fields to both sides of $\Phi_0/\Phi = 0.8 = q/p = 4/5$. Exactly at this flux ratio a Landau band splits into $p = 5$ subbands with a Hall conductance contribution sequence $\sigma = \{0, 1, 2, -1, 0, 1\}$ as seen in Fig. 5.2. To both sides of $\Phi_0/\Phi = 0.8$ additional much smaller minigaps come into play with contributions $\sigma = -2$ and 3. These contributions however occur at different positions in the main sequence $\sigma = \{0, 1, 2, -1, 0, 1\}$ depending on whether the Fermi energy passes on the right ($\sigma = \{0, 1, 2, -\mathbf{2}, \mathbf{3}, -1, 0, 1\}$) or left ($\sigma = \{0, 1, -\mathbf{2}, 2, -1, \mathbf{3}, 0, 1\}$) side of $\Phi_0/\Phi = 0.8$ through the spectrum. So analogous to the previous section, we can again look for changes in the Hall conductance when comparing the filling of the Landau band on the left or right side of $\Phi_0/\Phi = 0.8$. Landau bands $n = 17$ and 18 are the most suitable candidates as they are also centered between the next pair of flat band conditions (cf. Fig. 5.1). Fig. 5.3(e) shows traces of the Fermi energy in red as the Landau bands $n = 17$ and 18 are filled with decreasing magnetic field. The more complex and distinct series of consecutive Hall conductance values when filling the bands are plotted in red in Fig. 5.3(f). After applying the heuristic procedure mentioned above with a Gaussian of $(1.8\%\hbar\omega_c)^2$ variance, all features including the weak shoulders and dents seen in the black Hall conductance trace of Fig. 5.3(g) are reproduced. These fine features can not be explained without invoking the much smaller minigaps, which contribute a Hall conductance of $\sigma = 3$ and -2. Hence we have delved experimentally deeper into the self-replicating structure of the Hofstadter butterfly spectrum than ever before. The ability to resolve such tiny minigaps in the Hofstadter spectrum is also the crucial prerequisite, which was previously not satisfied, to investigate the intermediate field regime where Landau band coupling can no longer be ignored.

5.4 Landau band coupling effects

The Hofstadter butterfly spectrum appearing in Fig. 5.2 is valid only if Landau band coupling can be neglected. This is the case for large magnetic fields ($\hbar\omega_c \gg V_0$). As we decrease the magnetic field for a fixed potential modulation V_0, we enter the intermediate regime where neither the modulation nor the magnetic field can be viewed as a small perturbation. Obermayr and Schellnhuber *et al.* [96–98] were first to calculate the spectrum for this regime and even larger values of V_0, but only for a few selected values of Φ_0/Φ. Spectra for full ranges of Φ_0/Φ were calculated later by Springsguth and Ket-
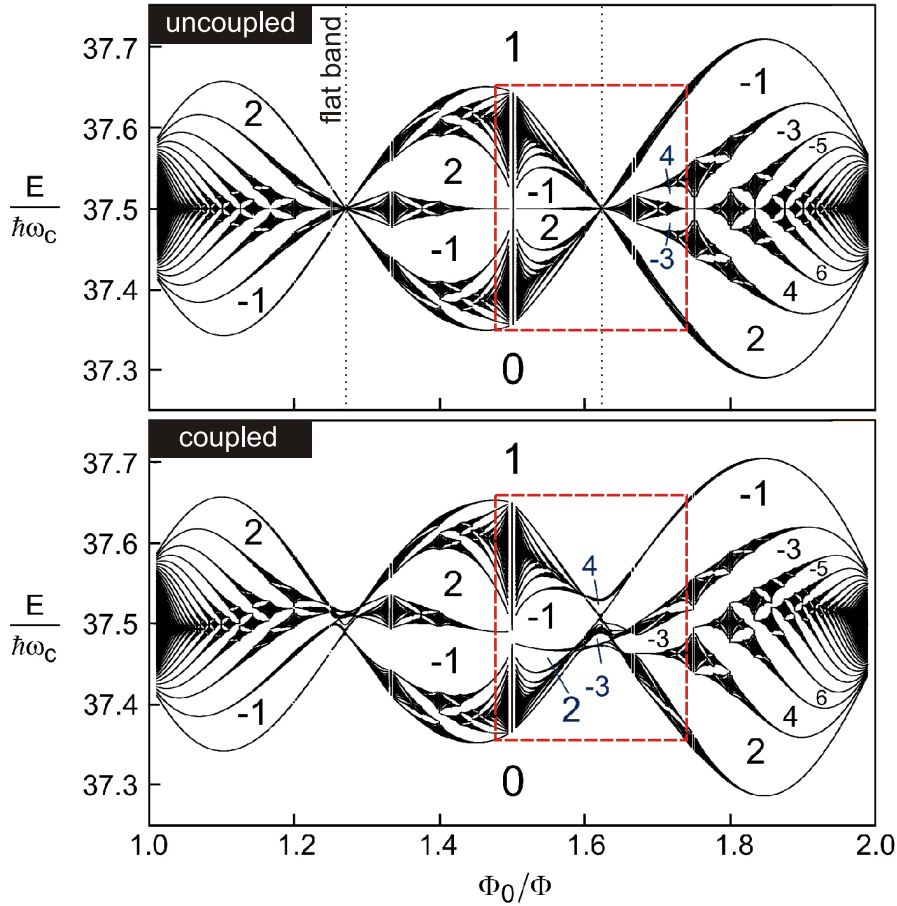
Figure 5.5:
Top: Calculation of the internal spectrum of Landau band $n = 37$ for $K = 2\pi m^\star a^2 V_0 / h^2 = 2$ ignoring coupling with other bands for the Φ_0/Φ range covered by the second Hofstadter butterfly. The energy is divided by the cyclotron energy for clarity. Hall conductance contributions for major gaps are indicated. Bottom: Same as the top spectrum, but with coupling between the six nearest neighboring bands taken into account. The symmetry is broken and deformations are visible. The red boxes mark the zoomed region used in Fig. 5.6. The white regions surrounding $\Phi_0/\Phi = 1.5$ are an artefact. For these values of Φ_0/Φ calculations become prohibitively time consuming.

zmerick *et al.* [23][1]. They characterized the Landau band coupling strength by a single dimensionless parameter

$$K = \frac{2\pi}{h^2} m^\star a^2 V_0 \tag{5.1}$$

independent of the magnetic field. For $K > 0$, coupling is predicted to lift the flat band condition, distort the butterfly and eventually rearrange subbands. Due to these changes, the spectrum is no longer universal to all Landau bands but now depends on the orbital index n.

5.4.1   Anomalous Hall conductance contributions

For a rearrangement of subbands some minigaps in the spectrum have to close and new ones open up. If the Fermi energy is in such a new minigap, the Hall conductance contribution is changed compared to the same gap g in the uncoupled spectrum. The Diophantic equation 3.13 is no longer valid. Only if the constraint $|w| \leq p/2$ is dropped, Eqn. 3.13 remains valid, but is no longer unambiguous for a given set of p, q and g [99, 100]. So one has to resort to a different formula due to Středa [62]: The change in the number of filled states per unit area $N(E)$ below the minigap at energy E with varying magnetic field has to be calculated to get the Hall conductivity contribution

$$\sigma = \frac{\partial N(E)}{\partial B} \frac{h}{e} . \tag{5.2}$$

Since σ is quantized within the minigap, it is possible to replace $\partial N(E)/\partial B$ by $\Delta N(E)/\Delta B$ for all flux ratios $p_i/q_i = B_i \cdot ea^2/h$ ($i = 1, 2$), which share the same minigap [23]. With the number of states per unit area in one of the p_i subbands,

$$N_{\text{subband}} = eB_i/hp_i , \tag{5.3}$$

and the number of subbands below the gap n_i Eqn. 5.2 becomes

$$\sigma = \frac{n_1 q_2 - n_2 q_1}{p_1 q_2 - p_2 q_1} . \tag{5.4}$$

This equation is necessary to calculate the σ-values for Figs. 5.5 and 5.6.

Summing up, the change in number of states below a certain minigap due to rearrangement of the spectrum will lead to a change in σ. Minigaps with unexpected Hall conductance contributions emerge.

---

[1] In the nomenclature of Ref. [23], variables p and q are interchanged.

5.4.2   Experimental evidence

Coupling between Landau bands has been extensively investigated in theory in Ref. [23], but experimental evidence remained elusive. These calculations were for the first butterfly and Landau band indices $n \leqslant 14$. For the device used in the present work, a rough estimate for V_0 from the positive magnetoresistance near zero field suggests a coupling parameter K of order 1. Hence coupling is important only at low magnetic fields which correspond to flux ratios $\Phi_0/\Phi \gtrsim 1$ and Landau bands $n \gtrsim 30$. In collaboration with R. Ketzmerick and B. Naundorf, the calculations of Ref. [23] were extended to handle Landau levels with higher orbital indices and Φ_0/Φ values in the range for the second butterfly. The lower panel of Fig. 5.5 depicts such a calculation for band $n = 37$, the second butterfly and a coupling parameter $K = 2$. The contribution σ to the Hall conductance of band $n = 37$ when the Fermi energy is located in selected minigaps is calculated using Eqn. 5.4. Contrary to Eqn. 3.13, this formula holds also for the coupled Landau band case. A comparison with the upper panel, where coupling effects are neglected, helps to identify the influence of band coupling: For the in Fig. 5.5 depicted second butterfly, small coupling values K already produce significant effects. The first butterfly on the other hand is not significantly affected at these small K-values, as seen in Fig. 5.3(a) and (e), where coupling is taken into account. This can be understood since in Fig. 3.2(b) Landau bands get close for high Φ_0/Φ values and to avoid band crossings the spectrum will rearrange. The strongest impact of coupling appears near the flat band locations $\Phi_0/\Phi \approx 1.25$ and 1.65 of the uncoupled case. The macroscopic degeneracy is lifted and, in comparison with the uncoupled case, subbands rearrange and minigaps with unexpected Hall conductance values appear. Away from the zero band width region the spectrum is still distorted and the vertical symmetry is broken. No rearrangements occur. Nevertheless, minigaps open up between so-called kissing bands. An example occurs exactly at $\Phi_0/\Phi = 1.5$. Such additional minigaps are however hard to verify experimentally since no new Hall conductance sequences arise due to these minigaps. Furthermore the energy spectrum in these regions changes rapidly, so these minigaps are very sensitive to disorder broadening and small changes in Φ_0/Φ.

Hence, the best place to look for coupling effects is at high Φ_0/Φ values and near the 'flat' band position of the uncoupled case. Signatures of band coupling are additional shoulder structures in ρ_{xx} as well as a non-monotonic behavior in the Hall conductance σ_{xy}. This motivates and justifies our choice of the 37th Landau band situated right at a flat band condition in the 2nd butterfly to look for Landau band coupling signatures (see Fig. 5.1).

The bottom panel of Fig. 5.6 displays the Hall conductance for six carrier densities rang-
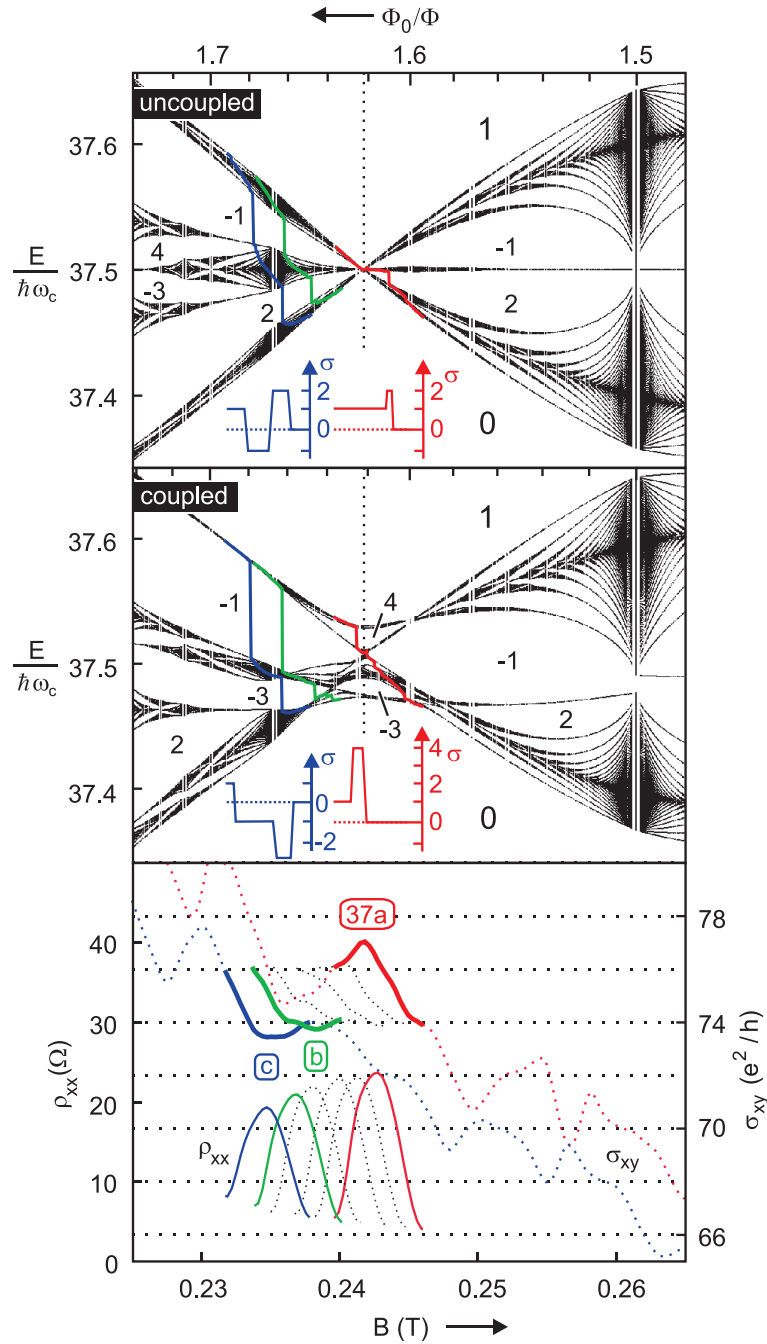
Figure 5.6:

Consequences of Landau band coupling: Top: Calculation of the internal spectrum of Landau band $n = 37$ ignoring coupling with other bands. Hall conductances for major gaps are indicated. Middle: Deformations due to coupling. As in the top panel, traces of the Fermi energy are plotted for three electron densities. Two Hall conductance traces are shown in blue and red as insets. Bottom: the measured Hall conductance for n_s from $4.32 \cdot 10^{11} \text{cm}^{-2}$ for **a** to $4.17 \cdot 10^{11} \text{cm}^{-2}$ for **c**. The longitudinal resistivity is plotted for each Hall conductance trace to mark the B-field region where the Landau band $n = 37$ is filled.

ing from $n_{\mathrm{s}} = 4.32 \cdot 10^{11} \mathrm{cm}^{-2}$ for **a** to $4.17 \cdot 10^{11} \mathrm{cm}^{-2}$ for **c**. Trace **a** is identical with the Hall conductance trace of Fig. 5.1. For the sake of clarity, the Shubnikov-de Haas peaks have been added. They demarcate the field interval across which the 37th level is filled. The Hall conductance traces **a** to **c** are plotted as thick lines. To compare the experimental data with theory, the appropriate field range of the calculated Landau bands in Fig. 5.5 is repeated in the top two panels of Fig. 5.6. They are of course only valid for band $n = 37$. For the densities **a**,**b** and **c**, the calculated behavior of the Fermi energy has been included in the top two panels.

First focus on the red curve for the highest carrier density as the magnetic field is lowered. In the single band approximation shown at the top the Fermi energy crosses a gap with $\sigma = 2$ during the *initial* stage of filling this band. The only sizeable gaps available after this jump have a negative $\sigma = -1$. This contradicts the experimental data, where an overshoot appears during the second half of populating the band. Instead, the behavior fits the numerical data with Landau band coupling, where the Fermi energy passes a $\sigma = 4$-gap when the band has been filled more than half. The small size of the gap unfortunately prevents the Hall conductance from reaching its quantized value. Note that the corresponding Shubnikov-de Haas peak is featureless. It emphasizes once more the importance of the Hall conductance to gain detailed information about the Hofstadter spectrum.

The data at lower carrier densities again confirms that Landau band coupling plays a dominant role. Due to band coupling, the large gap with $\sigma = 2$ has closed and a gap with $\sigma = -3$ has taken its place. The consequences of this rearrangement for the Hall conductivity are depicted schematically in the blue insets of Fig. 5.6. For the uncoupled case, a positive Hall conductance contribution $\sigma = 2$ is followed by a negative $\sigma = -1$. This switching behavior is recognizable in the Hall conductance for other bands at higher and lower flux ratios, but the traces for $n = 37$ differ: For both curves **b** and **c**, the Hall conductance drops 'negative' instantly as the band is being filled. Curve **b** even develops its absolute minimum as the Fermi energy reaches the first significant gap (with $\sigma = -3$) in the spectrum. Both of these observations disagree with the positive contribution to the Hall conductance of $\sigma = 2$ predicted by the single band approximation. The blue calculated Hall conductance trace for the coupled case nicely explains the behavior in experiment.

In conclusion, owing to significant advances in sample quality and fabrication, it is now possible to resolve higher order minigaps in Hofstadter's energy spectrum with recourse to the quantum Hall effect as a diagnostic tool. This progress has offered experimental access to the hitherto-unexplored regime where Landau band coupling further enriches the physics of this model problem with fractal nature, which arises in many different

physical contexts.

6 Quantum interference in square lattices

In this chapter we demonstrate and discuss quantum interferences unique to a 2D artificial crystal. The 2D artificial crystal is realized by modulating a 2D electron system in two directions. In such a system, electrons are Bragg reflected at the Brillouin zone boundaries (BZB) of the artificial lattice, where energy gaps appear. In a B-field, electrons move on constant energy contours in k-space, which deviate from the free electron contours due to the gaps at the BZB. Both closed and open electron trajectories emerge. At sufficiently large B-field, magnetic breakdown allows tunneling across the gaps at the BZB, and enables an entirely new network of closed electron paths. These paths enclosing different areas in k-space produce additional $1/B$-periodic oscillatory features in the transport quantities. In addition, quantum interferences of certain pairs of electron paths, which share the same starting and ending point, give rise to a novel type of $1/B$ oscillations for 2D artificial crystals. Their periodicity is also proportional to the enclosed area in k-space. An electron density dependent study is instrumental to identify the relevant orbits and groups of interfering paths. We present a Monte Carlo approach which finds the plethora of new orbits and quantum interferences responsible for the oscillations observed in our experiment.

6.1 Oscillations in the magnetotransport measurement

We know from section 3.2 that miniband effects should be observable in a magnetotransport measurement as $1/B$-oscillations. So we replot the longitudinal transport data of Fig. 3.1 as a function of $1/B$.
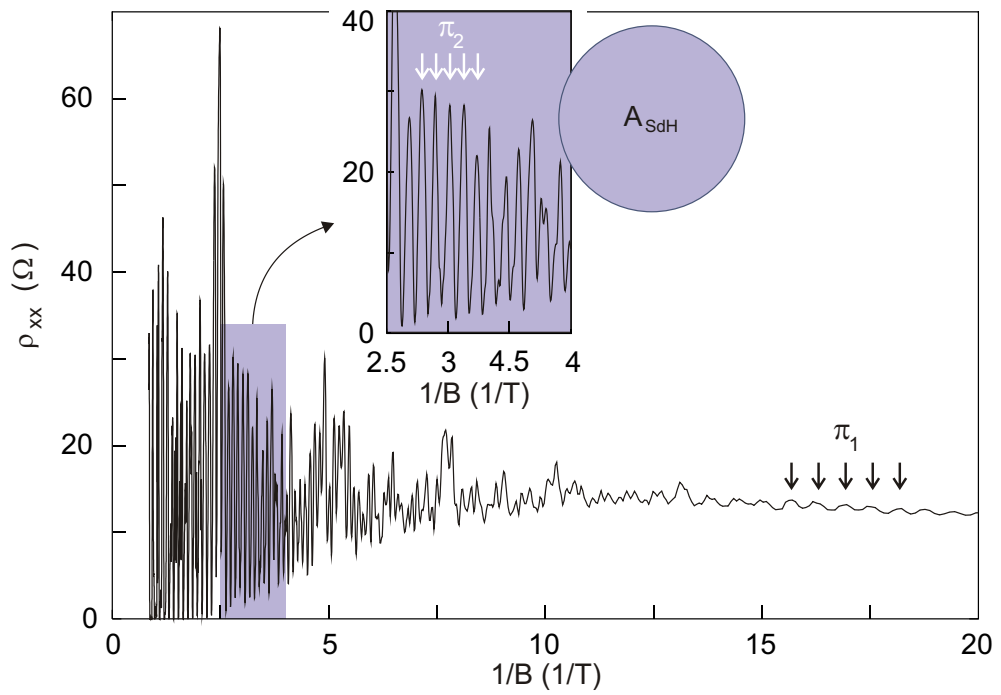
Figure 6.1:
The longitudinal resistivity ρ_{xx} shown in Fig. 3.1 of the modulated sample plotted versus $1/B$.
Two oscillation patterns with different $1/B$-periodicities π_1 and π_2 are marked. The oscillations
with period π_2 correspond to the Shubnikov-de Haas oscillations of the unmodulated system.

Several oscillation patterns with a different periodicity are already visible in the raw data of Fig. 6.1. Using Eqn. 2.22, we know that the oscillation period $\pi_1 \approx 0.61/\text{T}$ corresponds to an electron trajectory which encloses an area $A_1 = 1.5 \cdot 10^{16}/\text{m}^2$ in k-space. This is four times larger than the area of the first Brillouin zone, $A_{\text{BZ}} = K_a^2 = 0.4 \cdot 10^{16}/\text{m}^2$. The second period $\pi_2 \approx 0.11/\text{T}$ is just the Shubnikov-de Haas oscillation period expected for an unmodulated sample with the same electron density $n_{\text{s}} = 4.3 \cdot 10^{11}\text{cm}^{-2}$. It corresponds to the Fermi circle in the left panel of Fig. 3.7a, with an area $A_2 = A_{\text{SdH}} = \pi k_{\text{F}}^2 = 8.7 \cdot 10^{16}/\text{m}^2$, six times larger than A_1.

To find all the different $1/B$-periodicities, the data of Fig. 6.1 is Fourier transformed. The magnetic field range used is 0.04 T to 1.1 T, so that neither the positive magnetoresistance at low B nor the spin splitting at high B is picked up. The details of how the Fourier transform is carried out to ensure that low frequencies are properly resolved can be found in appendix A.

In Fig. 6.2 more oscillations are visible than expected from the three types of closed trajectories found in the right panel of Fig. 3.7c. This is not surprising, since this panel corresponds to a density of $n_{\text{s}} = 0.4 \cdot 10^{11}\text{cm}^{-2}$ for a period $a = 100\,\text{nm}$. The experimental data, however, is taken at an electron density $n_{\text{s}} = 4.3 \cdot 10^{11}\text{cm}^{-2}$, at which many more minibands are filled.

6.2   The miniband structure

In the samples at hand we can vary the electron density from $2.9 \cdot 10^{11}\text{cm}^{-2}$ to $4.3 \cdot 10^{11}\text{cm}^{-2}$. To compare with the experiment, the band structure in the right panel of Fig. 3.7b is extended to higher energies. The result can be seen in Fig. 6.3a. There, the Fermi energy for a representative density of $n_{\text{s}} = 3.4 \cdot 10^{11}\ \text{cm}^{-2}$ is marked with a dotted line. Red circles along this line highlight energy gaps. Some of them are not clearly resolved in spite of the in comparison with experiment exaggerated modulation amplitude of $V_0 = 2$ meV. Gaps open up along the line $\text{M} - \Gamma$, since the modulation potential used in the band structure calculation has the form

$$
\begin{aligned}
V(x,y) & = V_0 \left(\cos\frac{\pi x}{a} \cdot \cos\frac{\pi y}{a} \right)^2 \\
& = \frac{V_0}{4} \left(1 + \cos\frac{2\pi x}{a} + \cos\frac{2\pi y}{a} + \frac{1}{2}\cos\frac{2\pi(x+y)}{a} + \frac{1}{2}\cos\frac{2\pi(x-y)}{a} \right) .
\end{aligned}
\tag{6.1}
$$
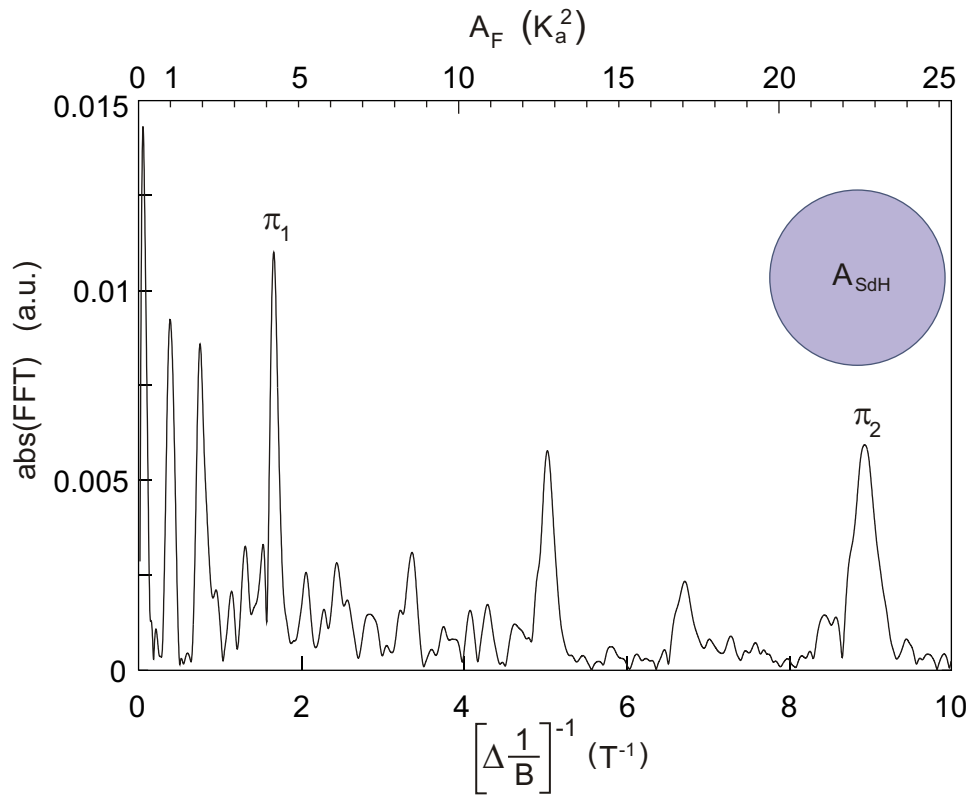
Figure 6.2:
The Fourier transformation of the longitudinal resistivity ρ_{xx} shown in Fig. 5.1. The oscillations with periods π_1 and π_2 of Fig. 6.1 are clearly visible. Each $1/B$-oscillation corresponds to an electron trajectory which encloses an area A_F in k-space. The top axis shows A_F in units of the first Brillouin zone area K_a^2.
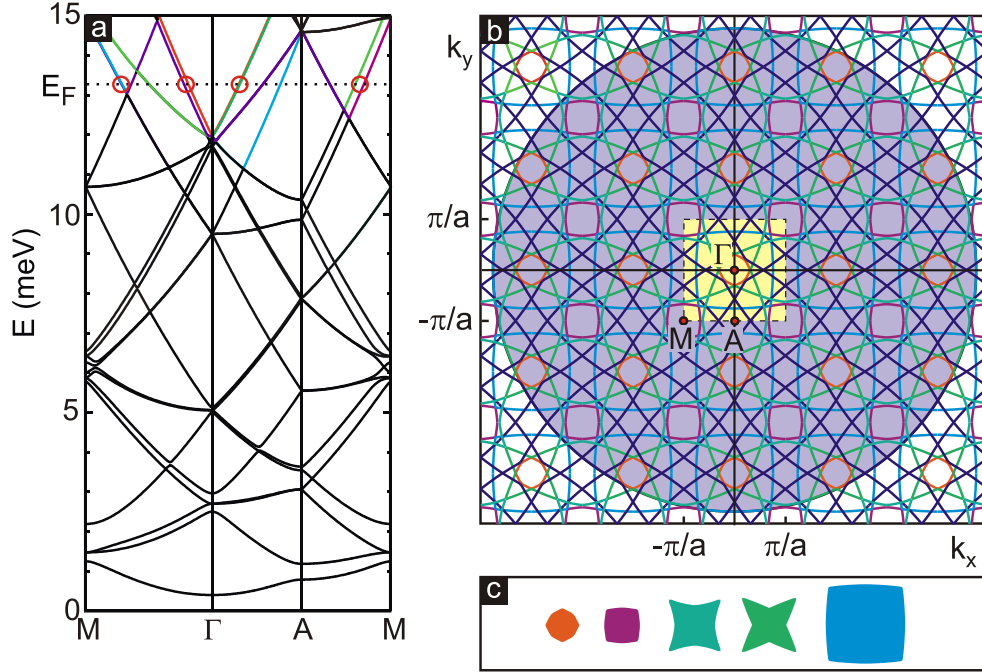
Figure 6.3:

(a) The band structure for the two-dimensional modulation in Eqn. 6.1, with period $a = 100$ nm and amplitude $V_0 = 2$ meV. This graph is taken from [64]. For a sample with electron density $n_s = 3.4 \cdot 10^{11}$ cm^{-2}, the Fermi energy lies at $E_F = 13.2$ meV (dotted line). (b) The repeated zone scheme for this Fermi energy. The main and diagonal Fourier components in Eqn. 6.1 are responsible for the gaps at the first and second Brillouin zone boundaries. The resulting open and closed Fermi contours have different colors. The first Brillouin zone is demarcated in yellow. (Based on [101]). (c) The closed trajectory types requiring no tunneling found in (b).

We can rewrite this potential as a Fourier expansion (3.14) with the four main coefficients $V_{K_a \cdot (\pm 1, 0)} = V_{K_a \cdot (0, \pm 1)} = V_0/8$ and four diagonal coefficients $V_{K_a \cdot (\pm 1, \pm 1)} = V_0/16$. We use this type of modulation potential to illustrate the influence of diagonal Fourier coefficients, since they play a role in the experiments presented here, as discussed later in section 6.4.3. The diagonal components bring about gaps along higher order Brillouin zone boundaries. The line $M - \Gamma$ is part of the boundary of the second Brillouin zone.

The k-space periodic zone scheme in Fig. 6.3b corresponds to the chosen value of the Fermi energy. In this figure, the Fermi circle for an unperturbed system is filled with purple color. As a result of the high electron density, its radius k_F is more than twice the width $K_a = 2\pi/a$ of the Brillouin zone. Due to the two-dimensional character of

the modulation, the large Fermi circle folds back into the first Brillouin zone, which is highlighted in yellow. Depending on the particular Fourier components present in the modulation potential, complicated electron trajectories are created, including runaway trajectories that do not close.

In Fig. 6.3b and c five closed trajectories are found which would correspond to only five oscillations in ρ_{xx}. These are not sufficient to explain the large number of oscillations found in Fig. 6.2. Furthermore, the five closed trajectories seen in Fig. 6.3c enclose areas *smaller* than the first Brillouin zone. Most of the peaks in the Fourier transform in Fig. 6.2 however correspond to enclosed areas *larger* than the first Brillouin zone.

6.3   Magnetic breakthrough

Both aforementioned issues are resolved by the well known phenomena of *magnetic breakthrough*, which was discussed in subsection 3.2.3. It allows for tunneling across energy gaps at the Brillouin zone boundary with a *B*-field dependent probability $P_{\mathbf{q}}$, so that additional closed trajectories may be traced by the electrons at the Fermi energy.

It turns out to be quite a challenge for a two-dimensionally modulated system to find the most probable of these orbits in view of their large number: At high magnetic fields the tunneling probability approaches 1 and electrons tunnel across all the gaps. Hence, the electrons encircle the Shubnikov-de Haas orbit. At lower fields, magnetic breakthrough occurs with high probability only for certain gaps and other closed trajectories than the high field Shubnikov-de Haas orbit dominate. Many such closed trajectories are possible: The first Brillouin zone shown in yellow in Fig. 6.3b is subdivided into 56 different small basic shapes by the intersecting electron trajectories. The number and form of these basic shapes changes drastically with k_{F} and thus with the electron density. A possible electron trajectory is the circumference of any area pieced together from these basic shapes, provided the circumference is convex. A few trajectories which are possible when magnetic breakthrough is taken into account for the case in Fig. 6.3 are presented in Fig. 6.4. In this Figure, tunneling events are not marked, since they are too frequent and would clutter the entire periphery. Instead, green dots mark gaps where an electron stays on its track and does not tunnel. Each of these areas consists however of 700 and more basic shapes. One can already obtain the idea that combinatorially many such trajectories must be possible, much more than oscillations observed in experiment. In order to compare with experiment, we therefore need to determine the probability of all of these trajectories and select the most probable ones.
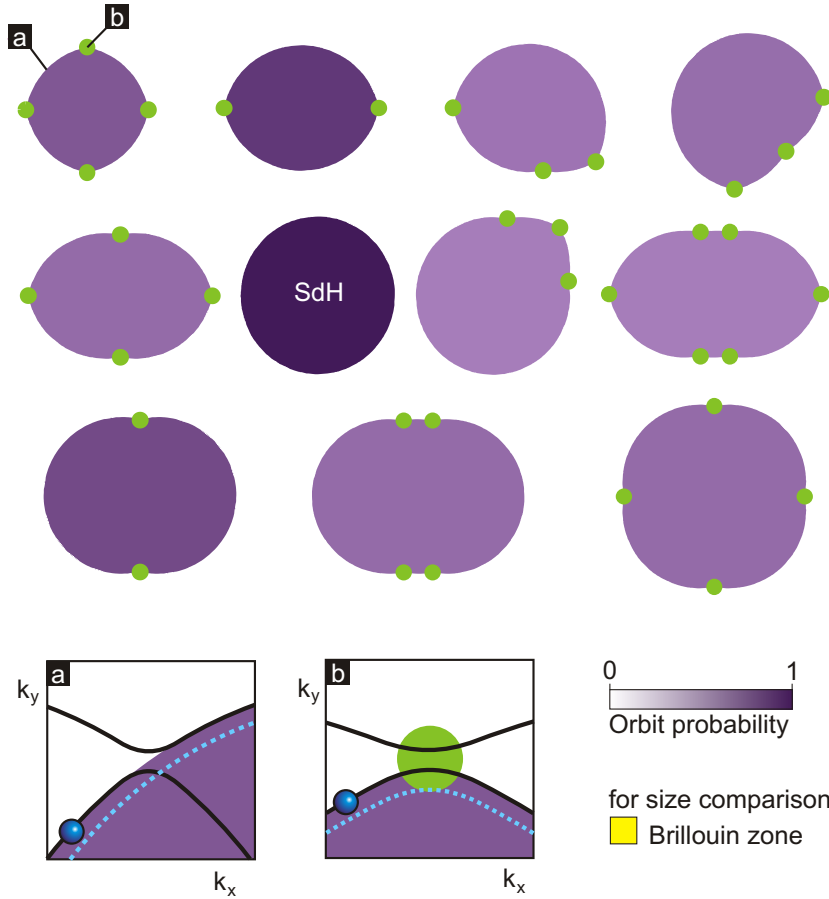
Figure 6.4:
A few closed electron trajectories which are possible due to magnetic breakthrough. Green dots mark gaps where electrons do not tunnel. Gaps where the electron does tunnel are not marked, since they are too frequent and would clutter the entire picture. Inset (a) shows pictorially a gap where the electron tunnels. Inset (b) illustrates one where it does not tunnel.

6.3.1   Tunneling probability

We already introduced the tunnel probability

$$P_{\mathbf{q}}(k_{\mathrm{F}}, K_a, V_0^2/B) = \exp\left(-\frac{\pi \Delta E_{\mathbf{q}}^2}{4\hbar \omega_{\mathrm{c}} E_{\mathrm{F}} \sin(2\theta_{\mathbf{q}})}\right) \tag{6.2}$$

in Eqn. 3.18. At each gap corresponding to an intersection of two Shubnikov-de Haas circles with distance $\mathbf{q}$ the electron can either tunnel with probability $P_{\mathbf{q}}(k_{\mathrm{F}}, K_a, V_0^2/B)$ or stay on its track with probability $Q_{\mathbf{q}}(k_{\mathrm{F}}, K_a, V_0^2/B) = 1 - P_{\mathbf{q}}(k_{\mathrm{F}}, K_a, V_0^2/B)$.

When calculating the round-trip probability $P_{\mathrm{total}}(k_{\mathrm{F}}, K_a, V_0^2/B)$ of a trajectory, we count how often an electron on the trajectory has to tunnel over a gap with probability $P_{\mathbf{q}}(k_{\mathrm{F}}, K_a, V_0^2/B)$. This number is $n_{\mathbf{q}}^{\mathrm{tunnel}}$. We repeat the same count for non-tunnel events and get $n_{\mathbf{q}}^{\mathrm{non-tunnel}}$. The round-trip probability of a closed trajectory is then

$$P_{\mathrm{total}}(k_{\mathrm{F}}, K_a, V_0^2/B) = \prod_{\mathbf{q}} P_{\mathbf{q}}^{n_{\mathbf{q}}^{\mathrm{tunnel}}} Q_{\mathbf{q}}^{n_{\mathbf{q}}^{\mathrm{non-tunnel}}}. \tag{6.3}$$

Since the computation cost to calculate the probability $P_{\mathrm{total}}(k_{\mathrm{F}}, K_a, V_0^2/B)$ of all trajectories would be prohibitive, we devised a Monte Carlo method which finds the most probable orbits first. Note that this problem is unique to two-dimensional modulation. For a one-dimensional modulation, the most probable orbits can be guessed easily [14].

6.3.2   The Monte Carlo simulation

One possibility to find the most probable closed trajectories is to walk along the segments of the Fermi circles just like an electron does. At each intersection of two circles with distance $\mathbf{q}$, the probability for tunneling, $P_{\mathbf{q}}(k_{\mathrm{F}}, K_a, V_0^2/B)$, is determined.

The necessary parameters are chosen in the following way: The Fourier component responsible for the energy gap $\Delta E_{\mathbf{q}}$ at the intersection and the Bragg scattering angle $\theta_{\mathbf{q}}$ are determined from the exact geometry of the intersection. This geometry is governed by k_{F} and $K_a = 2\pi/a$. These two parameters are fixed for a simulation run, since the period a and electron density are known from experiment. The choice for B, V_0 and for the Fourier components of the modulation potential, $V_{\mathbf{q}} = V_0 \cdot \alpha_{\mathbf{q}}$, will be motivated after the discussion of the experimental results in the next section.
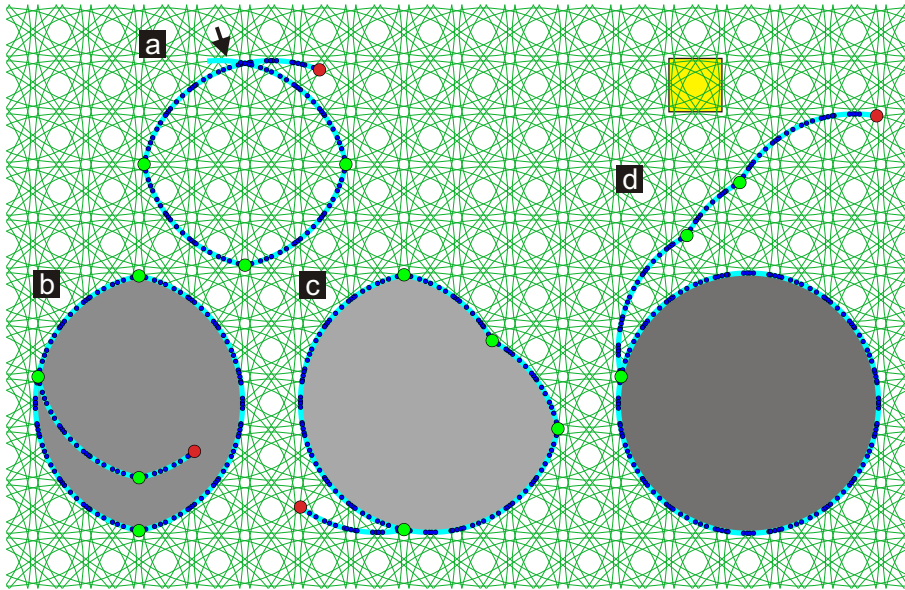
Figure 6.5:

Possible outcomes of a simulated electron walk through the reciprocal lattice. Start points are red. Small blue dots mark tunnel events, big green dots mark intersections where the electron stays on its track and changes from one Fermi circle to another. a) An example of a trajectory, which does not close properly (arrow). b-d) Examples of closed electron trajectories, including the starting trail from the simulation. A Brillouin zone is drawn as yellow square for reference.

According to the calculated probability $P_\mathbf{q}$, the electron either tunnels or stays on its Fermi surface until it reaches the next intersection. The whole process is repeated until a closed trajectory is formed.

Typical results of such a simulated electron walk through the extended zone scheme are illustrated in Fig. 6.5. The green repeated zone scheme is constructed in the limit of a vanishing modulation potential $V_0 \to 0$. All gaps are infinitesimally small but the modulation potential still defines the Brillouin zones and leads to a repetition of the Fermi circle at reciprocal vectors $\mathbf{q}$. The red dots are the starting points for the simulation. During one iteration, each intersection of two Fermi circles in a half open quarter Brillouin zone $(0; \pi/a] \times (0; \pi/a]$ is taken as starting point. Thus intersections lying on the border of the quarter Brillouin zone are taken into account only once. From each starting point, the simulation will start a random walk four times, one for each possible direction. This random walk will continue until it hits its own track or at most for 10.1 times the total number of possible tunnel events on a Fermi circle circumference. If the random walk does not cross its own track until this cutoff count, it is discarded. This cutoff speeds up the simulation and is justified for small $[\Delta(1/B)]^{-1} \leq 10$ as in Fig. 6.6. If the trajectory closes, the electron is followed one more step to determine whether this step is in the same direction as the old track and thus the trajectory really closes. If this is not the case, like for trajectory (a) in Fig. 6.5, again the trajectory is discarded. If on the other hand a trajectory closes properly, its starting trail, which is not part of the closed trajectory, is cut off. Examples of such starting trails are included in Fig. 6.5. Notice that starting trails may be in- or outside of the orbits found. Both the area enclosed by the trajectory and its probability $P_\text{total}(k_\text{F}, K_a, V_0^2/B)$ are calculated. The area is approximated using a polygon and refined by adding or subtracting missing circle segments. Statistics are kept of how often each orbit is found, including its rotated, mirrored and translated variants[1]. For each such orbit type one representative is saved to be accessible later on. The simulation stops after finding more than 1000000 orbits. We will now outline how the result of the simulation compares with experiment.
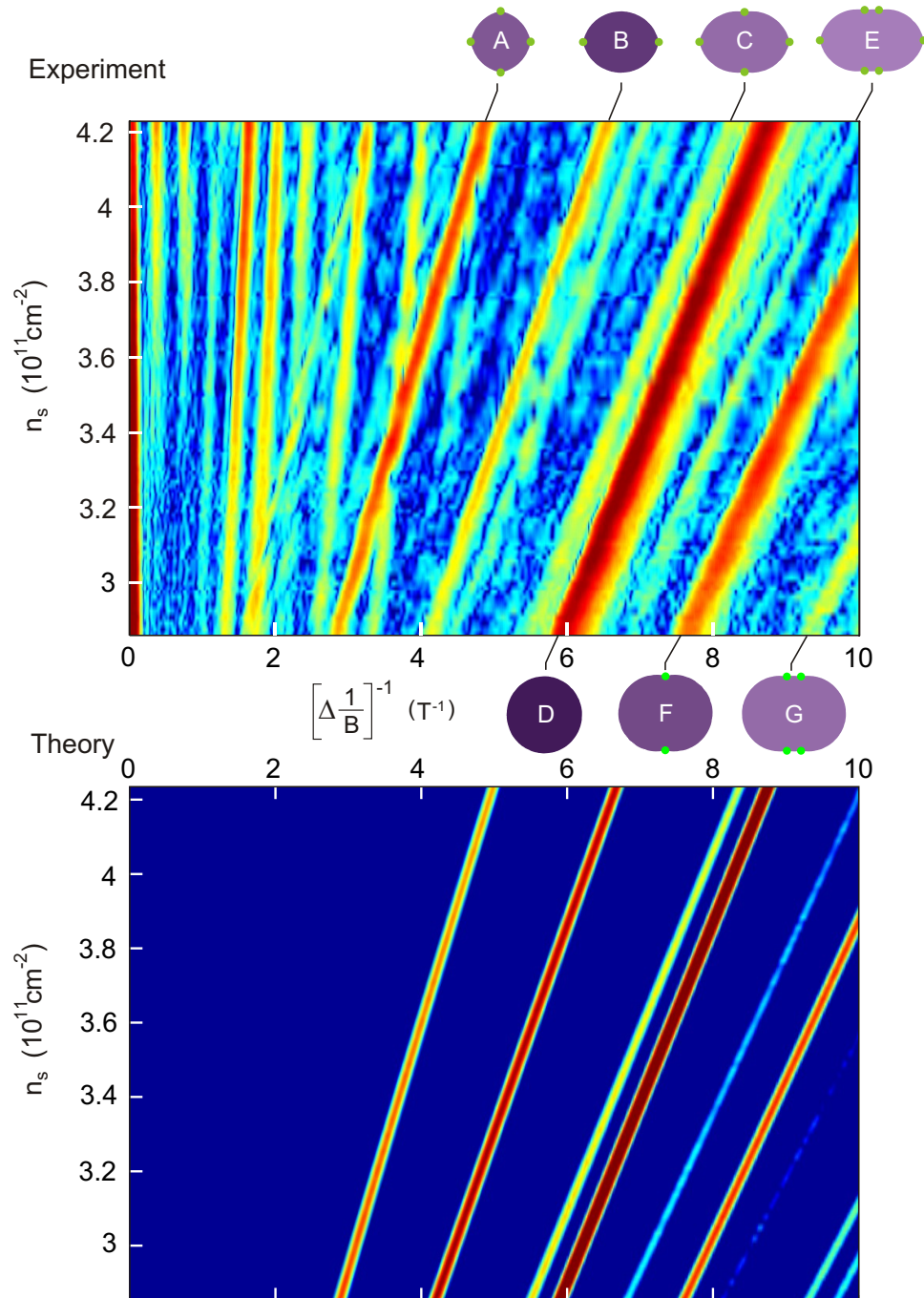
Figure 6.6:

Top: The Fourier transformation of magnetotransport data at 93 different values of the electron density and a temperature of $T \approx 50\,\text{mK}$. Red color signals a large Fourier transform amplitude. The color axis is logarithmic. Peaks are labeled with their electron trajectories in k-space. Bottom: The corresponding result of the simulation for closed electron trajectories.

6.3.3   Comparison with the experiment

The experiment

To get more information about each oscillation in ρ_{xx}, we can use an additional parameter in experiment: the electron density. As the unperturbed Shubnikov-de Haas circle radius k_F increases with increasing electron density n_s, all the intersections of different circles will shift and the areas of closed orbits will change in a characteristic way. This will cause a shift in the observed oscillation period $\Delta(1/B)$ with n_s.

To observe this shift over a range of electron densities, the automated illumination procedure presented in section 4.3.2 is mandatory. It enables to collect magnetotransport data for a large set of densities. Fig. 6.6 consists of 93 measurements of ρ_{xx}, Fourier transformed and stacked vertically. The logarithm of the Fourier transform amplitude is plotted and color coded. Red corresponds to a large amplitude, blue to a vanishing amplitude.

Several maxima are visible. The position $\Delta(1/B)_j$ of each maximum corresponds to an area A_j enclosed by orbit type j in k-space. The largest oscillation amplitude is produced by the Shubnikov-de Haas oscillations as expected for unmodulated samples. The associated circular orbit (D) is plotted at the bottom of the experimental color plot in Fig. 6.6. These are the only oscillations with a periodicity which shifts linearly with n_s, since $A_{SdH} = \pi k_F^2 = 2\pi^2 n_s$. The shift of the other peaks is not linear, but a complicated function of k_F and the period a. In general however, the range of n_s is too small to clearly observe the curvature. Trajectory (B) indicated on top of Fig. 6.6 for instance is a lens shaped orbit. It is also found in 1D modulated systems. Its area is $A_L(k_F, a) = 2k_F^2(\arccos(\eta) - \eta\sqrt{1-\eta^2})$ with $\eta = \pi/(ak_F)$ [64].

Although the two leftmost orbits (A,B) in the upper row were already predicted by Langbein [17] and identified in magnetotransport experiments of modulated samples by Albrecht [8] and Deutschmann [14], the remaining orbits (except for the circular Shubnikov-de Haas orbit (D)) are by no means easily spotted. To identify them, the here introduced Monte Carlo simulation has proven to be indispensable.

---

[1] When using floating point variables for intersection coordinates, areas, and intersection angles, the rounding errors will accumulate and prohibit the creation of correct statistics. Hence, all important variables are represented in an exact way, without rounding errors: two packages LEDA and CGAL are used which represent coordinates with square roots, which occur for intersections of circles. The geometry package CGAL was extended for the here necessary cyclic boundary condition. See appendix F.

The simulation

We can now turn to the parameters (B, V_0 and $V_{\mathbf{q}}$) needed to calculate the probabilities $P_{\mathbf{q}}$:

To find a suitable V_0, it is important to note that the Fourier transform on the experimental data uses a magnetic field range from 0.04 T to 1.1 T. Thus we have to average each probability $P_{\text{total}}(k_{\text{F}}, K_a, V_0^2/B)$ for the orbits found over the same range of magnetic fields. This averaging, however, only changes the relative probabilities of the orbits. The $1/B$-oscillation frequency, which is given by the orbits' area, stays the same. Due to the averaging, the importance of the exact knowledge of the potential modulation amplitude is reduced. Nevertheless, Fig. 6.7 is reproduced here to exemplify the changes in the probabilities of different quantum interferences if V_0^2/B is varied. Due to the large B-field range over which we have to average, the dominant interferences visible mainly for low and high V_0^2/B in Fig. 6.7 are both entering the final Fig. 6.10. This is the case also in experiment, where certain oscillations are dominant only in certain magnetic field intervals.

For the simulation presented in Fig. 6.6 and Fig. 6.10, a value of V_0 as large as 8 meV had to be used to resolve the two leftmost orbits in Fig. 6.7 as in the experimental panel. This V_0 is an order of magnitude larger than the value obtained from the positive magnetoresistance in chapter 5. A reason for this discrepancy may be the already discussed unreliability of the positive magnetoresistance to evaluate the modulation amplitude for 2D modulated systems. The magnetic field range used in the Fourier transform translates into the V_0^2/B-range of 16 meV^2/T to 0.58 meV^2/T.

To describe the shape of the modulation potential, we assume $V_{K_a\cdot(\pm 1,0)} = V_{K_a\cdot(0,\pm 1)} = V_0 \cdot 0.3$ for the main Fourier components and $V_{K_a\cdot(\pm 1,\pm 1)} = V_0 \cdot 0.005$ for the first diagonal components. This proved sufficient to explain the main oscillatory features observed in experiment. The diagonal Fourier components turn out to be essential to explain the features at low $[\Delta(1/B)]^{-1}$ as discussed in section 6.4.3.

With these parameters, the bottom color plot in Fig. 6.6 is produced by running the simulation for 100 evenly spaced n_{s} values. Each orbit found contributes a Gaussian of width $\sigma_{\text{Gauss}} = 1/30$ T centered at the orbit's oscillation frequency $[\Delta(1/B)]^{-1}$. The height of the Gaussian is equal to the averaged probability of the orbit. This procedure is chosen to enable the effortless comparison of the experimental and theoretical plots. The closed trajectories found in the simulation label the various peaks visible both in the experimental and theoretical panel. For instance the unperturbed Fermi circle corresponding to the
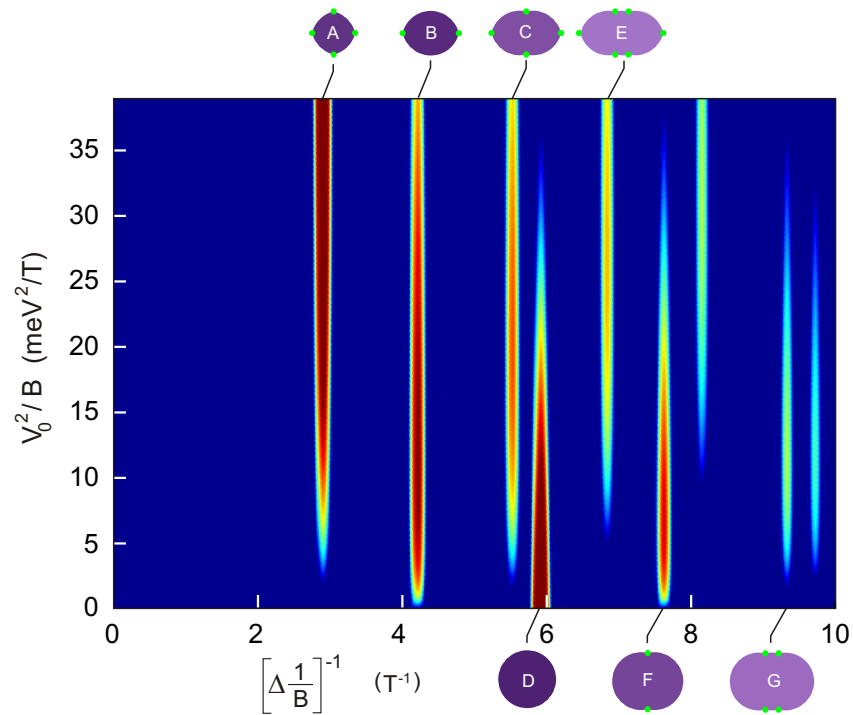
Figure 6.7:
Probability plot for the orbits of Fig. 6.6 versus potential modulation strength V_0^2/B as it enters the tunneling probability $P_{\text{total}}(k_{\text{F}}, K_a, V_0^2/B)$. The calculation uses a density of $n_{\text{s}} = 2.85 \cdot 10^{11}\text{cm}^{-2}$, so the closed trajectories have a different shape and size compared to Fig. 6.6. Red color denotes a large probability. The color axis is logarithmic.

Shubnikov-de Haas oscillations stands out as the most probable closed trajectory both in experiment and simulation.

As apparent from the experimental plot, the oscillations can roughly be classified into two groups: One group with a very weak dependence on n_s and one group with a stronger density dependence. In the theory plot in Fig. 6.6, only those oscillations belonging to the second category appear. Their Fourier maxima on the right hand side of the top panel in Fig. 6.6 can be mapped exactly to their counterpart in the theory plot below. Note that contrary to the orbit probability $P_{total}(k_F, K_a, V_0^2/B)$, the shift of the frequency $[\Delta(1/B)]^{-1}$ is controlled only by k_F and a. It does not depend on a certain choice of B, V_0 or $V_{\mathbf{q}}$. The majority of these orbits have not been observed and explained before. At higher $[\Delta(1/B)]^{-1}$-values even more oscillations are found in experiment. They agree well with the orbits found in the simulation. An example is orbit G. We restrict however the discussion here to a range where the two groups of oscillations with different n_s-dependence are easily distinguishable. To explain the second group of oscillations with a weak dependence on n_s on the left hand side of the top panel of Fig. 6.6, we need to take into account the possibility of quantum mechanical interference of two electron paths in the system. By doing this we get a step closer to the full network model suggested by Pippard for 2D modulated systems [72].

6.4 Quantum interferences of two paths

The slow resistance oscillations (small $[\Delta(1/B)]^{-1}$ frequency) corresponding to the maxima on the left hand side of the upper panel in Fig. 6.6 do not arise from the quantization of a closed orbit. They have no counterpart in the de Haas-van Alphen effect. Instead, they are analogous to an Aharonov-Bohm interferometer in k-space, where the electron wave has two alternative paths between two points. This type of interference was studied for magnetoresistance oscillations in magnesium by Stark and Friedberg [10, 102–105]. Here we need to extend their approach: In contrast to Stark and Friedberg's interference, where no intermediate tunneling is necessary, our interferometers incorporate many tunneling events on each arm.

We consider the two simplified electron paths in Fig. 6.8 which constitute the quantum interference (a) in Figs. 6.10 and 6.11. Each blue dot represents a gap. These gaps are omitted for clarity in Fig. 6.8. We focus on electrons which tunnel over all these gaps via magnetic breakthrough. In a finite magnetic field B, some of these electrons, which start at position 1, may tunnel over one of the gaps $\mathbf{q}_1$ or $\mathbf{q}_2$ and exit at $4'$. To determine the
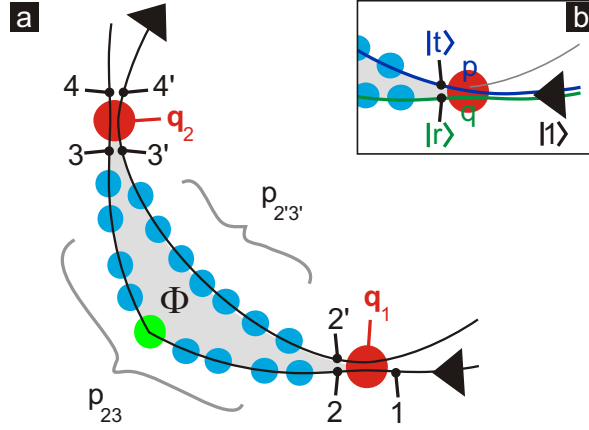
Figure 6.8:
(a) Two path quantum interference in k-space. The paths are simplified, gaps at the blue tunneling points are not shown. At the green point, the electron stays on the Fermi contour and does not need to tunnel. The red points mark the start and end of the interference. This figure is based on quantum interference a in Figs. 6.10 and 6.11. (b) The inset sketches the trajectory a tunneling electron (upper, blue) and a reflected electron (lower, green) takes. They are labeled by the transmitted $|t\rangle$ and reflected $|r\rangle$ wave function.

probability $|\langle 4'|1\rangle|^2$ of this transition, we need the magnetic breakthrough probabilities at each gap. For the example in Fig. 6.8, the probabilities at the red dots are the same and can be written as

$$|\langle 2'|1\rangle|^2 = |p|^2 = P_{\mathbf{q}_1}(k_F, K_a, V_0^2/B) , \tag{6.4}$$

$$|\langle 2|1\rangle|^2 = |q|^2 = 1 - |p|^2 = 1 - P_{\mathbf{q}_1}(k_F, K_a, V_0^2/B) , \tag{6.5}$$

$$|\langle 4'|3\rangle|^2 = P_{\mathbf{q}_2}(k_F, K_a, V_0^2/B) = |p|^2 = |\langle 2'|1\rangle|^2 \quad \text{and} \tag{6.6}$$

$$|\langle 4'|3'\rangle|^2 = 1 - P_{\mathbf{q}_2}(k_F, K_a, V_0^2/B) = |q|^2 = |\langle 2|1\rangle|^2 . \tag{6.7}$$

We introduced here the probability densities p and $q \in \mathbb{C}$. The transmitted, $|t\rangle = |p|e^{i\varphi_t}$, and reflected wave function, $|r\rangle = |q|e^{i\varphi_r}$, at a junction must be orthogonal (cf. Fig. 6.8b). We use this information about their relative phase,

$$\varphi_t - \varphi_r = \left(n + \frac{1}{2}\right)\pi , \tag{6.8}$$

to choose these phases to be $\varphi_t = 0$ and $\varphi_r = \pi/2$. We collect the remaining blue and green dots and the associated transition probabilities in the symbols p_{23} and $p_{2'3'}$. Using

Eqn. 6.3, they are

$$|\langle 3|2\rangle|^2 = |p_{23}|^2 = \prod_2^3 P_{\mathbf{q}}^{n_{\mathbf{q}}^{\text{tunnel}}} Q_{\mathbf{q}}^{n_{\mathbf{q}}^{\text{non}-\text{tunnel}}} \quad \text{and} \tag{6.9}$$

$$|\langle 3'|2'\rangle|^2 = |p_{2'3'}|^2 = \prod_{2'}^{3'} P_{\mathbf{q}}^{n_{\mathbf{q}}^{\text{tunnel}}} Q_{\mathbf{q}}^{n_{\mathbf{q}}^{\text{non}-\text{tunnel}}} \quad . \tag{6.10}$$

The phase change along the transition from 2 to 3 and 2' to 3' consists of two parts: A magnetic field independent phase contribution from the tunnel and reflection events, η_{23} and $\eta_{2'3'}$. A phase contribution φ_{23} and $\varphi_{2'3'}$ due to the vector potential $\mathbf{A}$, given by

$$\varphi_{23} = \frac{e}{\hbar} \int_2^3 \mathbf{A} \cdot d\mathbf{r} \,. \tag{6.11}$$

To reach 4', the electron must tunnel either at junction $\mathbf{q}_1$ or at $\mathbf{q}_2$. The probability $|\langle 4'|1\rangle|^2$ is given by the coherent superposition of both paths,

$$
\begin{aligned}
|\langle 4'|1\rangle|^2 &= |q p_{23} p + p p_{2'3'} q|^2 \\
&= Q P_{23} P + P P_{2'3'} Q + p p^* q q^* p_{23} p_{2'3'}^* + p^* p q^* q p_{23}^* p_{2'3'} \\
&= I_0 + PQ|p_{23}||p_{2'3'}| \left(e^{i(\varphi_{23}+\eta_{23}-\varphi_{2'3'}-\eta_{2'3'})} + e^{i(-\varphi_{23}-\eta_{23}+\varphi_{2'3'}+\eta_{2'3'})} \right) \\
&= I_0 + 2PQ\sqrt{P_{23}P'_{2'3'}} \cos(\varphi_{23} - \varphi_{2'3'} + \eta_{23} - \eta_{2'3'}) \\
&= I_0 + I_1 \cos(\Delta\varphi + \Delta\eta) \,.
\end{aligned}
\tag{6.12}
$$

Here, we introduced the shorthands $I_0 = Q P_{23} P + P P_{2'3'} Q$ and $I_1 = 2PQ\sqrt{P_{23}P'_{2'3'}}$. The last term in Eqn. 6.12 causes an oscillation of the probability $|\langle 4'|1\rangle|^2$ with the phase difference, $\Delta\varphi$, the electron acquires due to the vector potential. This probability determines which path the electron takes after the interference. Thus the trajectory the electron follows after the quantum interference will oscillate with the phase difference $\Delta\varphi$. This oscillation may in turn be visible in a magnetotransport experiment. The phase difference,

$$\Delta\varphi = \frac{e}{\hbar} \int_C \mathbf{A} \cdot d\mathbf{r} = \frac{\hbar}{eB} \cdot A_{\text{QI}} = 2\pi \frac{\Phi}{\Phi_0} \,, \tag{6.13}$$

is proportional to the flux $\Phi = B \cdot A$ enclosed by the two paths (C is the closed integration path $2 \to 3 \to 3' \to 2'$). This leads to *B*-periodic magnetotransport oscillations in the Aharonov-Bohm effect [52,106], where the real space area *A* is fixed. In the system studied here, however, the *k*-space area A_{QI} is constant and the real space area *A* changes with

the magnetic field. Therefore, the phase difference is proportional to $1/B$ (cf. Eqn. 6.13). The resulting $1/B$-oscillations in magnetotransport have the same periodicity as an oscillation due to a hypothetical closed orbit with the same size $A_F = A_{QI}$. The paths of Fig. 6.8 are however not suitable as closed orbit, since they have the same chirality.

We only mention here that oscillations due to the quantum interference are expected whenever I_1 is nonzero. For very small ($B \to 0$) or very large magnetic fields ($B \to \infty$), either P or $Q = 1 - P$ is zero and consequently I_1 and even $|\langle 4'|1\rangle|^2$ vanishes. For both limits, no electrons are expected to reach 4'.

6.4.1   Probability amplitudes

The probability for the electron to "switch paths", $|\langle 4'|1\rangle|^2$, is oscillating with the phase difference $\Delta\varphi$. The oscillations' amplitude given by Eqn. 6.12 is $I_1 = 2\sqrt{QP_{23}P \cdot PP_{2'3'}Q}$. Here we already grouped the probabilities for the two paths. Each (blue) tunnel event thus enters the amplitude via $\sqrt{P_{23}} = |\langle 3|2\rangle|$ with $\sqrt{P_\mathbf{q}}$, each (green) non-tunnel event with $\sqrt{Q_\mathbf{q}}$ and each of the two (red) interference junctions with $\sqrt{PQ}$ (cf. Fig. 6.8). This is true also for other quantum interferences. Since there are combinationally many possible combinations of two paths to form a quantum interference, the most probable path pairs will be found using a variant of the already introduced random walk approach.

6.4.2   The second Monte Carlo simulation

We now present a second simulation to search for the most probable quantum interferences. Analogous to subsection 6.3.2, probable quantum interference paths are found by using random walks through the extended zone scheme. This second simulation runs as described for the first one, only the probabilities are modified to agree with Eqn. 6.12.

Examples of interferences are shown in Fig. 6.9a and b. There, tunnel events are marked with small blue dots. A big green dot marks gap locations where the electron is not tunneling and thus stays on the same Fermi contour. Quantum interferences are marked with big red dots. Interfering paths are drawn in light blue and magenta. As before, the starting trail still need to be cut off. Then, the probability and enclosed area is calculated. These values are stored and a statistic is kept for all these pairs of paths This information yields the theoretical data in Fig. 6.10.
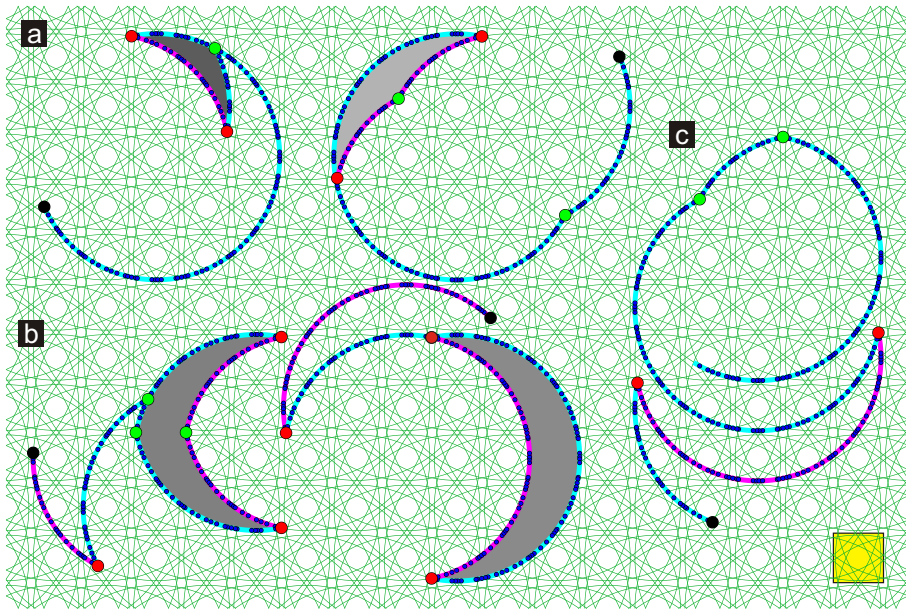
Figure 6.9:
a,b) Possible outcomes of a simulated electron walk through the reciprocal lattice. The starting points are black dots. c) An example for an electron trajectory which did not close before reaching the threshold length. The Brillouin zone is filled in with yellow.

The open trajectory c in Fig. 6.9 is an example of a random walk which does not close after a length of 2.1 circumferences of the Shubnikov-de Haas circle. It does not enter the statistics of probable quantum interferences. In the simulation for Fig. 6.10 the cutoff is set at 10.1.

6.4.3   Comparison with the experiment

As already noted, the maxima on the left hand side of the upper panel of Fig. 6.10 can not be explained by closed electron trajectories. Both the frequency $[\Delta(1/B)]^{-1}$ and the n_s-dependence has no counterpart in the set of closed orbits found in the first simulation.

We will compare these maxima now with the result from the second simulation. For the lower panel of Fig. 6.10 the simulation was run for the same 100 n_s values as in Fig. 6.6. The resulting probabilities were averaged over the same B-field range as before, then represented by Gaussians. The outcome of this second simulation reproduces the unexplained features in the experimental panel nicely. For a large set of peaks the corresponding quantum interferences are indicated above and below the experimental panel of Fig. 6.10.

The interference marked e is already known from 1D modulated systems [14]. The enclosed area has a shape of a lens since it results from the interference of two Shubnikov-de Haas orbits which are spaced a distance K_a apart. In the limit of large k_F it corresponds to the commensurability oscillations of a modulated system [14]. The remaining quantum interferences (a-d,f-m) have however not been observed and explained before. All but the two rightmost interferences in the lower row (e,i) can only be observed in 2D modulated systems.

Now the weak n_s-dependence of most of these interferences can be understood as follows: With increasing k_F the Shubnikov-de Haas circles constituting the "outer" (convex) and "inner" (concave) path of the interference grow. The growth of the outer path enlarges the enclosed area, while the growth of the inner one reduces it. The total enclosed area will not change dramatically in size and merely shift its position. As a consequence, the oscillation frequency has a weak dependence on n_s or E_F and thus temperature broadening is not very effective [72].

Of the novel interferences, those with the smallest area in k-space (a,b,c) are peculiar in that their area is close to the area of one, two and three Brillouin zones. The areas can all be found as the intersections of three Shubnikov-de Haas circles spaced K_a apart,
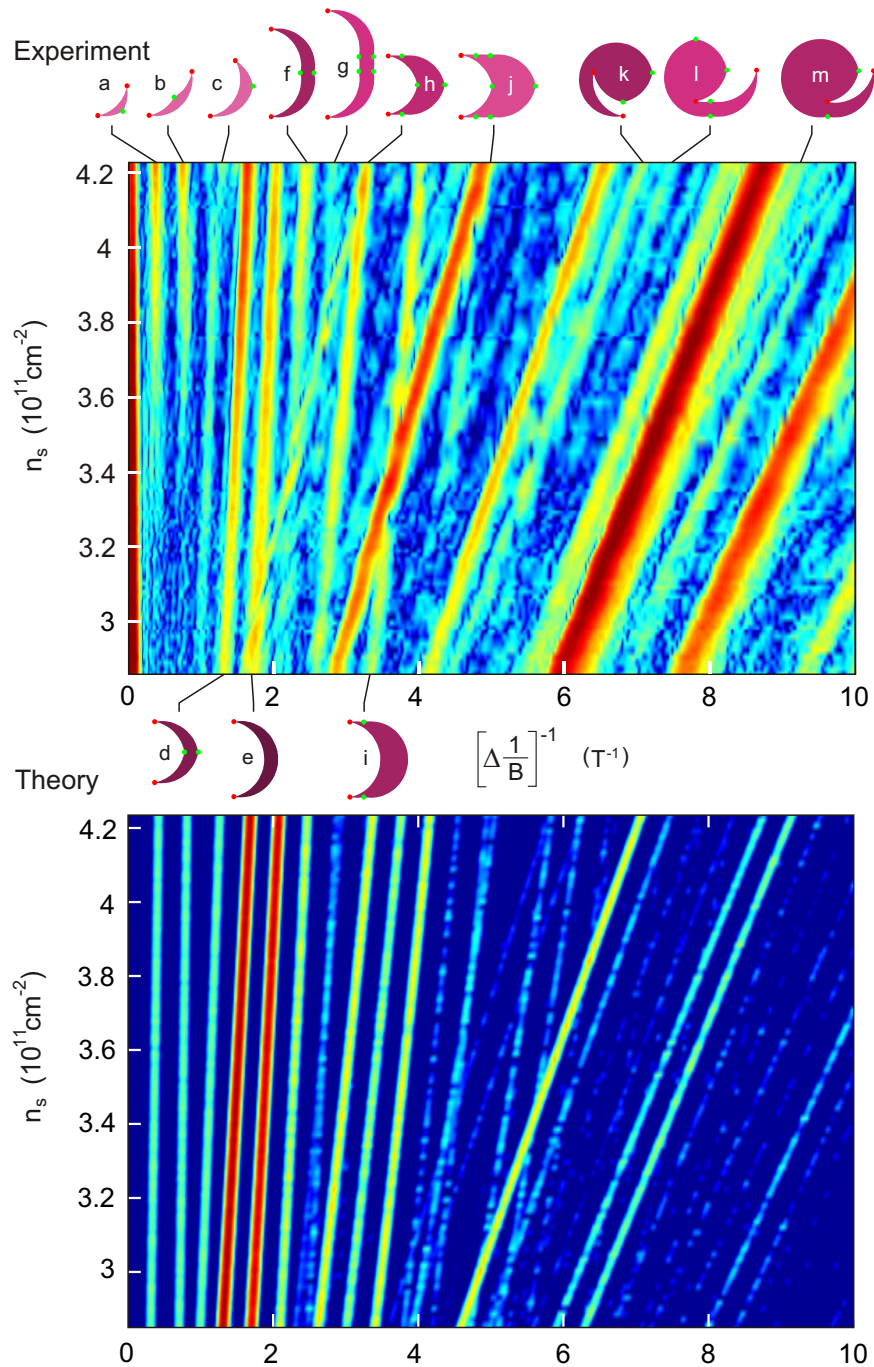
Figure 6.10:

Top: The Fourier transformation of magnetotransport data at 93 different electron densities and at a temperature of $T \approx 50$ mK. This is the same data as in the top panel of Fig. 6.6. Red color signals a large Fourier transform amplitude. The color axis is logarithmic. Peaks are labeled with the interfering paths given by the simulation. Bottom: The corresponding result of the simulation for quantum interferences.

as shown in Fig. 6.11. These areas are however only incidentally comparable to the Brillouin zone, since they can both shrink and grow for densities smaller and larger than the range available to experiment.

The two leftmost interferences (a,b) are only visible for high densities $n_s > 3.4 \cdot 10^{15} \text{cm}^{-2}$ in experiment. This might be a consequence of the increase in mobility for higher densities, since the probability does not increase as dramatically in the simulation. The mean free path changes for instance from 10μm to 35μm for the range of densities in Fig. 6.10. The two interferences are most sensitive to the mobility as they are the largest in real space. Their circumferences are 0.32 μm$/(B/\text{T})$ and 0.37 μm$/(B/\text{T})$ respectively. For small magnetic fields of 0.03 T the circumferences are larger than the mean free path of 10μm at low electron densities.

Finally, a detailed comparison of experiment and theory reveals unexplained oscillations in the experiment. An oscillation is found, whose frequency $[\Delta(1/B)]^{-1}$ shifts from 1.5 T to 3 T (as marked with arrows in Fig. 6.12), which is not present in both Monte Carlo simulations as demonstrated in Fig. 6.12. This oscillation is also remarkably different from all the rest: It is not continuous, but broken up into sections. At present, we have no explanation for this oscillation.

We conclude this section with an overlay of the experimental and combined theoretical color plots in Fig. 6.13. In this overlay both the position and the probability of the observed oscillations agrees well with the combined results from the two Monte Carlo simulations. The small mismatch may be due to the accuracy with which the electron density can be extracted from experiment. When shifting the experimental color plot by $\Delta n_s \approx 0.03 \cdot 10^{11} \text{ cm}^{-2}$ to lower densities, this mismatch disappears.

Fourier components of the modulation potential

We already hinted at evidence for the presence of higher Fourier components in the modulation potential. Up to now no direct access to the relative strength of different Fourier components is available in experiment. Only the case that the diagonal Fourier components $V_{K_a \cdot (\pm 1, \pm 1)}$ are larger than the first Fourier components $V_{K_a \cdot (\pm 1, 0)}$, $V_{K_a \cdot (0, \pm 1)}$ can be detected: The lattice effectively turns $\pi/2$ and changes its period, so a different frequency of the commensurability oscillations can be observed [84].

Here we can detect higher order Fourier components even if their amplitude is only a fraction of the main Fourier component. In Fig. 6.10 the diagonal Fourier component used
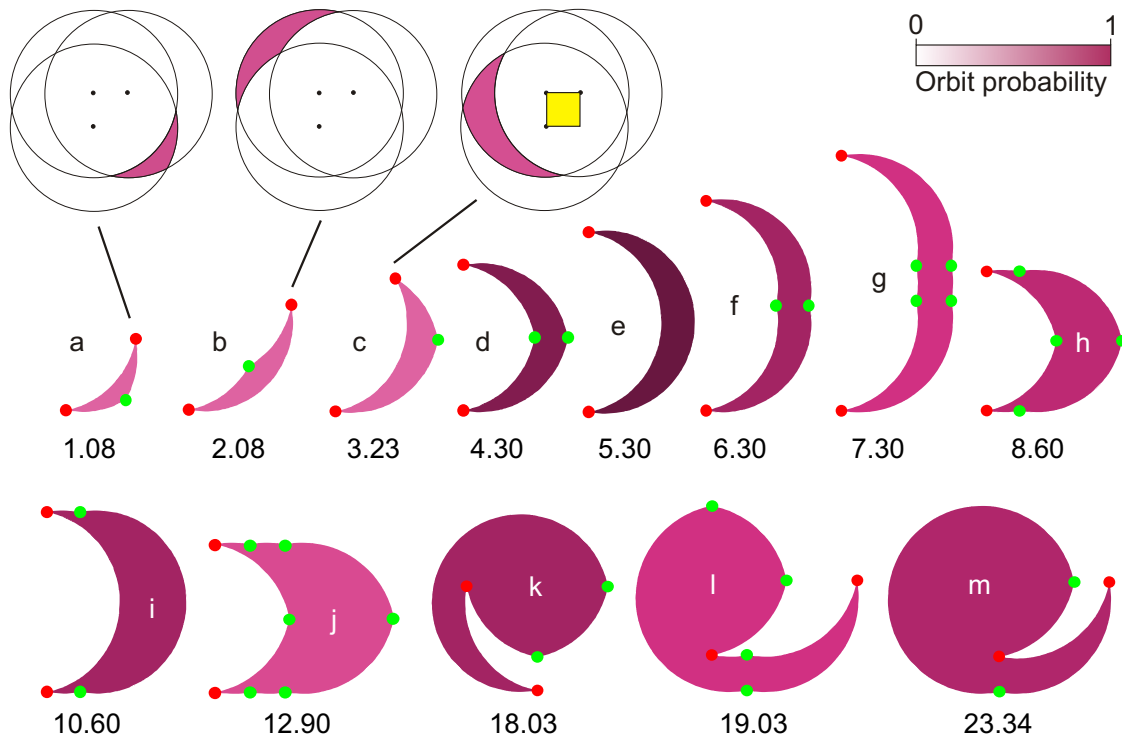
Figure 6.11:
The quantum interferences shown in Fig. 6.10. Green dots mark gaps where electrons do not tunnel. Red dots mark start and end points of the two interfering electron trajectories. Gaps where electrons tunnel are not marked, since they are too frequent. A darker fill color indicates a higher probability. The shapes shown here are for a density of $n_s = 4.24 \cdot 10^{11}\text{cm}^{-2}$. The enclosed area is given in units of the first Brillouin zone area. The Shubnikov-de Haas circles at the top visualize how the area of the first three interferences come about in k-space. The first Brillouin zone is filled with yellow.
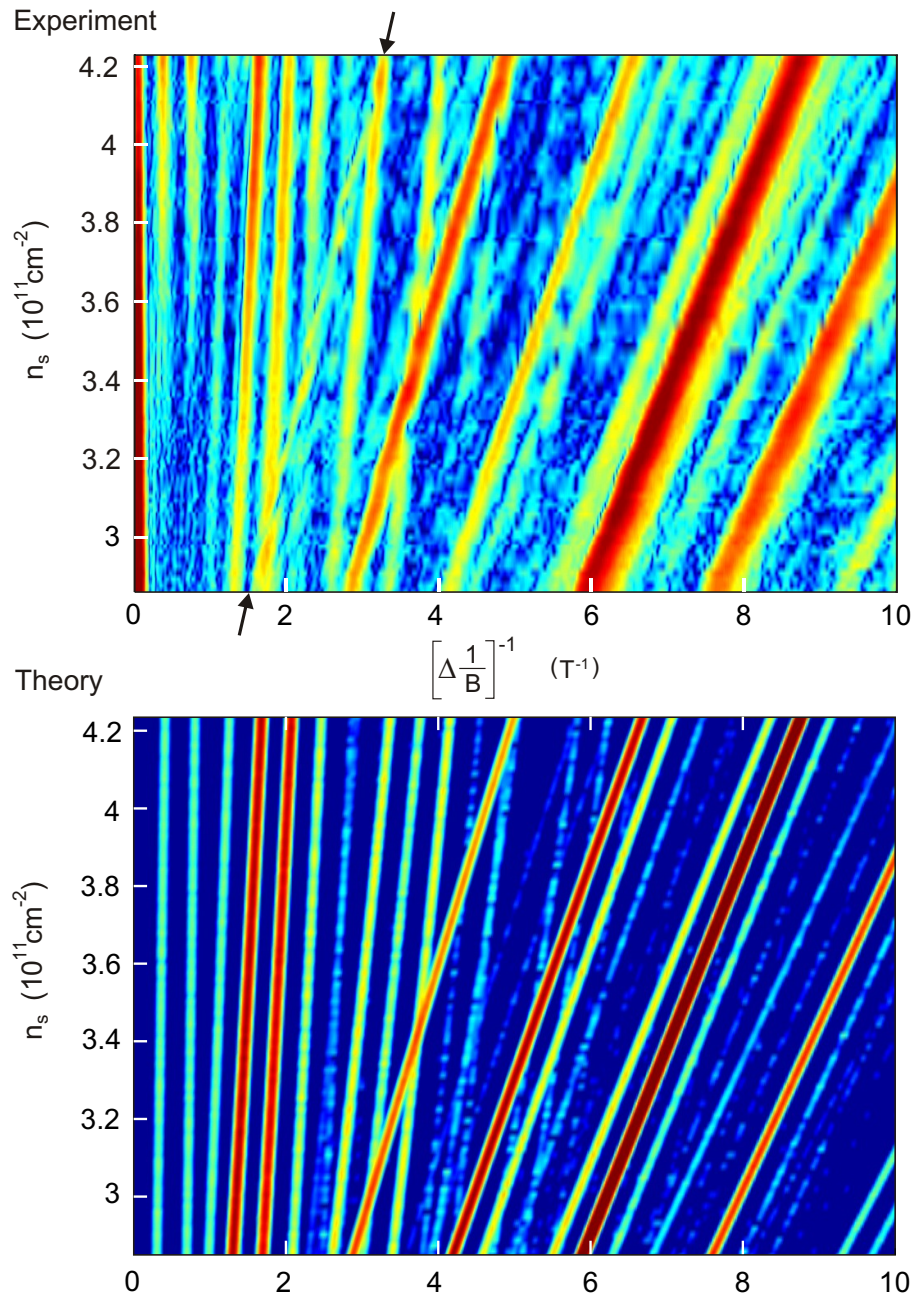
Figure 6.12:
Top: The Fourier transformation of the magnetotransport data in $1/B$ for a range of electron densities, as for Fig. 6.10. The unexplained oscillations are marked with arrows. Bottom: The simulation results depicted in Fig. 6.10 and Fig. 6.6 combined in one colorplot. The aforementioned oscillations are not reproduced.
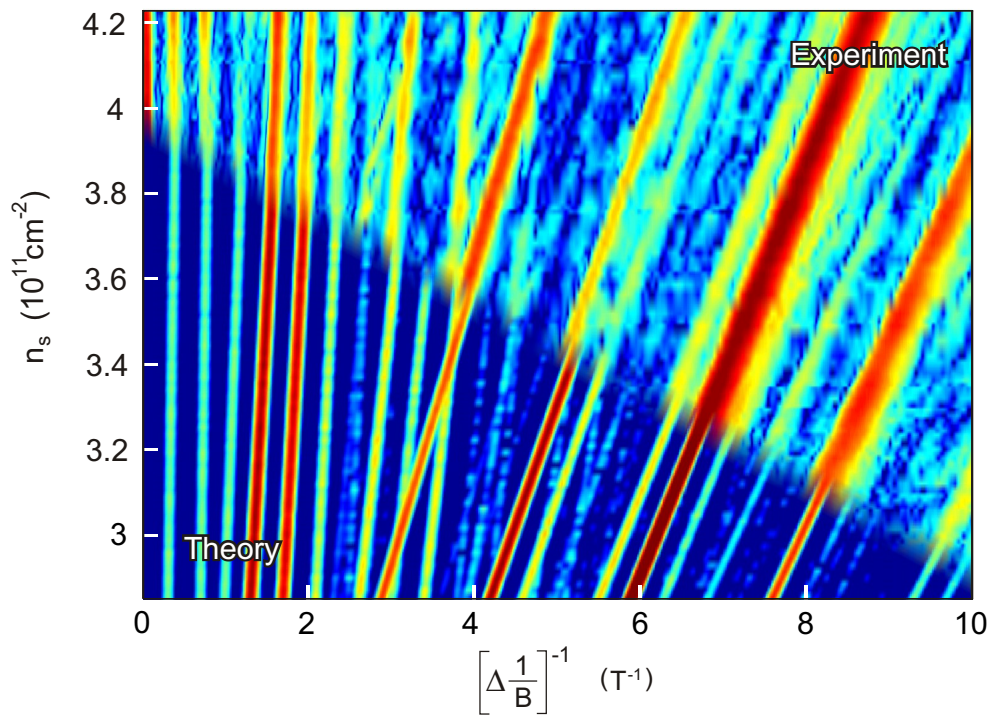
Figure 6.13:

Overlay of the experimental and theoretical color plots presented in Fig. 6.12. The small mismatch is due to the inevitable inaccuracy in the determination of the electron density from the experimental data.
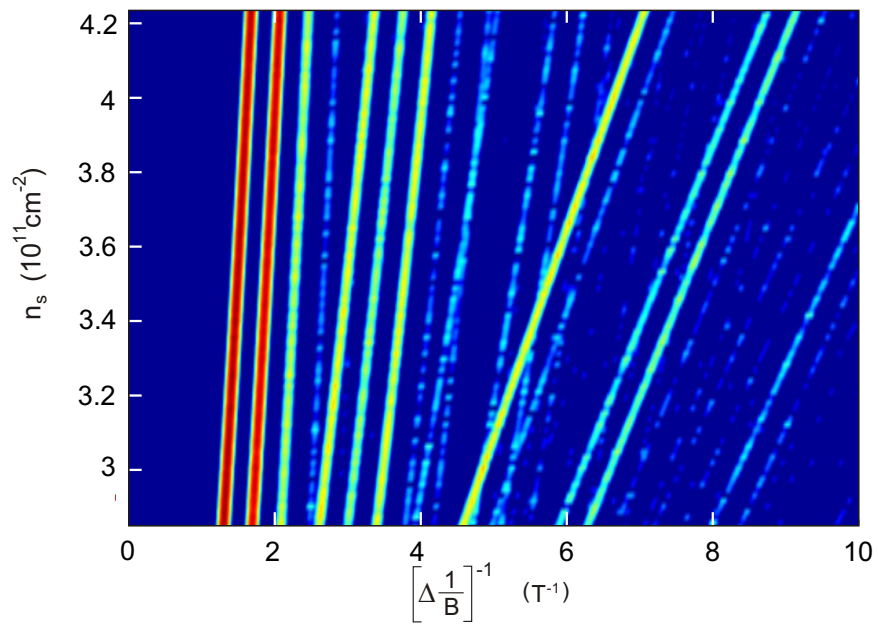
Figure 6.14:
A simulation of quantum interferences for a pure cosine potential. Less interferences than in Fig. 6.10 are visible. Red color denotes a large probability. The color axis is logarithmic.

was $V_{K_a \cdot (\pm 1, \pm 1)} = 1/60 \cdot V_{K_a \cdot (\pm 1, 0)}$. When setting $V_{K_a \cdot (\pm 1, \pm 1)}$ to zero, some interference oscillations (a,b,c) seen in experiment disappear from the simulations' output, as illustrated in Fig. 6.14. This can be understood as follows: For $V_{K_a \cdot (\pm 1, \pm 1)} = 0$ all gaps on the second Brillouin zone boundary are closed. These gaps are located where the diagonally displaced Shubnikov-de Haas orbits in Fig. 6.11 intersect. One can see immediately that the two leftmost interferences (labeled a,b in Fig. 6.10) have a no-tunnel point (green) on such an intersection. The third interference (c) has its upper red point, where its two paths meet, on such an intersection. Thus these three interferences enclosing the smallest area in *k*-space are only possible if an electron finds a gap at the second Brillouin zone.

We already know that $V_{K_a \cdot (\pm 1, \pm 1)}$ has to be non-zero. Its value can be estimated using calculations as in Fig. 6.15. Obviously, already small values of $V_{K_a \cdot (\pm 1, \pm 1)}$ are enough to allow for the oscillations (a,b,c) observed in experiment. We chose $V_{K_a \cdot (\pm 1, \pm 1)} = V_0 \cdot 0.005$, since it best reflects the relative probabilities of the three novel oscillations (a,b,c) at low $[\Delta(1/B)]^{-1}$ with the remaining oscillations. For larger $V_{K_a \cdot (\pm 1, \pm 1)}$ these novel oscillations become dominant, which is not true for the experiment.

6.5   Summary

Quantum interferences unique to a 2D artificial crystal have been measured for the first time and are quantitatively accounted for. These studies have become possible due to the unrivaled sample quality and the careful illumination technique used in our magneto-transport measurements.

The electron density dependent study allows the identification of the relevant orbits and groups of interfering paths. We present a Monte Carlo approach which correctly predicts the plethora of new orbits and quantum interferences observed in our experiment.

Using the simulation techniques presented here, closed orbits and interferences can be predicted for different lattice geometries, periods and modulation strengths to tailor future samples.
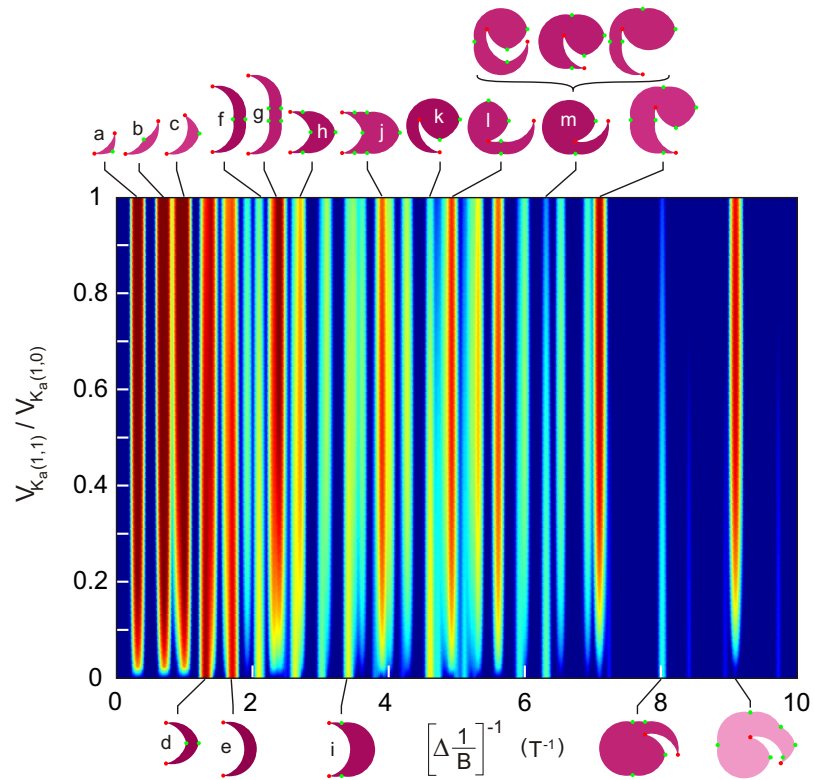
Figure 6.15:
A simulation using different relative Fourier component sizes $V_{K_a \cdot (\pm 1, \pm 1)}/V_{K_a \cdot (\pm 1, 0)}$ for an electron density of $n_s = 2.85 \cdot 10^{11} \mathrm{cm}^{-2}$. V_0^2/B is averaged as in Fig. 6.10. For $V_{K_a \cdot (\pm 1, \pm 1)} = 0$ many interferences vanish. Red color denotes a large probability. The color axis is logarithmic. The interference paths are depicted for the above density, so they have a different shape and size compared to Fig. 6.10. The three interferences at the top of the figure have the same size like the one below and contribute to the oscillation, but are not as probable.

7 Different lattice geometries

Up to now, our discussion focused on modulations with square geometry and 100 nm periodicity. In the present chapter we extend our scope to different periodicities and geometries. The results are divided into two groups:

The first two sections confirm and refine the physics of quantum interferences of chapter 6. In the first section, the periodicity of the square lattice is reduced to 90 nm. This changes the network of Shubnikov-de Haas circles in k-space. At large, the findings of chapter 6 are confirmed for the altered network. Unexpected features arise only near crossings of certain oscillations. These features can be reproduced also for the 100 nm periodicity sample of the preceding chapters. In the second section, the square lattice is replaced by a Lieb lattice [107]. For the Lieb lattice, the Brillouin zone is four times smaller, different Fourier components appear, but the square symmetry of the lattice stays the same. New quantum interferences are observed due to the additional Fourier components.

In the third section we address samples with a rectangular modulation. The recent prediction of a non-monotonous dependence of the commensurability oscillation amplitudes on the applied magnetic field is verified.

7.1   Smaller lattices, higher temperatures

To check the findings of the preceding chapter, where we used a 100 nm periodicity modulation, samples with square modulation and $a = 90$ nm periodicity were produced. For such a sample, the network of Shubnikov-de Haas circles in k-space changes: The distance of two neighboring Shubnikov-de Haas circles, $K_a = 2\pi/a$, gets larger. Thus, the area enclosed by closed orbits (which have a convex circumference) will shrink. Hence,
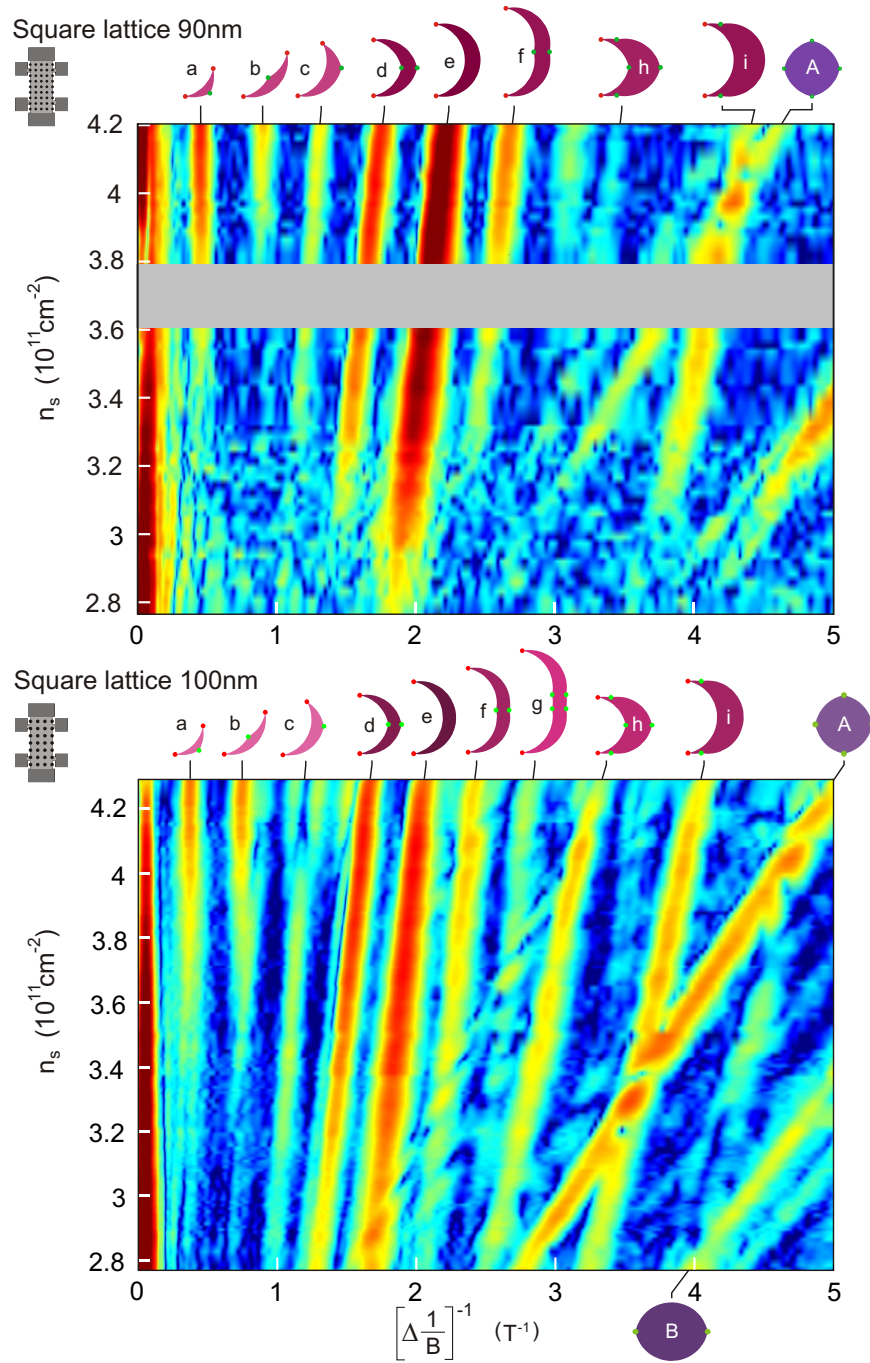
Figure 7.1:
Top: The Fourier transformation of magnetotransport data at 53 different electron densities for a square modulation with 90 nm period. Red color signals a large Fourier transform amplitude. The color axis is logarithmic. In the grey region no data was taken due to limitations in the illumination process. Peaks are labeled with their interfering paths. Bottom: The same for a 100 nm period modulation and 124 different electron densities. Both measurements are done at $T \approx 300$ mK. The lower plot can be compared to Fig. 6.12, which is measured at $T \approx 50$ mK.

the corresponding $1/B$-oscillation frequency in ρ_{xx} should get smaller compared to its counterpart in the 100 nm lattice.

To verify this, the Fourier transformations of 53 ρ_{xx}-traces obtained on a sample with a 90 nm period modulation are plotted in the upper panel of Fig. 7.1. For comparison, the bottom panel shows a plot for a 100 nm period sample. This is the same sample as the one used for the two previous chapters. In contrast to the data in the top panels of Fig. 6.6 and 6.10, which are taken at $T \approx 50$ mK, the measurement temperature for Fig. 7.1 is $T \approx 300$ mK. The quantum interferences (a-i) and orbits (A,B) responsible for the peaks in Fig. 7.1 are obtained with Monte Carlo simulations. The oscillation due to orbit (A) confirms the predicted shift to lower $1/B$-frequencies when comparing its position for the $a = 100$ nm plot with its position for the $a = 90$ nm plot.

With increasing $K_a = 2\pi/a$, the area enclosed by quantum interferences on the other hand grows: the Shubnikov-de Haas circles constituting the "inner" (concave) path of the interference move away from the "outer" (convex) path. The corresponding $1/B$-oscillation frequency increases. Indeed the $1/B$-oscillations (a-i) are shifted to the right in the top panel of Fig. 7.1. Due to this shift, the intersection point of the two $1/B$-oscillations (A) and (i) moves to higher electron densities.

Exactly at this intersection point, an unexpected feature arises: The two experimental plots in Fig. 7.1 are different from the ones in chapter 6 as the $1/B$-oscillations (i) and (B) have about the same amplitude[1]. Right at the crossing of the two oscillations, this amplitude is increased. At slightly higher and lower electron density, the amplitude is nearly completely suppressed. Remnants of this behavior are also present for a different sample of 100 nm period in Fig. 7.4. Since each of the $1/B$-oscillations (A) and (i) are the outcome of a different Monte Carlo simulation, we can not explain the above effect by simply adding the two simulations as done in the previous chapter in Fig. 6.12. Instead, a more complex interplay of the closed orbit and the two-path quantum interference seems to take place. Such behavior is not properly captured by our simulations.

---

[1] The data shown in the bottom panel in Fig. 7.1 was obtained using the same sample as in chapter 6. However, the data was taken during a different cooldown cycle. This temperature cycling may be the reason for a change in stress exerted by the metal gate and hence for a modified ratio of the Fourier components.

7.2   The Lieb lattice
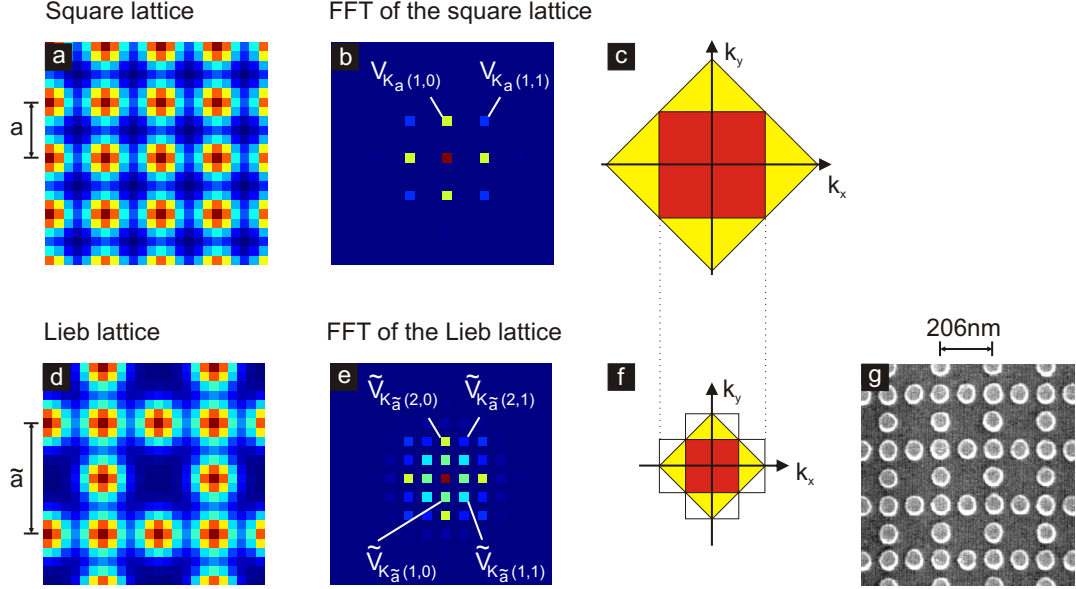
Figure 7.2:
A square (a) and Lieb (d) modulation potential, constructed from Gauss functions. (b,e) Absolute value of the 2D Fourier transformation of the modulation potentials in a) and d). The Fourier components used in the text are marked. (c,f) The first (red) and second (yellow) Brillouin zone corresponding to the first two Fourier components. A size comparison (dotted line) reveals that the first Brillouin zone of c) is as large as the third one of f). (g) A scanning electron microscopy of the Lieb lattice after evaporation and lift-off of a thin metal layer.

For the 90 nm lattice studied in the previous section, the size of the Brillouin zone is slightly increased compared to a 100 nm lattice. The Fourier components however stay essentially the same.

By replacing the square lattice in Fig. 7.2 a) with a Lieb lattice [107] as in Fig. 7.2 d), the superlattice periodicity increases from $a = 103$ nm to $\tilde{a} = 2 \cdot a = 206$ nm. The Lieb lattice has a four times larger unit cell, so the Brillouin zone size is decreased to a quarter of its original size (cf. Fig. 7.2 f). This leads to a much more nested network than before, since each Shubnikov-de Haas circle needs to be shifted into this drastically reduced first Brillouin zone. Additional gaps in this network appear along the new first Brillouin zone boundary, corresponding to new first order Fourier components. We want to point out that the Fourier components of the square lattice, $V_{\mathbf{q}}$, are roughly the same as those for
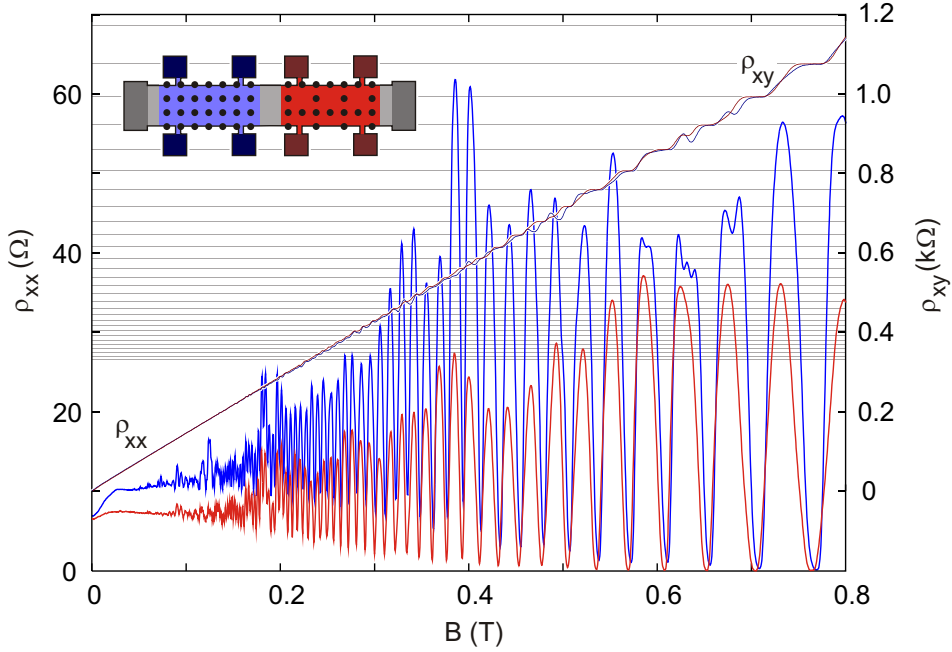
Figure 7.3:

Red: Longitudinal and Hall resistivities for a modulation with Lieb geometry of $\tilde{a} = 206$ nm period. The measurement temperature is $T \approx 300$ mK, the electron density is $n_\mathrm{s} = 4.3 \cdot 10^{11}/\mathrm{cm}^2$ and the mobility is $\mu = 2.2 \cdot 10^6 \mathrm{cm}^2/\mathrm{Vs}$. Blue: The same for a square modulation with $a = 103$ nm period. The data for both plots is measured at the same time using a single Hall bar with two active regions, which are patterned accordingly. The splitting in ρ_{xx} and non-monotonic behavior of ρ_{xy} around $B = 0.62$ T for square lattices is attributed to the Hofstadter butterfly spectrum as in chapter 5.

the Lieb lattice, $\tilde{V}_\mathbf{q}$, for example, $V_{K_a \cdot (1,0)} \approx \tilde{V}_{K_{\tilde{a}} \cdot (2,0)}$. Also the two underlying Bravais lattices have the same symmetry.

For an optimal comparison of the two lattice types, a Lieb lattice and a square lattice were exposed on the two active regions of one and the same Hall bar. Magnetotransport traces for the two lattices, which are measured simultaneously using this single Hall bar, are displayed in Fig. 7.3. The blue measurement for a square modulation exhibits less fine structure around e.g. $B = 0.6$ T as the measurement in Fig. 5.1, which was attributed to the Hofstadter butterfly. This is due to the lower mobility and higher measurement temperature $T \approx 300$ mK in Fig. 7.3. Still, we will use this data, since it allows us to directly compare $1/B$-oscillations for the two lattices, while excluding changes due to a difference in sample quality.

Differences originating from the lattice geometry are already apparent in the envelope of the Shubnikov-de Haas oscillations for the red and blue ρ_{xx}-traces. The density dependent Fourier analysis in Fig. 7.4 reveals particularly drastic differences in the two $1/B$-oscillation patterns. The most prominent oscillations (b, c, f, h, i, A) for the square modulation in the lower panel of Fig. 7.4 are very weak or vanish for the Lieb modulation in the upper panel. Some oscillations, like (B), may get stronger for the Lieb case. Most interesting are the oscillations (α, γ, ε, ζ, η), which are only present for the Lieb modulated sample.

In order to find their corresponding quantum interferences, the Monte Carlo simulation of the second type was carried out for a modulation potential with $V_0 = 8$ meV and Fourier components $\tilde{V}_{K_{\tilde{a}} \cdot (\pm 1, 0)} = \tilde{V}_{K_{\tilde{a}} \cdot (0, \pm 1)} = V_0 \cdot 0.03$, $\tilde{V}_{K_{\tilde{a}} \cdot (\pm 1, \pm 1)} = V_0 \cdot 0.012$, $\tilde{V}_{K_{\tilde{a}} \cdot (\pm 2, 0)} = \tilde{V}_{K_{\tilde{a}} \cdot (0, \pm 2)} = V_0 \cdot 0.3$ and $\tilde{V}_{K_{\tilde{a}} \cdot (\pm 2, 1)} = \tilde{V}_{K_{\tilde{a}} \cdot (1, \pm 2)} = V_0 \cdot 0.0075$, which describe a Lieb lattice modulation potential. The resulting probabilities were averaged over a magnetic field range from 0.04 T to 1.1 T. We chose these parameters as they are similar to the ones used for the square lattice in the previous chapter. In particular, the modulation potential V_0, the magnetic field range and the main Fourier component $\tilde{V}_{K_{\tilde{a}} \cdot (\pm 2, 0)} = V_{K_a \cdot (\pm 1, 0)}$ are identical to the values used in Fig. 6.10.

The result of this simulation for 10 evenly spaced electron densities is plotted on top of the experimental result in Fig. 7.5[2]. As in experiment, the probabilities of the oscillations (b, c, f, g, i) are decreased. Of these oscillations, (f, g, i) are present even for a modulation potential, where only the main Fourier coefficient $V_{K_a \cdot (\pm 1, 0)} = V_{K_a \cdot (0, \pm 1)}$ is non-zero (cf. tables A.2 and A.3). Since this Fourier component is the largest in our simulation, the additional smaller Fourier components, $\tilde{V}_{K_{\tilde{a}} \cdot (\pm 1, 0)}$, $\tilde{V}_{K_{\tilde{a}} \cdot (\pm 1, \pm 1)}$ and $\tilde{V}_{K_{\tilde{a}} \cdot (\pm 2, 1)}$, added to construct the Lieb lattice pattern, must be the reason for the suppression of these oscillations. Oscillation (A) is due to a closed trajectory, so it is not captured by this Monte Carlo simulation. The quantum interferences (d, e) are also found for the square case, while the quantum interference (β) is new. It has approximately the same frequency as (a) for the square case, but the shape is different. Most importantly, the simulation finds quantum interferences for the Lieb lattice, (α, γ, ε, ζ, η), which are absent for the square modulation potential. The quantum interferences (ζ) and (η) are similar to the interferences (d) and (f), only the points where no tunneling takes place lie on the new first Brillouin zone of the Lieb lattice. As a consequence, their shape changes: The area enclosed by (ζ) is larger than (d), the one enclosed by (η) is smaller than (f). Pictorial

---

[2] Only 10 different electron densities are used here, since the computation time for a single n_s-value increases by more than an order of magnitude compared to the square lattice case in Fig. 6.10. This is due to the smaller Brillouin zone for the Lieb lattice, which divides each cyclotron orbit into many more sections.
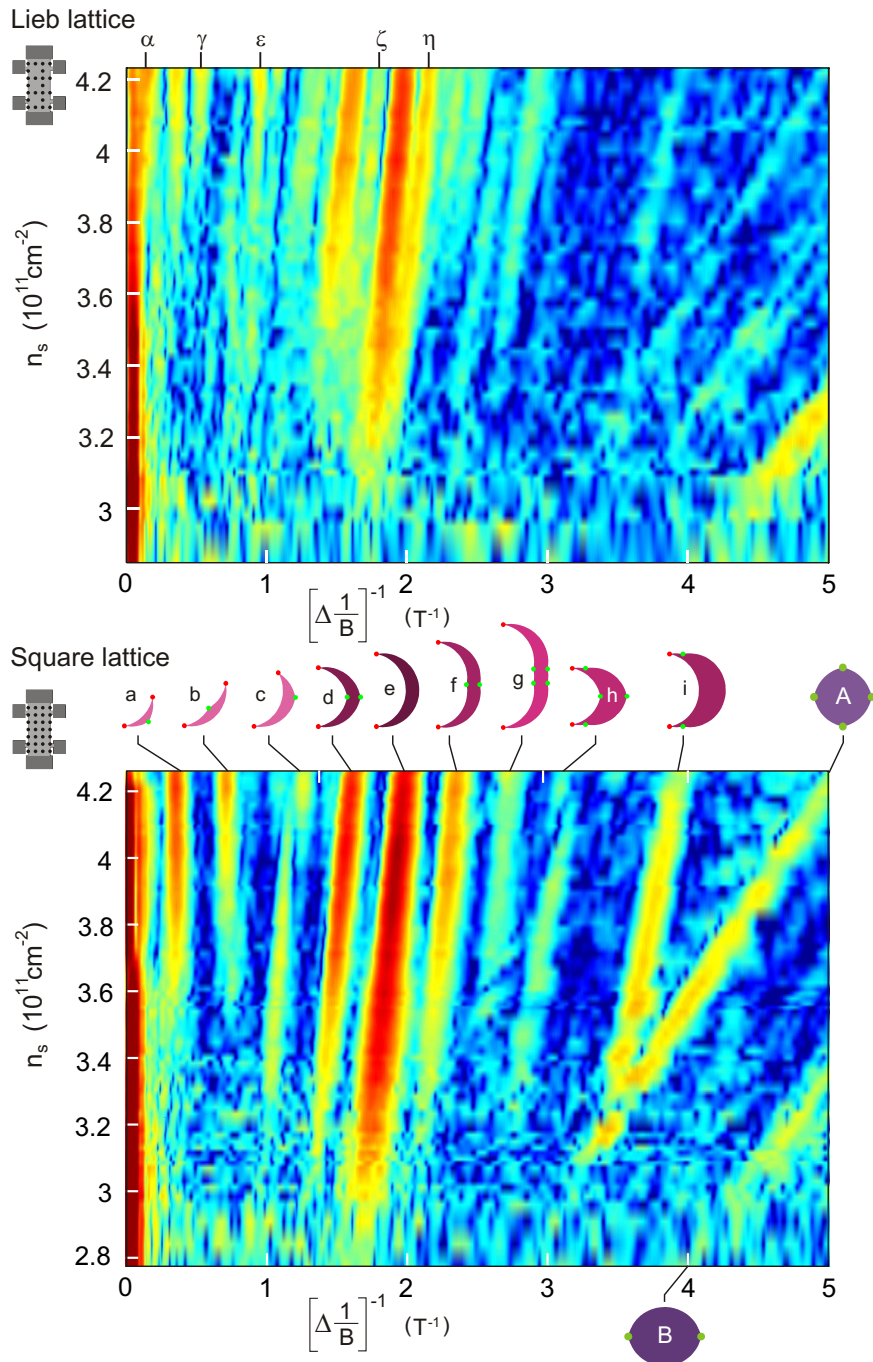
Figure 7.4:

Top: The Fourier transformation of magnetotransport data at 65 different electron densities for a modulation with Lieb geometry of $\tilde{a} = 206$ nm period. The measurement temperature is $T \approx 300$ mK. Red color signals a large Fourier transform amplitude. The color axis is logarithmic. Bottom: The same for a square modulation with $a = 103$ nm period. Prominent oscillations are marked with their orbits or quantum interferences. The data for both plots is measured simultaneously using a Hall bar with two active regions.
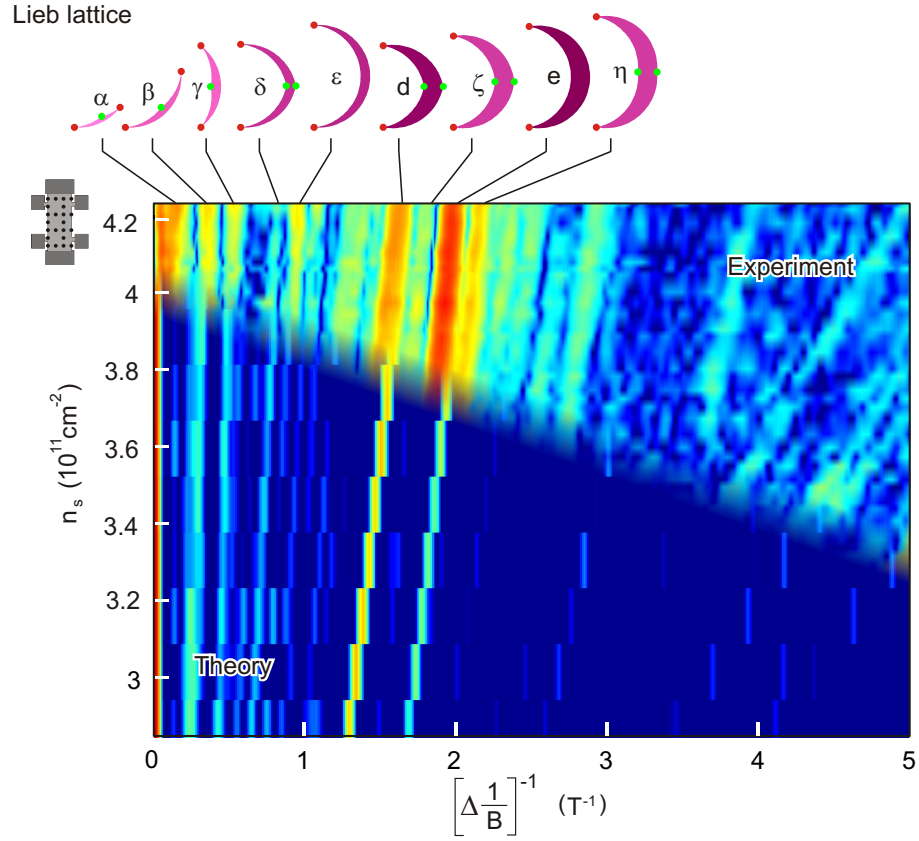
Figure 7.5:

Overlay of the experimental color plot of Fig. 7.4 and a theoretical color plot. The simulation was run for only 10 different densities, so peaks shift in a staircase like fashion. The quantum interference paths are indicated at the top of the plot.

representations of all the quantum interferences mentioned for the Lieb lattice are given in Fig. 7.5.

To summarize, we have found quantum interferences typical for Lieb lattices and we are able to explain them using the same Monte Carlo simulation as for the square lattice. In general, Fourier transformed magnetotransport data as in Fig. 7.5 is like a fingerprint of the modulation potential experienced by the electrons in the 2D system. We can use such data to get detailed information about the relative sizes of the Fourier components and one may even test different models for the shape of the modulation potential.

7.3   The rectangular lattice

In the preceding chapters two quantum mechanical effects typical for 2D electron systems modulated in two spatial directions were observed. Here we address another phenomenon, which is already present for one-dimensional superlattices: the commensurability or "Weiss" oscillations. These oscillations were first also considered to be of quantum mechanical origin, but later they were explained semiclassically. A recent calculation based on this semiclassical approach predicts for rectangularly modulated samples an intriguing non-monotonous dependence of the commensurability oscillation amplitudes on the applied magnetic field. Such a dependence is neither known for one-dimensional nor for square lattices, and has so far neither been confirmed by quantum calculations nor by experiments. This section summarizes our effort to observe these novel features in samples modulated with a rectangular pattern. We are able to demonstrate a good agreement between the theory and our experiments. [3]

7.3.1   Commensurability oscillations for 1D modulation

The commensurability oscillations of the band conductivity were introduced in section 3.1.1. They are a consequence of the modulation induced broadening of the Landau levels. They can, in contrast to the commensurability oscillations of the scattering conductivity, also be understood in semiclassical terms as the result of a guiding center drift of the classical cyclotron orbits of electrons at the Fermi energy [108]. To illustrate this, we revert to the one-dimensional modulation of Eqn. 3.1. First we consider the flat band condition where the band conductivity is zero. For this case the average of the potential $V(x)$ over the perimeter of a cyclotron orbit is the same for all guiding center coordinates x_0 as depicted for two examples in the top panel of Fig. 7.6a. Thus the guiding center will not drift and no additional conductivity $\Delta\sigma_{yy}$ is expected. The opposite is true for the case shown in the bottom panel of Fig. 7.6a, which can be attained by changing the magnetic field and thus the cyclotron orbit radius R_c. For this second case, the guiding center will drift along straight lines in y-direction and yield a contribution $\Delta\sigma_{yy}$. In brief, the contribution $\Delta\sigma_{yy}$ will oscillate when changing the cyclotron orbit radius. This produces oscillations in ρ_{xx}.

The guiding center picture is also valid for two-dimensional modulation potentials. It can be used to explain the suppression of the band conductivity in samples modulated in two

---

[3] This work on rectangular superlattices has been carried out in collaboration with Dr. S. Chowdhury.
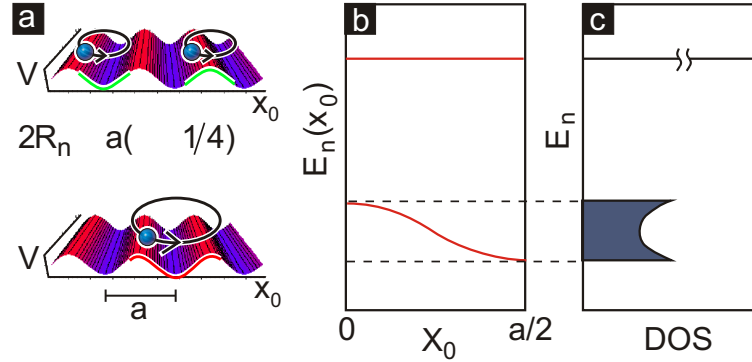
Figure 7.6:
 a) Top panel: The average of the modulation potential with period a over a cyclotron orbit is independent of x_0 if the flat band condition is met. Bottom panel: The average changes with x_0. b) The corresponding dispersion relations. c) The resulting density of states. Van-Hove singularities arise due to the flat dispersion at $x_0 = 0, a/2$.

spatial directions as demonstrated in the next paragraph.

7.3.2   Band conductivity suppression for 2D modulation

The pioneering experiments on 1D modulated samples [11, 12] were soon followed by experiments using a two-dimensional modulation potential. There, the commensurability oscillations were much smaller in amplitude than those observed before in the band conductivity for a 1D modulation (when the resistance is measured along the modulation direction), but they were comparable in amplitude and phase with the scattering conductivity observed in the 1D modulation case (when the current flows perpendicular to the modulation direction) [4]. This apparent suppression of the band conductivity in 2D superlattices was first interpreted quantum mechanically [4, 49]: As elaborated in chapter 5, due to the 2D modulation, Landau levels split into subbands according to the Hofstadter butterfly spectrum. If collision broadening effects are so weak that spectral functions of different subbands have little overlap, the calculated band conductivity is considerably suppressed as compared to that calculated for the corresponding situation with a 1D modulation. This suppression becomes more effective with increasing strength of the 2D modulation and with increasing mobility [4, 49]. This is, of course, a rather subtle argument, since the subband splitting was not observed in the experiments under consideration. This splitting is also not observed in the samples presented in this chapter

due to the relatively low electron mobilities.

Later, the suppression was also explained in the guiding center picture [109]. Initial efforts to describe commensurability effects for 2D modulations were restricted to modulation potentials of the form $V(x,y) = V_x(x) + V_y(y)$ with small amplitudes V_j [110,111]. In this approximation, the modulation effects in x- and y-direction decouple and no suppression of the commensurability oscillations is obtained [112]. A numerical solution of the full Boltzmann equation without such a weak-potential approximation, on the other hand, yielded a drastic suppression of the commensurability oscillations for large modulation amplitude and high mobility [112]. Later Grant *et al.* [84,113] argued that, for a two-dimensional modulation, part of the guiding centers drift along pinned closed orbits and thus should not contribute to the band conductivity. This should cause the suppression of the commensurability oscillations. In subsequent work by Gerhardts and Zwerschke, [109] the guiding center drift model was used for a detailed calculation of commensurability oscillations and their suppression in rectangular geometries. For intermediate magnetic field strengths and not too strong modulations, the results obtained in Ref. [112] by numerical solution of the full Boltzmann equation (which requires heavy numerical work and large computation time) could be reproduced. A direct comparison of the predictions made in Ref. [109] with quantum calculations or experimental results is, however, still missing.

We will reiterate here the physical picture put forward in Ref. [109] and its predictions for modulations with additive potentials in the x- and the y-direction and with different periods $a \neq b$.

7.3.3   2D rectangular modulation

To describe the transport in samples with rectangular superlattices, we assume a simple harmonic modulation potential of the form

$$V(x,y) = V_x \cos(K_a x) + V_y \cos(K_b y) \qquad (7.1)$$

with periods $a \neq b$, $K_a = \frac{2\pi}{a}$ and $K_b = \frac{2\pi}{b}$. The modulation amplitudes V_x and V_y should be comparable in magnitude.

For sufficiently weak V_x and V_y, the classical electron trajectories may be approximated as a superposition $\mathbf{r}(t) = \mathbf{r}_{\mathrm{gc}}(t) + \mathbf{r}_{\mathrm{cyc}}(t)$ of a rapid cyclotron motion $\mathbf{r}_{\mathrm{cyc}}(t) = R_c[\sin(\omega_c t + \alpha_0), -\cos(\omega_c t + \alpha_0)]$ around a slowly moving guiding center $\mathbf{r}_{\mathrm{gc}}(t)$. Such trajectories are
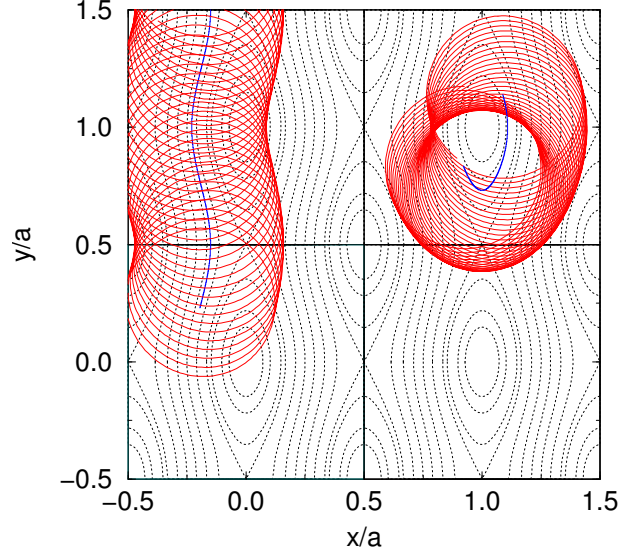
Figure 7.7:
The electron (red) and guiding center (blue) trajectory for a modulation potential $V(x,y) = 0.1 E_{\mathrm{F}}(\cos K_a x + 0.25 \cos K_a y)$ with $K_a = 2\pi/a$ and $qR = 2$. The equipotentials of $V(x,y)$ are dotted. Taken from Ref. [109]

illustrated in Fig. 7.7. According to Refs. [113] and [109], the instantaneous velocity of the guiding center, averaged over a perimeter of the unperturbed cyclotron orbit, is given by [110]

$$\mathbf{v}_{\mathrm{avg}} = -\nabla V_{\mathrm{eff}} \times \mathbf{B}/B^2 , \qquad (7.2)$$

where V^{eff} is an effective potential. Hence the guiding center drifts along the contours of this effective potential

$$V_{\mathrm{eff}}(\mathbf{R}) = \sum_{q \neq 0} e^{i\mathbf{q}\cdot\mathbf{R}} V_{\mathbf{q}} J_0(qR_{\mathrm{c}}) . \qquad (7.3)$$

Here, $\mathbf{R} = (X,Y)$ is the cyclotron orbit guiding center coordinate and J_0 is the Bessel function of the first kind. The $V_{\mathbf{q}}$ are the Fourier coefficients of the modulation potential,

$$V(\mathbf{r}) = \sum_{\mathbf{q} \neq 0} V_{\mathbf{q}} e^{i\mathbf{q}\cdot\mathbf{r}} , \qquad (7.4)$$

with $\mathbf{q} = (n_x K_a, n_y K_b)$. The effective potential $V_{\mathrm{eff}}(\mathbf{R})$ can be understood geometrically: It is the periodic potential $V(x,y)$ averaged over the perimeter of a cyclotron orbit centered at $\mathbf{R} = (X,Y)$ [111, 113]. It has the same periods a and b, but different effective modulation strengths $V_x^{\mathrm{eff}}(B)$ and $V_y^{\mathrm{eff}}(B)$, which in contrast to V_x and V_y depend on the

magnetic field. By studying the equipotentials of this effective potential accurate predictions about the electronic transport are possible.

Considering only fundamental Fourier components for our rectangular lattice, which will prove to be sufficient, we can write the actual potential modulation in the rectangular superlattice in the form of Eqn. 7.1. The corresponding effective potential is given by [55]

$$V^{\text{eff}}(X,Y) = V_x^{\text{eff}} \cos(2\pi X/a) + V_y^{\text{eff}} \cos(2\pi Y/b), \tag{7.5}$$

where

$$V_x^{\text{eff}} = V_x J_0(2\pi R_c/a), \quad V_y^{\text{eff}} = V_y J_0(2\pi R_c/b). \tag{7.6}$$

Three consequences for the transport in 2D modulation potentials result. First, the Bessel functions J_0 for each direction are identical to those found for transport in a corresponding 1D modulated system [43, 44, 108]. Hence, the commensurability oscillation minima found in a 2D modulated system with periods a and b agree with those of the corresponding 1D systems. Second, some of the guiding centers will drift along pinned closed orbits as seen on the right hand side of Fig. 7.7, so they can not contribute to the band conductivity. This suppresses the commensurability oscillation amplitude [109, 113]. Third, the oscillatory magnetic field dependencies of $V_x^{\text{eff}}(B)$ and $V_y^{\text{eff}}(B)$ are different [109], due to the different periods $a \neq b$ (cf. Eqn. 7.6). This will lead to a non-monotonic variation of the commensurability oscillation amplitude [109]: When sweeping the magnetic field, one can find situations with $V_x^{\text{eff}}(B) = 0$, in which the guiding centers can only move along open orbits in x-direction, situations with $V_y^{\text{eff}}(B) = 0$, with only open orbits in y-direction, and situations with $V_x^{\text{eff}}(B) = V_y^{\text{eff}}(B)$, with only closed orbits for the guiding centers. Thus, sweeping B should cover situations with effectively 1D modulations in y- or x-direction and also situations with a strong suppression of the guiding center contribution to the conductivities.

To verify these predictions in experiment, suitable samples have to be produced. Their fabrication procedure is described next.

7.3.4   Sample preparation and measurement procedures

This work was carried out on two different GaAs-AlGaAs heterostructures, #6-159 and #6-100, grown on (100) GaAs substrates by Dr. Vladimir Umansky from the Braun Submicron Research center at the Weizmann Institut of Science in Rehovot, Israel. They have lower mobility than heterostructure #5-74, which was used in the preceding chapters. The
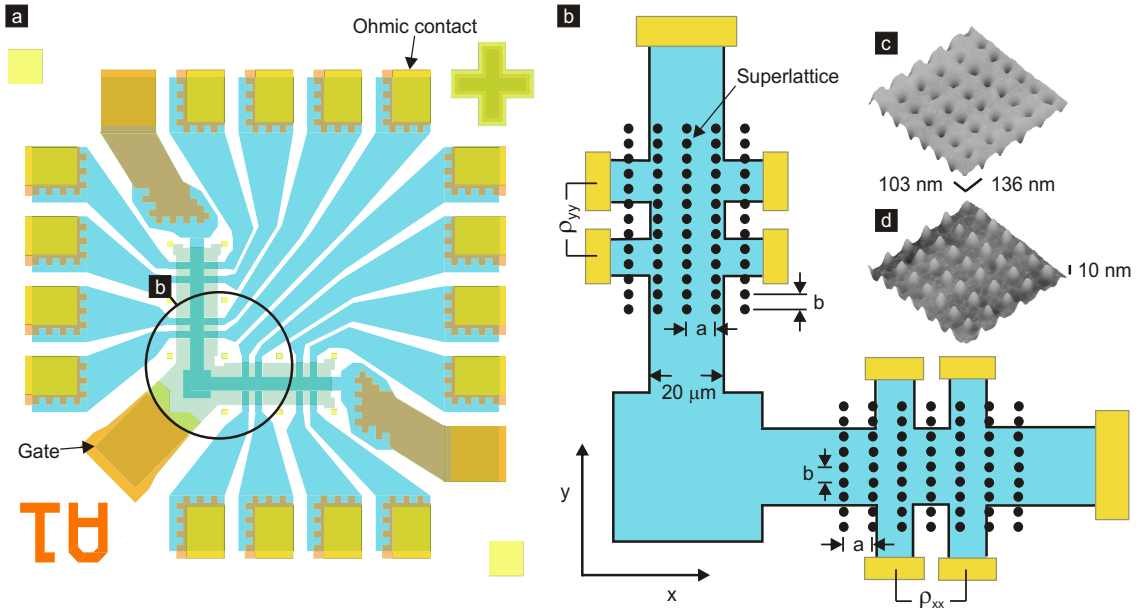
Figure 7.8:

(a) The L-shaped Hall bar mask. The mesa is light blue, alloy regions are orange, contact pads yellow. The optional gate covers the Hall bar and has protruding corners to avoid excessive rounding in the shadow mask etching process. (b) Sketch of the L-shaped Hall bar geometry showing the extent and orientation of the superlattices. The *x*- and *y*-directions coincide with the cleavage directions of the (100) GaAs wafer. (c) Normal and (d) inverted views of a representative AFM measurement on an etched 136 nm by 103 nm period superlattice after removal of the resist.

two heterostructures contained a 2D electron system 42.5 nm below the surface. Hall bars with L-shaped mesas (see Fig. 7.8a,b) were fabricated with standard lithographic techniques. They were 20 μm wide and the geometry factor, L/W, was equal to 1. When unmodulated, the 2D electron system of the first heterostructure #6-159 showed a carrier density of $n_s = 3.2 \times 10^{15}$ m^{-2} and a transport mobility $\mu = 0.8 \cdot 10^6$ cm^2/Vs at 4 K. After a brief illumination with a light emitting diode at 4 K, the mobility improved to $1.0 \cdot 10^6$ cm^2/Vs for a carrier density of 5×10^{15} m^{-2}. In the second heterostructure #6-100, these quantities were $n_s = 3 \times 10^{15}$ m^{-2} and $\mu = 0.83 \cdot 10^6$ cm^2/Vs without illumination and $n_s = 4 \times 10^{15}$ m^{-2} and $\mu = 1.3 \cdot 10^6$ cm^2/Vs after illumination.

a	b	$a:b$	$a \cdot b$
108nm	100nm	1.1	$(104\,\text{nm})^2$
142nm	84nm	1.7	$(109\,\text{nm})^2$
120nm	100nm	1.2	$(110\,\text{nm})^2$
142nm	100nm	1.4	$(119\,\text{nm})^2$
253nm	151nm	1.7	$(195\,\text{nm})^2$
240nm	200nm	1.2	$(219\,\text{nm})^2$
283nm	200nm	1.4	$(238\,\text{nm})^2$

Table 7.1: The periods of the rectangular lattices used for the gated samples.

Electron beam lithography

Patterns of about 50 nm diameter holes arranged on a rectangular superlattice were produced with high resolution electron beam lithography in a 90 nm thick PMMA resist layer coating the Hall bar. The main axes of the rectangular lattices were oriented along and across the Hall bar, i.e. the cleavage directions of the (100) GaAs substrate (see Fig. 7.8b). The area of each superlattice was large enough to cover more than an entire active area on the Hall bar, as depicted in Fig. 7.8b.

The gated samples

In first experiments, the electron beam pattern was transferred to the electron gas using a metal gate as described in section 4.1.3. Several samples with different rectangular lattices were produced to find a suitable range of experimental parameters. The lattice periods and ratios used are listed in table 7.1. The magnetoresistances of the devices were measured after a brief illumination using lock-in techniques introduced in chapter 4.2. The measurement temperature was 4 K in order to suppress the Shubnikov-de Haas oscillations at low B-fields and bring out better the semiclassical guiding center effects. To simultaneously acquire the ρ_{xx}- and ρ_{yy}-magnetoresistances for transport in the two orthogonal directions of the rectangular superlattice, two nominally identical superlattices oriented in the same direction with respect to the crystal directions were produced on the two arms of the L-shaped Hall bar (see Fig. 7.8b in which x and y are the cleavage directions).

Since a more detailed discussion of the features present in experiments on these gated samples follows in section 7.3.7, we will at this point only outline the relevant findings:

The results obtained using the gated samples already confirm all predictions of the guiding center drift model. Additionally, the most suitable range of experimental parameters could be extracted from the large number of gated samples produced: Using modulation periods $a \approx 100$ nm and 130 nm $< b <$ 140 nm, all features expected from theory can be observed in a magnetic field range appropriate for experiment. In such lattices with large ratios $a : b \approx 1.4$, the difference between the modulation amplitudes in the two spatial directions was however getting large ($V_x/V_y \approx 3$). This is due to the stronger attenuation of surface stress for smaller periods. For this reason, a wet etching process was introduced which results in a smaller V_x-V_y-difference for the same ratios of a and b. For the rest of this chapter, we will analyze the experiments on these, even more suitable, etched samples.

The etched samples

A batch of samples was prepared as before, but instead of a metal gate, a room-temperature shallow wet etching process transferred the electron beam pattern to the heterostructure material: First, the oxide on the sample surface was removed by a 15 s etch in 40 ml deionized water with 10 ml concentrated hydrochloric acid and one drop of the surfactant benzalkonium chloride. The surfactant reduces the surface tension of the etchants used. This in turn enables the etchants to reach into the nanoscale holes in the PMMA. As etch stop the sample was dipped into iso-propyl alcohol for 60 s and blown dry in a N_2 flow. To transfer the electron beam pattern, the sample was subsequently etched in 10 ml citric acid solution (prepared by mixing 10 g citric acid monohydrate powder and 10 g deionized water), 30 ml 30% hydrogen peroxide and one drop of surfactant. By changing the etch time from 15 s to 60 s, the etch depth and the resulting modulation strength were adjusted. Finally, the sample was rinsed 30 s in 50 ml deionized water with a drop of surfactant to stop the etching, further rinsed in flowing deionized water for 60 s and blown dry with N_2. The resist was then entirely removed. In AFM studies, the depth of the holes etched at the surface of the Hall bars was found to be about 10 nm. Fig. 7.8c and d display normal and inverted AFM images of the etched superlattice after the removal of the resist. No gate is deposited to avoid stress.

The mobility is reduced by the etching process to $\mu \approx 0.55 \cdot 10^6$ cm^2/Vs at an electron density of $n_s = 4.4 \times 10^{15}$ m^{-2} for heterostructure #6-159 and $\mu \approx 0.65 \cdot 10^6$ cm^2/Vs at $n_s = 4.3 \times 10^{15}$ m^{-2} for heterostructure #6-100. Both superlattices are etched at the same time, and therefore we assume that the modulation strengths are similar for both.

The source of modulation has been identified as originating solely from the depletion

effect. To this end, we studied square superlattices of 100 nm period. At the etched holes, the surface states are closer to the dopants. Hence a density modulation is introduced at the 2D electron system [114]. Combination of this depletion effect and stress modulation is known to introduce asymmetry between the two cleavage directions on (100) GaAs substrates in the case of square superlattices [84, 115]. However, here no asymmetry was observed between the commensurability oscillations for transport along the *x*- and *y*-directions. In view of the absence of asymmetry, we conclude that the modulation is exclusively due to the depletion effect.

For the samples with rectangular superlattices, the resulting modulation amplitude ratio $V_x/V_y \approx 1.5$ for these etched samples is half the one found for gated samples. We will focus on results from these etched samples first.

7.3.5   Key experimental observations

Resistance traces

Figure 7.9 shows the magnetoresistances measured at 4 K for transport along the two axial directions of a rectangular superlattice with lithographic periodicities of $a = 136$ nm along the $[01\bar{1}]$ direction and $b = 103$ nm along the $[011]$ direction of the GaAs crystal ($a : b \approx 1.3$). The *x*-direction is taken along the longer period and the *y*-direction along the shorter period of the modulation. The minima of the commensurability oscillations in the trace for transport along the 136 nm period occur when $2R_c = (k_a - 1/4)a$, where R_c is the cyclotron radius and $k_a = 1, 2, 3, \ldots$, while those in the trace for transport along the 103 nm period coincide with the condition $2R_c = (k_b - 1/4)b$ where $k_b = 1, 2, 3, \ldots$. Hence, the location of the minima is identical to those anticipated for a 1D modulated system with period *a* and *b* respectively [13]. Unique to 2D superlattices of rectangular shape are the following three striking features of the data:

(1) The amplitude of the commensurability oscillation peaks do not monotonically decrease as in 1D-modulated systems. For transport along the longer period (136 nm), i.e. in ρ_{xx}, the commensurability oscillation peak between the $k_a = 3$ and 4 minima is significantly suppressed in amplitude (for instance as compared with its neighboring peak at lower magnetic field, i.e. the commensurability oscillation peak between the $k_a = 4$ and 5 minima).

(2) Similarly, for transport along the shorter period (103 nm), i.e. in ρ_{yy}, the commen-
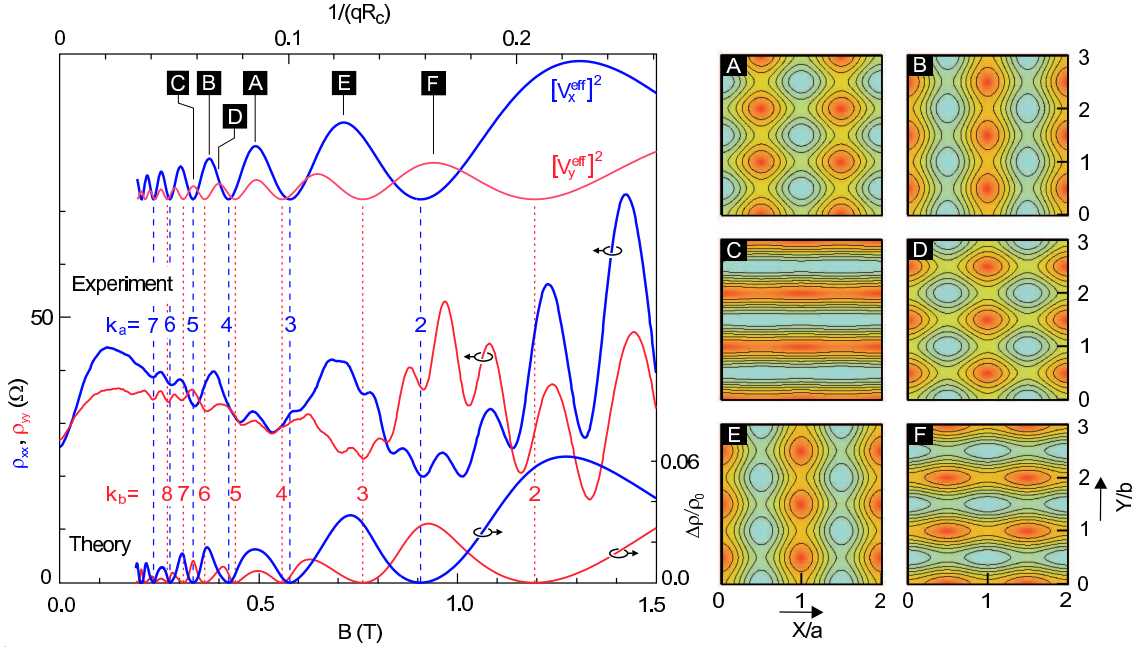
Figure 7.9:
Left panel, middle: Magnetoresistances measured at 4 K for transport along the 136 nm (x-direction, thick blue) and the 103 nm (y-direction, thin red) period directions of a rectangular superlattice. Bottom: Magnetoresistances ρ_{xx} (blue) and ρ_{yy} (red) calculated using Ref. [109] for the parameters $V_x = 5.6\%$ E_F, $V_y = 3.9\%$ E_F, a ratio $a:b = 1.32$ and $q\lambda_{\mathrm{mfp}} = 26$, as estimated in appendix E. The vertical lines indicate the calculated B values of the commensurability oscillation minima of ρ_{xx} for indices k_a (blue dashed) and of ρ_{yy} for indices k_b (red dotted). They coincide with the zeroes of the corresponding effective potential amplitudes $[V_x^{\mathrm{eff}}]^2$ (blue line) and $[V_y^{\mathrm{eff}}]^2$ (red line) shown, in arbitrary units, at the top as function of $1/(qR_c)$. Right panels: A, B, C, D, E and F show the contours of the effective potential $V_x^{\mathrm{eff}}\cos(2\pi X/a) + V_y^{\mathrm{eff}}\cos(2\pi Y/b)$ at the peaks marked in the left graph by A, B, C, D, E and F respectively. The contours in these panels correspond to guiding center trajectories in real space.

surability oscillation peak between the $k_b = 6$ and 7 minima is significantly enhanced in amplitude (compared with its neighboring peak at higher magnetic field, i.e. the commensurability oscillation peak between the $k_b = 5$ and 6 minima).

(3) The large commensurability oscillation peaks between the $k_a = 2$ and 3 minima and the $k_b = 2$ and 3 minima occur when the magnetoresistance in the other axial direction exhibits a broad commensurability oscillation minimum. This corresponds to an interchange of the high and low resistance directions between the two axial directions of the superlattice.

These three characteristics of the commensurability oscillations in rectangular lattices will be referred to as *suppression*, *enhancement*, and *switching*.

7.3.6 Comparison with theory

The behavior of the effective potential

All of these features have been predicted by the theory outlined in Ref. [109]. Hence we follow Ref. [109] and study the behavior of the effective potential $V_{\text{eff}}(\mathbf{R})$ which was already introduced in section 7.3.3: The most notable property of the effective potential in the current context is that the magnetic field dependencies of V_x^{eff} and V_y^{eff} are different, as the arguments of the two Bessel functions involve the different periodicities a and b. The Bessel functions entering the X- and Y-dependent components of the effective potential are identical to those Bessel functions describing the transport in 1D modulated systems along the direction of modulation [43, 44, 108]. The zeroes of these Bessel functions coincide with the commensurability oscillation minima. Hence, in a 2D modulated system with periods a and b the commensurability oscillation minima agree exactly with those of the corresponding 1D systems at the zeroes of $[V_x^{\text{eff}}]^2$ and $[V_y^{\text{eff}}]^2$. For large arguments of the Bessel functions, these zeroes occur in excellent approximation when $2R_c = (k_a - 1/4)a$ and $2R_c = (k_b - 1/4)b$ where $k_a, k_b = 1, 2, 3, \ldots$. Figure 7.9 depicts the B-dependence of $[V_x^{\text{eff}}]^2$ and $[V_y^{\text{eff}}]^2$ (uppermost traces, arbitrary units) for $a = 136$ nm and $b = 103$ nm, calculated for $V_x/V_y = 1.45$. The carrier density 4.4×10^{15} m^{-2}, which determines R_c, is obtained from the Shubnikov-de Haas (SdH) oscillations. Whereas the peak values in the traces of $|V_x^{\text{eff}}|^2$ and $|V_y^{\text{eff}}|^2$ decrease monotonously with decreasing magnetic field, the peak values of the commensurability oscillations in the experimental

traces apparently do not. To understand this, we calculated $\rho_{xx}(B)$ and $\rho_{yy}(B)$ for the same parameter values from the model of Ref. [109] and plotted the results near the bottom of Fig. 7.9. The ratio $V_x/V_y = 1.45$ is chosen in order to obtain for the theoretical resistance traces an overall appearance similar to the corresponding experimental traces (of course apart from the SdH oscillations, which are not included in the calculation). Other values in the range $1.3 \lesssim V_x/V_y \lesssim 1.7$ would also be acceptable and compatible with estimates given in appendix E.

At the zeroes of the Bessel functions, the effective potential amplitudes $[V_x^{\text{eff}}]^2$ and $[V_y^{\text{eff}}]^2$ drop to zero and these zeroes indeed align with the minima of the commensurability oscillations observed in ρ_{xx} and ρ_{yy}. The phases of the squared effective potential amplitudes, plotted as functions of B near the top of Fig. 7.9, are essentially the same as those of ρ_{xx} and ρ_{yy}, respectively. As is evident from the plot, the dominance of $|V_x^{\text{eff}}|$ over $|V_y^{\text{eff}}|$ changes as a function of the magnetic field. The ratio $\alpha_{\text{V}} = |V_x^{\text{eff}}|/|V_y^{\text{eff}}|$ is the key to understanding the various features of the commensurability oscillations in question (suppression, enhancement and switching) as it controls the shape of the effective potential, i.e. the distribution of open and closed contours as well as the direction along which open contours run. Since these contours are the trajectories of the guiding centers in real space, many open contours in a particular direction implies an enhancement of the conductivity in this direction or, equivalently, an increase of the resistivity in the perpendicular direction.

Suppression

In contrast to the peak values of the $|V_x^{\text{eff}}|^2$- and $|V_y^{\text{eff}}|^2$-traces in the upper part of Fig. 7.9, the peak values of the measured commensurability oscillations show a non-monotonous dependence on the magnetic field. For instance, the commensurability oscillation peak in ρ_{xx} (blue curve) between the $k_a = 3$ and 4 minima at the magnetic field position with the label A is much lower than the neighboring peaks at the field values with labels B and E. A similar reduction of the peak height at A is seen in the corresponding theoretical curve for ρ_{xx} at the bottom of Fig. 7.9. The explanation goes as follows: Near A both the $|V_x^{\text{eff}}|^2$ and the $|V_y^{\text{eff}}|^2$ traces have local maxima and the deviation of the ratio α_{V} from 1 is not so large as near B and E, where $|V_x^{\text{eff}}|^2$ has a local maximum while $|V_y^{\text{eff}}|^2$ is close to a local minimum. As a consequence, in the cases B and E the effective modulation in x- direction is much stronger than in y-direction, with many open guiding center trajectories in y-direction. This results in large, quasi-1D commensurability oscillation peaks in ρ_{xx}. At A, on the other hand, the effective potential has 2D character with more closed equipotentials and the commensurability oscillation peak is suppressed as compared with the 1D case.

The contour plots of Fig. 7.9A, 7.9B, and 7.9E, which have been calculated for $|V_y^{\text{eff}}| = 0.60|V_x^{\text{eff}}|$, $|V_y^{\text{eff}}| = 0.32|V_x^{\text{eff}}|$, and $|V_y^{\text{eff}}| = 0.34|V_x^{\text{eff}}|$, support this explanation.

Similar arguments apply to the commensurability oscillation peak in ρ_{yy} (middle red curve: experiment; bottom red curve: theory) at A, which is lower than that labeled D between the $k_b = 5$ and 6 minima. At D we have $|V_x^{\text{eff}}| = 1.07|V_y^{\text{eff}}|$, so that nearly all equipotentials are closed (see Fig. 7.9D) and the guiding center contributions to both ρ_{xx} and ρ_{yy} are suppressed below the corresponding 1D cases. At A, however, we have open trajectories in the y-direction but not in the x-direction, and, as a consequence, the guiding center contribution to ρ_{yy} is even smaller than that to ρ_{xx}, which is already suppressed compared with its neighboring peaks. This behavior is clearly seen in both the theoretical and the experimental results.

Another feature, that is evident in the theoretical curve for ρ_{yy} and less clear but visible also in the experimental curve, is the asymmetry of the commensurability oscillation peaks between $k_b = 3$ and 4 and between $k_b = 5$ and 6. As compared to the corresponding maxima of $|V_y^{\text{eff}}|^2$ in the upper part of Fig. 7.9, the maxima of the theoretical magnetoresistance curve are shifted towards the regions with lower values of $|V_x^{\text{eff}}|^2$, since the guiding center contribution to ρ_{yy} is stronger suppressed in field intervals with $|V_y^{\text{eff}}|^2 < |V_x^{\text{eff}}|^2$ than in those with $|V_x^{\text{eff}}|^2 < |V_y^{\text{eff}}|^2$.

Enhancement

The peak of $|V_y^{\text{eff}}|^2$ marked as C in Fig. 7.9 corresponds to the commensurability oscillation peak in ρ_{yy} between the $k_b = 6$ and 7 minima. At this field value $|V_x^{\text{eff}}|^2$ nearly vanishes, $\alpha_V = 0.05$. Fig. 7.9C displays the guiding center trajectories for this commensurability oscillation peak. One sees only open trajectories which run along the x-direction. This situation is very similar to a 1D modulation in y-direction, with an 1D-like, unsuppressed peak of the guiding center contribution to ρ_{yy} and no guiding center contribution to ρ_{xx}. Compared with the adjacent peaks in ρ_{yy}, the peak at position C appears as enhanced. This effect is present in both the experimental and the theoretical ρ_{yy} traces.

Switching

So far we have compared commensurability oscillation peaks in the ρ_{xx} and the ρ_{yy} curves only with adjacent peaks in the same curve. It is however also interesting to compare the curves with each other.

From the experimental traces in Fig. 7.9 one gets the impression that, in general, the commensurability oscillations in ρ_{xx} are stronger than those in ρ_{yy}. We have adapted potential strengths in the upper part of the figure so that the theoretical curves near the bottom of Fig. 7.9 reproduce this impression. The effective potential $|V_x^{\text{eff}}|$ associated with the longer axial lattice constant is dominant for most of the magnetic field values. Hence, at these magnetic fields, open trajectories of the guiding center exist *exclusively* along the shorter axial lattice constant (y-direction), and the guiding center contribution to ρ_{xx} is considerably larger than that to ρ_{yy}. The commensurability oscillation peaks for transport along the shorter axial lattice constant (ρ_{yy}) at these magnetic fields are, however, not entirely absent. As a consequence of the finite mean free path and modulation strength, a guiding center follows during its lifetime only a fraction of the trajectory and its velocity in x-direction does not average to zero.

Near the magnetic field values labeled B and E and near $B = 1.3\,\text{T}$ the dominance of the commensurability oscillations in ρ_{xx} is clearly seen. There are, however, also B regions where ρ_{yy} is larger than ρ_{xx}, e.g., near the positions labeled C and F. At these positions $|V_y^{\text{eff}}|^2$ has a local maximum while $|V_x^{\text{eff}}|^2$ becomes very small, so that the equipotential patterns of the effective potential are governed by open trajectories in x-direction (see Fig. 7.9C and Fig. 7.9F, which was calculated for $|V_x^{\text{eff}}| = 0.31|V_y^{\text{eff}}|$).

As Fig. 7.9E and F show, the open trajectories in these two cases run along the two orthogonal directions: in the y-direction in the first case and in the x-direction in the second. This corresponds to a complete switching of the guiding center drift direction between the two *axial* directions of the superlattice and an interchange of the high and low resistivity directions. All the features discussed so far are in nice agreement with the theoretical predictions [109].

Limitations of the guiding center model

There are several features of the experimental magnetoresistance traces, which have no counterpart in the theoretical traces at the bottom of Fig. 7.9, obtained within the simple

semiclassical guiding center approximation [109]. For instance to reproduce the pronounced SdH oscillations (observed for $B \geq 0.6\,\mathrm{T}$), one needs a quantum calculation based on a modulation-induced Landau band structure, in which the group velocity takes over the role of the classical guiding center drift velocity. The oscillatory width of Landau bands yields commensurability oscillations, which appear as a modulation of the envelope of the SdH oscillations [44, 49]. The superposition of the SdH oscillations makes it difficult to extract the positions of the commensurability oscillation minima from the experimental curves. Moreover, near these minima, which we understand as band-conductivity minima, one expects maxima of the scattering conductivities, related to DOS maxima [4, 49]. Therefore, near the resistance minima quantum effects may cause differences between the experimental traces and the theoretical traces in Fig. 7.9.

Also the pronounced positive magnetoresistance at very low magnetic fields and the overall decrease of the resistances in the region $0.1\,\mathrm{T} \lesssim B \lesssim 1.0\,\mathrm{T}$ are beyond the scope of the guiding center approach of Ref. [109]. They can be reproduced by classical calculations based on the full Boltzmann equation [112, 116]. The positive magnetoresistance has been explained by the motion of electrons on channeled trajectories along minima of the modulation potential [77, 116]. Even if the guiding center approach seems meaningful (i.e., in Fig. 7.9 for $B \gtrsim 0.2\,\mathrm{T}$), the calculation based on Eq. (7.2) is not always reliable. It has been pointed out in Ref. [109] that Eq. (7.2) does not correctly describe the guiding center motion if the effective potential (7.5) vanishes. At B-values close to the $k_b = 4$ and 5 minima, the effective potentials $|V_x^{\mathrm{eff}}|$ and $|V_y^{\mathrm{eff}}|$ are both very small and the distance of the experimental resistivity minima is apparently considerably smaller than the separation between the minima in the theoretical curves. At present we do not know whether this discrepancy could be resolved within the semiclassical approach [e.g., by a more reliable treatment of the guiding center motion than on the basis of Eq. (7.2)], or whether it is due to the above-mentioned quantum effects.

Finally we remark that, with decreasing B, the commensurability oscillations of the experimental traces decay much faster than those of the theoretical traces. As we know from calculations for 1D superlattices [116–118] as well as for square superlattices [112], this points towards predominant small-angle scattering caused by finite-range impurity potentials. This is also not included in the approach of Ref. [109].

In view of all these limitations of the simple guiding center approach, we cannot expect a quantitative agreement between the calculations of Ref. [109] and the measured magnetoresistivity curves. However, qualitatively all predictions (non-monotonous decrease of commensurability oscillation amplitudes, suppression, enhancement, and switching) are confirmed in our experiments.

7.3.7   Further experiments

Scaling behavior

We have also compared the commensurability oscillations of rectangular superlattices for three different pairs of a and b-values, while preserving the ratio $a : b \approx 1.3$. The superlattices are 150 by 114 nm, 133 by 101 nm and 119 by 91 nm. The longer periods were along the $[011]$ direction and the shorter periods were along the $[01\bar{1}]$ direction. The data are plotted in Fig. 7.10. The magnetic field axis is rescaled as $1/(qR_c)$, where $q = 2\pi/\sqrt{ab}$, to take out both the density dependence and the dependence on period. Because $a : b$ is the same in each case, similar features can be seen at the same value of $1/(qR_c)$. The three commensurability oscillation minima for $k_a = 5$ for instance occur at the same abscissa value in Fig. 7.10.

The important observation in Fig. 7.10 is related to the previously discussed suppressed commensurability oscillation peak between the $k_a = 3$ and 4 minima. When comparing the traces obtained on the different superlattices, the suppression is found to be least effective in the case of the 119 nm period peak and most effective in the case of the 150 nm period peak. The superlattices were fabricated at the same time and hence the depths of the etched holes are expected to be nearly the same in all cases. But the modulation amplitudes are expected to vary. Because of the exponential decay of electric fields with the distance of the 2D electron system from the heterostructure surface [110], a stronger modulation is associated with a larger period. The transport mobilities are essentially the same in all three cases. The data in Fig. 7.10 thus provide evidence of increasing suppression with increasing modulation at a given mobility. This is in agreement with the theory [109]. From Eq.(7.2), we conclude that the magnitude of the velocity of the guiding center drift is proportional to the gradient $|\vec{\nabla}V^{\text{eff}}|$. Therefore, this velocity increases with the modulation amplitude. Hence for a given mobility, if the velocity of the guiding centers is enhanced, more of them will be able to complete closed trajectories, which renders the suppression more effective. Of course, if the modulation is too large, then this picture will not hold as then one cannot average the drift velocity over the unperturbed cyclotron orbit to get the average velocity and Eq.(7.2) loses its validity.

Flattening of the commensurability minima

The data discussed so far were obtained from devices using heterostructure #6-159. Devices from heterostructure #6-100 exhibited stronger modulations. Data for transport
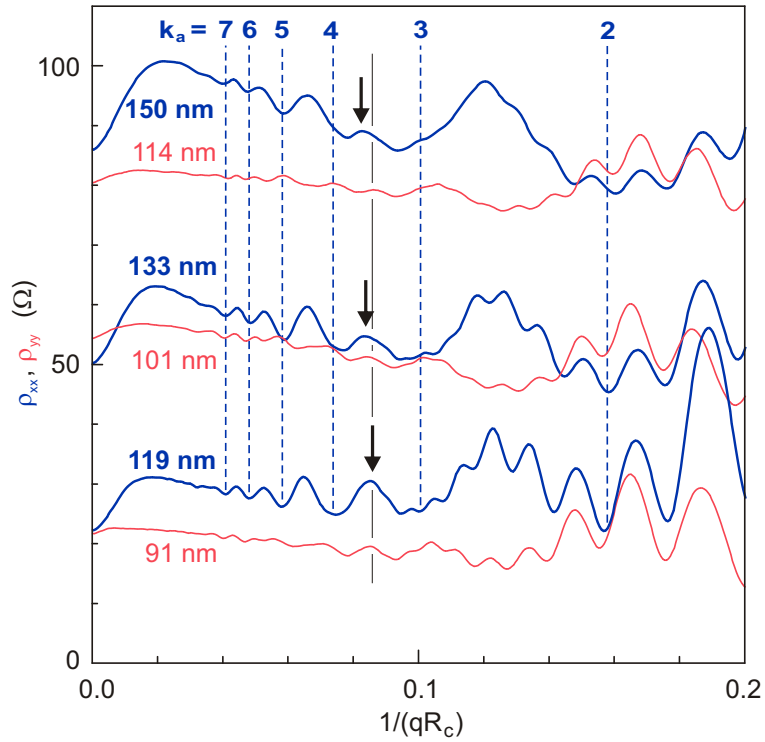
Figure 7.10:

Magnetoresistances measured at 4 K for transport in rectangular superlattices of three different pairs of lattice constants having the ratio 1.3. Thick lines are for transport along the longer periods (ρ_{xx}), thin lines for transport along the shorter periods (ρ_{yy}). The periods are indicated in the plot. For clarity, the middle and the upper pair of traces have been offset by 30Ω and by 60Ω, respectively. The three commensurability oscillation minima (in ρ_{xx}) for $k_a = 5$ occur at the same dashed vertical line. The commensurability oscillation peaks in ρ_{xx} marked by downward arrows between $k_a = 3$ and 4 are increasingly suppressed with increasing modulation period.
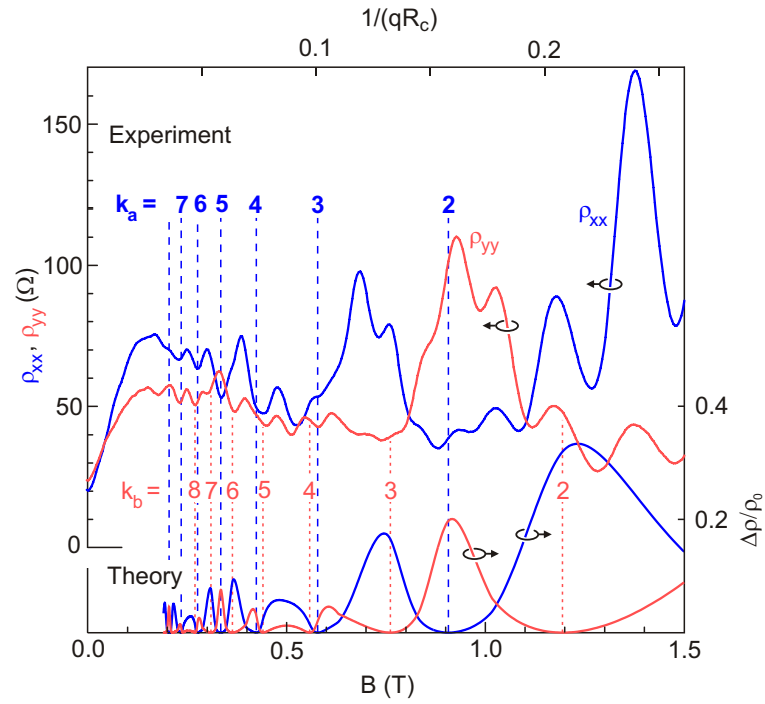
Figure 7.11:
Top: Magnetoresistances measured at 4 K for transport along the 136 nm (thick line) and 103 nm (thin line) period of a rectangular superlattice on heterostructure #6-100. The vertical lines mark the calculated magnetic field values of the commensurability oscillation minima for indices k_a and k_b. Note that the broad commensurability oscillation minima at $k_a = 2$ and $k_b = 3$ are flattened. Bottom: Magnetotransport calculation using Ref. [109] with $V_x = 9\%\ E_F$, $V_y = 7\%\ E_F$, the ratio $a : b = 1.32$ and $q\lambda_{\mathrm{mfp}} = 37$.
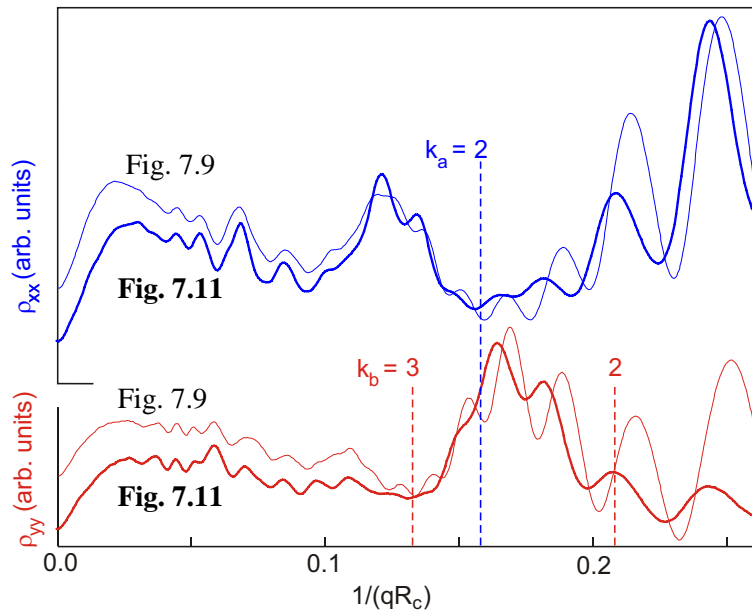
Figure 7.12:
The Magnetoresistances of Fig. 7.9 (thin) and Fig. 7.11 (thick) plotted versus $1/(qR_c)$, so commensurability oscillation minima are aligned. Note that the SdH oscillations for the commensurability oscillation minima at $k_a = 2$ and $k_b = 2, 3$ are suppressed for the thick lines (larger modulation amplitude) as compared to the thin lines.

along the two axial directions of a 136 nm by 103 nm superlattice measured at 4 K after a brief illumination are depicted in Fig. 7.11. The 136 nm period was along the $[01\bar{1}]$ and the 103 nm period was along the $[011]$ direction. As is evident, all the characteristics of the commensurability oscillations discussed in connection with the data of Fig. 7.9 are present in the data of Fig. 7.11. One additional feature in the data is a flattening and broadening of the commensurability oscillation minima in ρ_{xx} and ρ_{yy} at $k_a = 2$ and $k_b = 3$, respectively. This is best illustrated in Fig. 7.12, which is directly comparing the data of Fig. 7.9 (thin line) and Fig. 7.11 (thick line). For sample B (thick line), the SdH oscillations of ρ_{yy} are strongly suppressed near $1/(qR_c) \approx 0.13$, and at $1/(qR_c) \gtrsim 0.2$, and those of ρ_{xx} are suppressed near $1/(qR_c) = 0.15$.

This magnetoresistance feature was predicted for relatively high mean free paths (e.g. for $q\lambda_{\mathrm{mfp}} = 800$ rather than 80; see Fig. 8 of Ref. [109]), and we would expect it to be more pronounced, if we calculate λ_{mfp} from the transport time (this would yield $q\lambda_{\mathrm{mfp}} \gtrsim 300$ for the data of Fig. 7.9). The large transport times in our samples result from the predominance of small-angle scattering, which was not considered in Ref. [109]. Since already small changes of the momentum can lead to trajectories with very different guiding centers, we should calculate λ_{mfp} from the total scattering time τ_0 instead (see appendix E.2). This reduces the $q\lambda_{\mathrm{mfp}}$ values by more than an order of magnitude, and we obtain $q\lambda_{\mathrm{mfp}} \sim 26$ and ~ 37 for the data of Fig. 7.9 and Fig. 7.11, respectively. The modulation amplitudes are, however, much larger for the data of Fig. 7.11. Using the commensurability oscillation peaks between the $k_a = 4$ and 5 minima and the $k_b = 6$ and 7 minima, and the Mirlin and Wölfle [117] theory as described in appendix E.2, the potential amplitudes are estimated to be $V_x = 10\% \, E_F$ and $V_y = 6\% \, E_F$ for the data of Fig. 7.11. Nevertheless, the magnetotransport calculation best reproduces the experimental data of Fig. 7.11 for a smaller ratio $V_x/V_y = 1.3$ and amplitudes $V_x = 9\%$ and $V_y = 7\%$ of E_F. This is still nearly twice as large as the values for Fig. 7.9. According to Ref. [109], larger modulation and larger mean free path are complementary within the limits of the guiding center drift model. Hence, the larger modulation amplitudes enable the observation of this flattening of the commensurability oscillation minima in Fig. 7.11. This effect should be even more pronounced in samples with larger scattering times.

Gated samples

We already presented the conclusions drawn from experiments on gated samples in section 7.3.4. Now we can discuss these results in more detail:

Using the magnetotransport measurements on gated samples using the lattices in table

7.1, the ranges of experimental parameters suitable for an optimal check of the theory were identified. Samples with small superlattice areas $a \cdot b \leq (110 \, \text{nm})^2$ show oscillations due to miniband effects at fields as high as $B = 0.4$ T and with amplitudes comparable to the amplitude modulation of the commensurability oscillations. In lattices with small ratios $a : b \leq 1.2$, the switching effect was not very pronounced, as confirmed by corresponding simulations. In lattices with large ratios $a : b \geq 1.4$, the difference between V_x and V_y is getting big ($V_x/V_y \approx 3$). This is due to the stronger attenuation of a periodical surface stress with small periodicity compared to one with a larger periodicity. The difference in V_x and V_y leads to a strong suppression of the commensurability oscillations for the shorter lattice period. This suppression is visible in ρ_{yy} in Fig. 7.13, where $V_x/V_y \approx 3$. The switching of high- and low-resistance directions with the magnetic field predicted by the guiding center theory is visible in this figure only at certain positions such as the one marked with an arrow. Still, the result of the theory in the bottom part of Fig. 7.13 nicely reproduces the experimental magnetoresistance trace on top. Only the Shubnikov-de Haas oscillations found at higher magnetic fields in experiment are naturally not covered in the semiclassical theory. At even higher ratios $a : b$ the magnetotransport data is more difficult to interpret, simply because the modulation potential shape at the position of the two-dimensional electron gas is not known well enough. Higher Fourier components may play an important role. They are probably present since the electron beam pattern consists of circular symmetric holes on a rectangular grid. Matched oval holes may remedy this problem.

7.3.8 Conclusions

In summary, we have investigated the commensurability oscillations in gated and ungated rectangular two-dimensional superlattices. The characteristic features of the commensurability oscillations can only be explained by the drift of the guiding center of the cyclotron motion along contours of a magnetic-field-dependent effective potential as described in a recent magnetotransport theory [109]. For transport along the longer period, the commensurability oscillation peaks for which the asymmetry of the effective potentials is small were suppressed relative to their neighboring commensurability oscillation peaks at lower magnetic fields. In our systematic study, the suppression was found to be more effective with increasing modulation amplitudes at a given transport mobility. For transport along the shorter periods, the commensurability oscillation peaks at which the effective potentials along the longer periods are small were enhanced relative to their neighboring commensurability oscillation peaks at higher magnetic fields. A magnetic-field-dependent switching of high and low resistance directions between the two axial directions of the superlattices was also observed. Comparison of the data with the the-
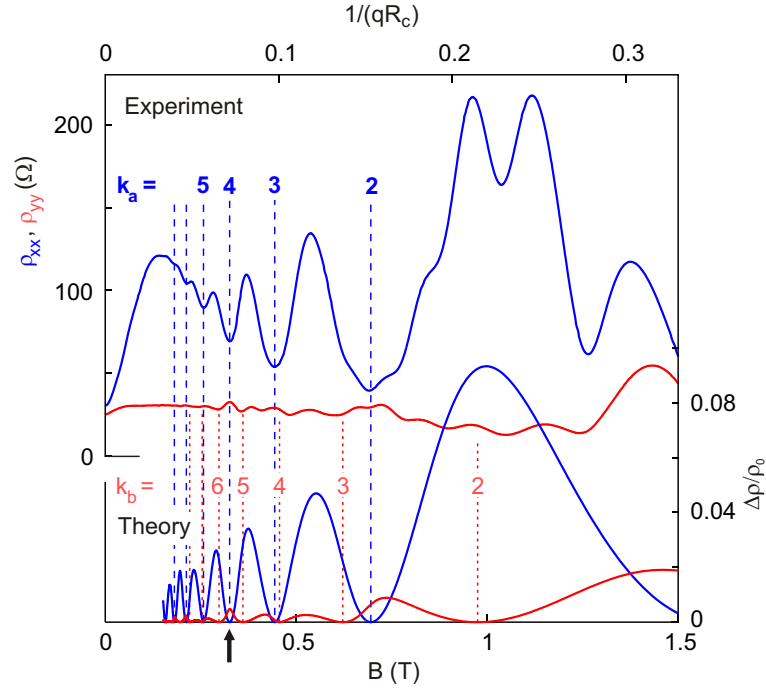
Figure 7.13:

Bottom: Magnetotransport data for a sample with rectangular modulation of 103 nm and 142 nm, mobility $0.8 \cdot 10^6$ cm^2/Vs, and electron density $3.27 \cdot 10^{15}$ m^{-2} Top: The calculated magnetoresistance. Electron density and lattice periods were extracted from experiment. The modulation strengths were taken to be $V_x = 1.5\%$ E_F and $V_y = 4.5\%$ E_F. A mean free path $q\lambda_{\mathrm{mfp}} = 40$ was used.

oretical calculation [109] showed good agreement. For a larger modulation amplitude, we observed a flattening of commensurability oscillation minima, which was predicted by the calculation [109]. None of these characteristic features can be explained by earlier perturbative calculations [110, 111] which are valid for weak modulation only. In particular, the earlier semiclassical and quantum theories predict a monotonic decay of the commensurability oscillation amplitude with decreasing magnetic field which is not the case in the data. Finding a quantum mechanical version of the semiclassical calculation [109] remains as a theoretical challenge.

7.4   Rotated lattices

In this section, we compare experiments on square superlattices which are oriented along different directions of the crystalline lattice. This comparison provides further evidence that the modulation at the position of the two-dimensional electron gas is a consequence of mechanical stress exerted by the metal gate and the piezoelectric properties of the GaAs crystal:

The heterostructures used throughout this work are grown on (100) GaAs substrates. Hall bars are oriented parallel to the {011}-cleavage planes (cf. Fig. 4.1). Except for this section, all samples are modulated with superlattices oriented along the Hall bar and cleavage directions. For this section, similar 100 nm square lattices were produced on the two active areas of a single Hall bar: One of the two superlattices is oriented along the $\langle 011 \rangle$ cleavage directions, the other along the $\langle 001 \rangle$ directions ($45°$). For the rotated lattice, the periodically displaced gate produces hardly any modulation (cf. Fig. 7.14). The remaining weak oscillation can be interpreted as commensurability oscillations due to the diagonal period $a' = 103/\sqrt{2}\,\text{nm} = 73\,\text{nm}$ of the $\langle 001 \rangle$ lattice in the $\langle 011 \rangle$ direction. This observation can be understood as follows: In GaAs, the components of the piezoelectric tensor in the $\langle 001 \rangle$-directions vanish, whereas they are large in the $\langle 011 \rangle$-directions [119]. The metallic gate and patterned PMMA layer underneath act as periodic stressors, but only the stress in the $\langle 011 \rangle$-direction produces a periodic electric field. This fits well with calculations of stress induced modulation potentials [120]. Further evidence comes from experiments on superlattices fabricated by etching and subsequently removing the patterned e-beam resist layer: For the etched samples both orientations of the lattice produce similar modulation. There, the modulation is caused by local depletion instead. As it does not rely on the piezoelectric effect, the orientation is irrelevant.
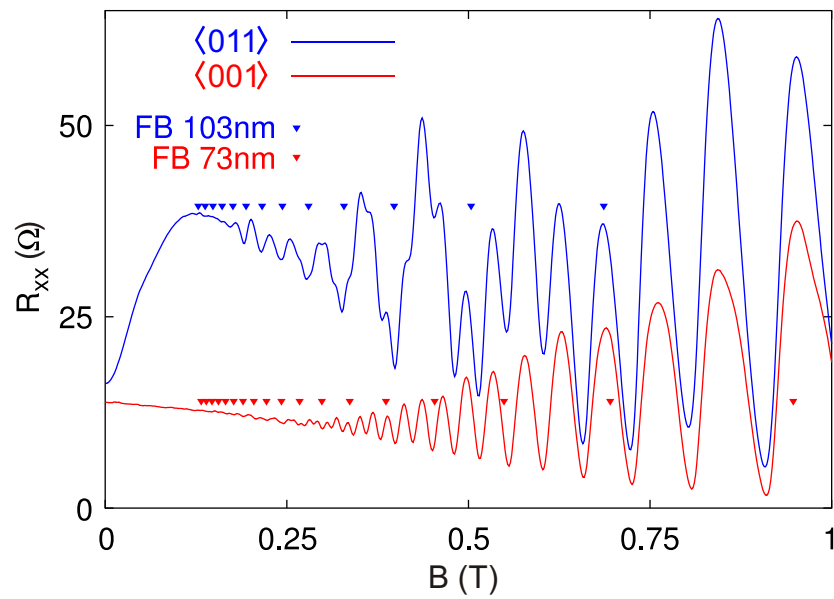
Figure 7.14:
Longitudinal resistances measured at the same time using a Hall bar with two active regions and square lattices oriented along the $\langle 011 \rangle$ and $\langle 001 \rangle$ directions of the GaAs crystal. The flat band conditions are marked with triangles for modulations with periodicities 103 nm and $103/\sqrt{2}$ nm $= 73$ nm. Modulation effects are only clearly visible for the pattern oriented along $\langle 011 \rangle$.

8 Conclusion

In this work, we studied 2D electron systems in a 2D periodically modulated electric potential by means of magnetotransport measurements. Such experiments have been performed for more than a decade, using GaAs/AlGaAs heterostructures, in the search for effects caused by an artificial band structure and due to the competition of characteristic length scales in the system. Here we present samples with modulations of 100 nm periodicity and with the highest reported mean free path to date, thus enabling the measurement of previously-unobserved quantum mechanical phenomena in 2D modulated electron systems.

In strong magnetic fields ($\hbar\omega_c \gg V_0$), the 2D electron system is Landau quantized. This quantization is manifested as Shubnikov-de Haas oscillations in the longitudinal magnetoresistance and as quantized plateaus in the Hall conductance. The additional 2D modulation broadens the discrete Landau levels into bands, which are further subdivided into a certain number of subbands and minigaps. This subdivision is governed by the rational number of flux quanta through a unit cell of the periodic modulation, Φ/Φ_0. The Hofstadter butterfly energy spectrum depicts this arrangement of minibands for a range of Φ/Φ_0. Minigaps should be detectable as additional minima in Shubnikov-de Haas peaks, whereas the Hall conductance should be quantized to values given by the integer solutions to an equation first studied by Diophantus of Alexandria around 250 AD. Recently, definite precursors of this behavior for the primary gaps in the Hofstadter spectrum were demonstrated in a regime where coupling between adjacent Landau bands can be ignored [22]. Due to advances in sample quality, our experiments could go further: we have observed the quantization of the Hall conductance for the largest minigaps and have been able to disclose higher order minigaps in the spectrum. The observation of smaller minigaps is the first indication of the fractal properties of the Hofstadter spectrum. Finally, distortions and rearrangements of subbands are observed within the Hofstadter spectrum. We can ascribe these to Landau band coupling by comparing our

magnetotransport data to theory [23].

For an even more detailed analysis, a calculation of the Hall conductance for the Hofstadter system in the nearly free electron case is essential. The present work has already motivated such a calculation for the first Landau band [95], but further work is needed for the higher Landau bands relevant to the experiments.

For weak magnetic fields ($\hbar\omega_c \ll V_0$), the artificial band structure is the key to understanding the magnetotransport experiments: the artificial 2D crystal, which is defined by the periodic modulation potential, creates energy gaps at the Brillouin zone boundaries. Both closed and open Fermi contours appear. Electrons move on these constant energy contours in k-space and closed orbits should manifest themselves in magnetotransport as $1/B$-periodic oscillations. Due to the finite magnetic field, electrons can tunnel across gaps at the Brillouin zone boundaries and larger closed electron paths should emerge. A first closed path characteristic of a 2D artificial modulation was reported recently [8]. We find a range of additional $1/B$-periodic oscillations which also correspond to such closed orbits. The shapes of these orbits in k-space are discovered in the direct comparison of a density dependent magnetotransport study with a Monte Carlo simulation devised in this work. This simulation correctly predicts the relative probability of the closed orbits observed in our experiment. Moreover, quantum interference of electron paths which share the same starting and ending point should also give rise to $1/B$-periodic oscillations proportional to the enclosed area in k-space. While theory easily finds the most probable interferences for a 1D modulation [14], this becomes an elaborate task for a 2D modulation. We observe and explain, for the first time, quantum interferences characteristic for a 2D artificial modulation. The contributing paths of the large set of quantum interferences found are extracted with the help of a second Monte Carlo simulation. This simulation keeps track of the phase difference which the electron wave function picks up on pairs of paths.

Three of these novel quantum interferences are only present if the modulation potential has second-order Fourier components. Therefore, a Lieb lattice modulation was used in order to introduce additional Fourier components. Additional quantum interferences were observed as a result. Furthermore, two types of unexplained features are encountered in comparing experiment and theory: we find an oscillation which is present only for certain electron density ranges and which has no counterpart in the Monte Carlo simulations. For a modulated sample with a smaller lattice period, two oscillations are suppressed in the vicinity of their crossing. To understand the origin of these features, further theoretical work is needed. Also, experiments with different periodicities or elec-

tron densities may facilitate the observation of crossings of other oscillations.

Finally, we further exploit the possibility of manipulating the properties of the artificial crystal by modifying the geometry of the modulation potential. We are able to verify experimentally a recent prediction for rectangularly modulated samples [109]: in a 1D modulation, commensurability oscillations arise [11, 12]. They are a consequence of the competition between the magnetic length and modulation period. By using different artificial lattice periods in the two spatial directions, we observe an intriguing non-monotonic dependence of the commensurability oscillation amplitudes on the applied magnetic field. Such a dependence is not known for 1D modulations or square artificial lattices. This particular study might be useful for 2D modulated samples where the two directions are modulated by different methods, as in recent experiment in the group of Prof. D. Weiss in which atomic force microscope oxidization is combined with cleaved-edge overgrown samples. In such samples, a non-symmetrical modulation is unavoidable.

9 Deutsche Zusammenfassung

Man stelle sich einen künstlichen Kristall vor, in dem alle räumlichen Freiheitsgrade periodisch moduliert sind, wie in einem natürlichen Kristall, allerdings mit dem Vorteil, daß die Periodizität und Geometrie dieser Modulation nun frei wählbar sind. Da die Gittergeometrie die Basis für viele Effekte in der Festkörperphysik ist, ermöglicht ein solcher künstlicher Kristall das Studium einer ganzen Klasse physikalischer Effekte, die mit natürlichen Kristallen nur schwer oder gar nicht zugänglich wären. Tatsächlich läßt sich solch ein künstlicher Kristall mit 2D-Elektronensystemen auf der Basis von GaAs/AlGaAs Heterostrukturen, auf denen ein periodisches 2D elektrisches Potential aufgeprägt ist [3–5], realisieren. Zumal die Herstellung von künstlichen 3D-Kristallen in entsprechender Qualität noch nicht möglich ist. Entscheidend für die Beobachtung quantenmechanischer Effekte ist dabei eine hohe Probenqualität. Hier konnte die vorliegende Arbeit auf der Basis von hochmobilen GaAs/AlGaAs Heterostrukturen durch optimiertes Aufbringen eines 100 nm periodisch strukturierten metallischen Gates wesentliche Fortschritte erzielen: bislang unerreicht hohe mittlere freie Weglängen wurden realisiert.

Ein zu erwartender Effekt beim künstlichen Kristall ist die Ausbildung einer **künstlichen Bandstruktur** infolge der verkleinerten Brillouinzone und der Lücken, die an den neuen Brillouinzonengrenzen entstehen. Da die Bandstruktur die Bewegung von Elektronen im Kristall festlegt, kann man dies nutzen, um Transporteigenschaften und optische Eigenschaften den Anforderungen entsprechend anzupassen. Effekte dieser künstlichen Bandstruktur können mit Hilfe von Magnetotransportexperimenten untersucht werden: In einem Magnetfeld bewegen sich die am Transport beteiligten Elektronen auf Fermikonturen im k-Raum. Elektronen auf *geschlossenen* Fermikonturen erzeugen Oszillationen im Magnetowiderstand, deren Periodizität charakteristisch ist für die vom Elektron umlaufene Fläche [6]. In unmodulierten Proben entstehen Shubnikov-de Haas Oszillationen [7]. Diese entsprechen der kreisförmigen Fermikontur eines freien Elektrons. Os-

zillationen aufgrund der kleineren geschlossenen Fermikonturen einer künstlichen Bandstruktur sind jedoch im Magnetotransport nicht leicht nachzuweisen. Denn in einem endlichen Magnetfeld können Elektronen im sogenannten magnetischen Durchbruch über die Lücken an den Brillouinzonengrenzen tunneln. Da so Teile von Fermikonturen verschiedener besetzter Minibänder verknüpft werden, können größere geschlossene Elektronenorbits entstehen. Für eine zweidimensionale künstliche Modulation konnte ein solcher Orbit erst vor kurzem im Magnetotransportexperiment beobachtet werden [8]. Die vorliegenden Arbeit nahm diese Suche auf und konnte mit Hilfe der verbesserten Proben eine ganze Reihe von derartigen geschlossenen Orbits nachweisen, was Hoffnung auf die Realisierung einer künstlichen Bandstruktur nährt. Die Formen dieser Orbits im k-Raum wurden mit einer in dieser Arbeit entwickelten Monte-Carlo-Simulation im direkten Vergleich mit den Magnetotransportexperimenten gefunden. Diese Simulation sagt auch die relativen Wahrscheinlichkeiten der nachgewiesenen geschlossenen Orbits voraus.

Ein anderer, bis jetzt unerforschter, quantenmechanischer Effekt in künstlichen 2D-Kristallen ist die **Quanteninterferenz** einer einzelnen Elektronenwellenfunktion, die zwei unterschiedliche Pfade durchlaufen hat. In der Festkörperphysik werden solche Phänomene bereits mit mesoskopischen, ringförmigen Aharonov-Bohm Interferometern untersucht [9]. Dort sind die interferierenden Elektronenpfade und damit auch die von ihnen umschlossene Fläche im Ortsraum festgelegt. Der Phasenunterschied, den die Elektronenwellenfunktion nach dem Durchlaufen der beiden Pfade aufweist, ändert sich linear mit dem angelegten Magnetfeld B. Dies führt zu B-periodischen Oszillationen im Magnetotransport. Könnte man solch ein Interferometer auch im reziproken Raum konstruieren? Dieses Interferometer müßte seine Größe im Ortsraum mit $1/B$ ändern, um im reziproken Raum konstant zu bleiben. $1/B$-periodische Oszillationen im Magnetowiderstand wären die Folge. Genau solch ein System wurde von Stark und Friedberg gefunden [10]. Sie konnten $1/B$-periodische Magnetowiderstandsoszillationen in Magnesium messen, die auf eine Quanteninterferenz zurückzuführen sind. Durch Betrachtung der Fermiflächen von Magnesium machten Sie interferierenden Pfade aus, die für die beobachteten Oszillationen verantwortlich sind. Diese Pfade sind durch magnetischen Durchbruch über zwei Lücken, die verschieden groß sind und auf verschiedenen Brillouinzonengrenzen liegen, schwach gekoppelt. Eine einfachere Interferenz als die von Stark und Friedberg wurde für künstlich 1D-modulierte Proben beobachtet [11–13], jedoch zunächst nur durch die modulationsinduzierte Landaulevelverbreiterung erklärt. Erst in jüngster Zeit wurde erkannt, daß diese Messungen auch durch eine Interferenz im k-Raum erklärbar sind [14]. Allerdings erzeugt die 1D-Modulation nur in einer k-Vektorrichtung Energielücken. Die möglichen Quanteninterferenzen sind deshalb beschränkt auf Pfade, die durch Tunneln über Lücken gekoppelt sind, welche dieselbe Größe haben und auf denselben Brillouinzonengrenzen liegen. Aufgrund dieser Ein-

144

schränkung sind die an der Interferenz beteiligten Pfade leicht zu finden. In der vorliegenden Arbeit wurden nun erstmals Quanteninterferenzen, die für ein künstliches 2D-Kristall charakteristisch sind, beobachtet und erklärt: Nachgewiesen wurden neuartige Quanteninterferenzen von Pfaden, die über zwei Lücken von verschiedener Größe und Position im k-Raum koppeln. Zwar gibt es bei der von Stark und Friedberg vorgestellten Interferenz in Magnesium auch eine derartige Kopplung, aber die in der vorliegenden Arbeit gefundenen Tunnelprozesse in den Interferometerarmen sind nicht vorhanden. Dies hängt zusammen mit der verkleinerten Brillouinzone des künstlichen Kristalls im Vergleich zu einem natürlichen Kristall und der dadurch bedingten großen Anzahl von Lücken im k-Raum. Um aus der großen Menge möglicher Interferometer die wahrscheinlichsten herauszufiltern, wurde in dieser Arbeit eine weitere Monte-Carlo-Simulation entwickelt. Auch ihr Ergebnis stimmt mit dem experimentellen Daten weitgehend überein. Mit Hilfe dieser Simulation kann die detaillierte Bandstruktur bestimmt werden. Sie eröffnet sogar die Möglichkeit, Interferometer im k-Raum zu entwerfen, indem das notwendige künstliche Modulationspotential im Ortsraum der Probe aufgeprägt wird.

Drei der neu gefundenen Quanteninterferenzen benötigen Fourierkomponenten höherer Ordnung im Modulationspotential. Diese Einsicht legt nahe, eine Lieb-Gitter Modulation zu verwenden, bei der weitere Fourierkomponenten zu erwarten sind. So wurden zusätzliche Quanteninterferenzen für diesen Fall gefunden. Die wenigen verbleibenden Differenzen zwischen Experiment und Simulation könnten durch eine über die hier verwendete Näherung hinausgehende Theorie erklärt werden. Dies würde bedeuten, nicht nur einzelne geschlossene Orbits und Paare von Pfaden zu betrachten, sondern das Wechselspiel aller Pfade zu berechnen. Ein derartiger Vorschlag von Pippard [72] hat sich jedoch bis jetzt für eine 2D-Modulation als undurchführbar erwiesen.

Ein künstliches Kristall birgt neben der künstlichen Bandstruktur und ihrer Konsequenzen weiteres Potential zu vielversprechenden quantenmechanischen Effekten, wie dem **Hofstadter Schmetterlingsspektrum**, das schon seit einem halben Jahrhundert theoretisch erforscht wird [15–18] und dessen Selbstähnlichkeit von Hofstadter 1976 demonstriert wurde [19]. Der Schmetterling ist die grafische Darstellung des fraktalen Energiespektrums eines periodischen 2D-Elektronensystems im externen Magnetfeld. Er wird durch die Konkurrenz von zwei charakteristischen Flächenskalen erzeugt: Erstens die Fläche, die genau ein Flußquant $\Phi_0 = h/e$ enthält und zweitens die Einheitszelle des künstlichen Kristalls. Leider sind die Bedingungen für den Hofstadter Schmetterling sehr streng: Der magnetische Fluß durch eine Einheitszelle muß von der Größenordnung eines Flußquants sein. Dies entspricht einem Magnetfeld $B > 60000\,\mathrm{T}$ für typische Halbleitergitter. Magnetfelder dieser Größe sind mit heutigen Anlagen nicht zu erreichen.

Eine Strategie war aus diesem Grund, künstliche Übergitter zu verwenden, die eine deutlich größere Einheitszelle haben, so daß der Schmetterling bei gemäßigten Feldern von $B \approx 1\,\mathrm{T}$ beobachtbar wird. Die in dieser Arbeit dem entsprechend untersuchte Situation kommt dem "*nearly free electron*" Grenzfall eines sehr schwachen Modulationspotentials nahe, das auf ein Landau-quantisiertes Elektronensystem wirkt [17, 20]. Nur am Rande sei hier erwähnt, daß Hofstadter ursprünglich den entgegengesetzten Grenzfall eines "*tight binding*" Elektronensystems in einem relativ schwachen Magnetfeld zu Grunde legte. Es kann jedoch gezeigt werden, daß beide Grenzfälle schließlich auf das gleiche Energiespektrum hinauslaufen [17]. Im "*nearly free electron*" Grenzfall verbreitert sich jedes Landau-Niveau proportional zur Stärke des Modulationspotentials und ist in Minibänder nach Vorgabe des Hofstadter Spektrums unterteilt. Diese Unterteilung in Minibänder wird von der rationalen Anzahl Flußquanten pro Einheitszelle der periodischen Modulation, Φ/Φ_0, bestimmt. Minigaps sollten als zusätzliche Minima in Shubnikov-de Haas Maxima sichtbar werden, während die Hall-Leitfähigkeit quantisierte Werte annimmt, die durch die ganzzahligen Lösungen einer Gleichung mit mehreren Variablen gegeben sind. Diese Gleichung wurde von Diophant von Alexandrien um 250 v. Chr. aufgestellt. Jüngst sind eindeutige Vorboten dieser Merkmale im Magnetotransport für die größten Lücken im Hofstadter Spektrum nachgewiesen worden in einem Bereich, in dem Kopplung von Landaubändern vernachlässigbar ist [22]. Die vorliegende Arbeit geht einen Schritt weiter und zeigt für die größten Minigaps die Quantisierung der Hall-Leitfähigkeit und kann Minigaps höherer Ordnung im Spektrum nachweisen. Die Beobachtung von Minigaps höherer Ordnung ist das erste Indiz für die fraktale Eigenschaft des Hofstadter Spektrums. Das oben angenommene ungestörte Spektrum ist jedoch geringfügig idealisiert: Tatsächlich spielt bei niedrigen Magnetfeldern Landaubandkopplung eine Rolle und kann das beobachtete Spektrum leicht verzerren oder sogar umordnen [23]. Die vorliegende Arbeit kann dies aufgrund der oben erwähnten Probenverbesserungen experimentell nachweisen und hat damit den bis jetzt unerkundeten Bereich über den "*nearly free electron*"-Grenzfall hinaus untersuchen können.

Schließlich wurde die Möglichkeit, die Geometrie des künstlichen Kristalls zu wählen, weiter ausgenutzt: Es ist in dieser Arbeit möglich geworden, eine kürzlich gemachte Voraussage für rechteckig modulierte Proben [109] experimentell zu bestätigen: In 1D-modulierten Proben entstehen Kommensurabilitätsoszillationen [11, 12]. Sie entstehen aufgrund der Konkurrenz zwischen der magnetischen Länge und der Modulationsperiode. Indem die vorliegende Arbeit die künstlichen Gitterperioden in den beiden Raumrichtungen unterschiedlich wählt, kann ein interessantes, nichtmonotones Verhalten der Amplitude der Kommensurabilitätsoszillationen vom Magnetfeld nachgewiesen werden.

Solch eine Abhängigkeit ist bei 1D-Modulationen oder quadratischen künstlichen Gittern nicht vorhanden.

Zusammenfassendes Leitmotiv für den Aufbau dieser Arbeit ist es, die Kluft zwischen Theorie und Experiment durch eng geführte Vergleiche und direkte Gegenüberstellungen zu schließen. Aus diesem Grund werden in allen Hauptabbildungen die experimentellen Daten direkt mit den theoretischen Berechnungen verglichen. Basierend auf diesem Ineinandergreifen von Experiment und Theorie und der dabei sichtbar gewordenen grundsätzlichen Übereinstimmung sind die Kernaussagen dieser Arbeit erst möglich geworden.

Diese Arbeit gliedert sich daher wie folgt:

- In *Kapitel 2* werden die Eigenschaften eines unmodulierten zweidimensionalen Elektronensystems mit Berücksichtigung des Quanten Hall Effekts eingeführt.

- In *Kapitel 3* werden die Grundlagen von 1D- und 2D-modulierten 2D-Elektronensystemen erörtert: Die Konkurrenz zweier charakteristischer Längenskalen, der Modulationsperiode und der magnetischen Länge, führen zu semiklassischen Kommensurabilitätsoszillationen im longitudinalen Magnetowiderstand von 1D-modulierten Proben. Im Grenzfall eines starken Magnetfeldes und einer 2D-Modulation führt diese Konkurrenz zu einem quantenmechanischen Phänomen: dem Hofstadter Schmetterlingsspektrum. Sein Einfluß auf Magnetotransport-Messungen wird herausgestellt, insbesondere auf die quantisierte Hall-Leitfähigkeit. Für den Grenzfall eines schwachen Magnetfeldes wird bei der durch künstliche Modulation erzeugten Minibandstruktur angesetzt und im Anschluß die Fermikonturen und ihre Änderung aufgrund des magnetischen Durchbruchs diskutiert. Es wird beschrieben, wie sich geschlossene Elektronenorbits im Magnetotransport manifestieren.

- In *Kapitel 4* wird der optimierte Prozess zur Probenherstellung und die verwendete Meßtechnik vorgestellt.

- In Kapitel 5 wird das fraktale Hofstadter Schmetterlingsspektrum mittels der quantisierten Hall-Leitfähigkeit experimentell nachgewiesen. Die theoretisch vorhergesagte Umordnung und Deformierung des Spektrums infolge von Landaubandkopplung wird in Messungen bestätigt.

- In *Kapitel 6* wird die Gruppe der wahrscheinlichsten geschlossenen Elektronenorbits ermittelt und im Experiment nachgewiesen. Erstmals werden Quanteninterferenzen, die charakteristisch für ein künstliches 2D-Kristall sind, gemessen und

quantitativ erklärt. Dabei werden Fourier-transformierte Magnetotransportdaten, die bei verschiedenen Elektronendichten gewonnen wurden, genutzt, um Oszillationen im Vergleich mit hierfür entwickelten Monte-Carlo-Simulationen zu identifizieren.

- In *Kapitel 7* wird die Gittergeometrie variiert: Sowohl eine kleinere Gitterperiode als auch ein Lieb-Gitter werden im Hinblick auf Quanteninterferenzen untersucht. Ein unerwartete "vermiedene Kreuzung" von zwei Oszillationen wird beobachtet. Der Einfluß der Fourierkomponenten des Modulationspotentials auf die Quanteninterferenzen wird bestätigt; neue Interferenzen werden gefunden.

  Im zweiten Teil wird die jüngste Voraussage für rechteckige Gitter im Experiment bestätigt: Es wird eine charakteristische nichtmonotone Abhängigkeit der Amplitude der Kommensurabilitätsoszillationen vom Magnetfeld gefunden, die für 1D- und quadratische 2D-Modulationen nicht existiert.

- Die Arbeit schließt mit einer Zusammenfassung im *Kapitel 8*.

- In den *Anhängen* werden Details der Probenherstellung, Meßverfahren und Auswertung gegeben.

A Appendix

A   The fast Fourier Transform

For the analysis presented in chapter 6 each magnetoresistance trace $\rho_{xx}(B)$ is Fourier transformed. To unveil the low frequencies of the novel quantum oscillations in the Fourier transform, the following steps are necessary:

For each measured magnetic field trace only data in the magnetic field range $0.04\,\text{T} < B < 1.1\,\text{T}$ is used for the fast Fourier transform to avoid influence of the positive magnetoresistance around $B = 0\,\text{T}$. Then the data is splined using $N = 2^{14}$ points on an inverted magnetic field axis, since the Fourier transform algorithm is most efficient with input data dimensions that are a power of 2 [121]. The spline is multiplied with the Hanning function

$$\text{Han}(t) = \frac{1}{2} - \frac{1}{2}\cos\left(2\pi\frac{t}{N}\right) \tag{A.1}$$

to reduce leakage and at the same time avoid excessive broadening in the frequency domain [122]. Leakage is inherent in the discrete Fourier transform due to the unavoidable truncation of the input data. Truncation results in a sharp discontinuity and leads to sidelobes in the frequency domain. Using the Hanning as a truncation function removes the discontinuities. To avoid zero frequency contributions in the Fourier transform, the sum over the magnetoresistivities $\sum\rho_{xx}(B)\text{Han}(1/B)\Delta(1/B)$ should be zero. This is achieved by subtracting a constant c from each ρ_{xx} value. This constant is given by

$$
\begin{aligned}
\sum(\rho_{xx}(B) - c)\,\text{Han}(1/B)\,\Delta 1/B &= 0 \\
\Leftrightarrow \qquad \sum\rho_{xx}(B)\,\text{Han}(1/B) &= c\sum\text{Han}(1/B) \\
\Leftrightarrow \qquad\qquad c &= \frac{\sum\rho_{xx}(B)\,\text{Han}(1/B)}{\sum\text{Han}(1/B)}\ .
\end{aligned}
\tag{A.2}
$$

The result is seen in the middle row (b,e) of Fig. A.1. It is padded with $(M-1)\cdot N = (2^4 -$
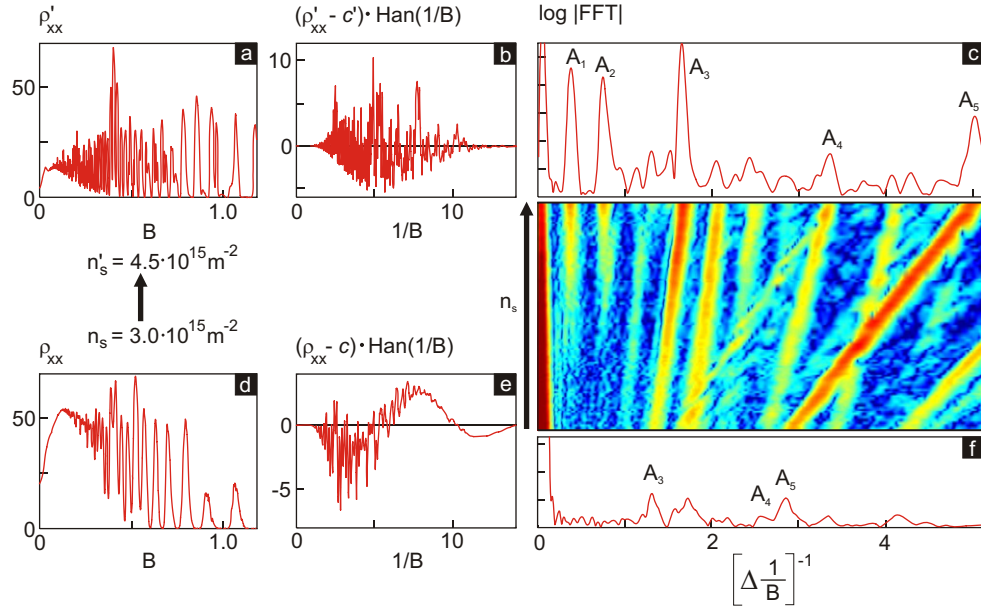
Figure A.1:
   (a) Magnetotransport measurement at an electron density of $4.5 \cdot 10^{15}$ m^{-2}. (b) Conversion of the raw data for the Fast Fourier transformation. (d,e) Same for lower electron density of $3 \cdot 10^{15}$ m^{-2}. Right: Color plot of $\log|\text{FFT}|$ for a large set of densities. (c,f) The Fourier transformations of b) and e). Peaks associated with oscillations of the same origin are marked for clarity.

$1) \cdot 2^{14}$ zeroes. This padding yields an interpolated Fourier transform of length 2^{18} [123]. This amount of data points is necessary to provide sufficient resolution for the final plot, which has again an inverse abscissa $(\Delta 1/B)^{-1}$. The end result is a color plot of the natural logarithm of the absolute value of the complex Fourier transform $\log(|\text{FFT}(\text{Han}(\rho_{xx} - c))|)$, as seen in Fig. A.1. These are presented in chapter 6.

B   Electron beam lithography

Two lithography systems produced the lattice patterns needed in this work (cf. table A.1):

For the square lattices used in chapters 5 and 6, a high reproducibility was needed to optimize the subsequent evaporation steps. These patterns were produced in the "Mikrostrukturlabor" of Prof. H. Schweizer at the University of Stuttgart by Mrs. H. Gräbeldinger us-

Electron beam lithography system	Acceleration voltage	Resist thickness	Samples used in chapters
Jeol IBX5DII (Univ. Stuttgart)	50 kV	200 nm	5,6
Leica EBL100-03 (MPI Stuttgart)	95 kV	90 nm	7

Table A.1: The two electron beam systems.

ing a Jeol lithography system. In the Jeol system, the samples are pressed flush with the resist-covered surface onto the backside of a metal sample holder. This sample holder has an aperture through which the exposure takes place. This ensures an optimal perpendicular alignment of the sample surface with the electron beam gun. The sample surface can be held in focus even for a deflected electron beam. Additionally, the sample is moved laterally so that each writing field is centered under the electron beam gun when the exposure takes place. Hence, all patterns exposed during one run share the same writing quality.

In the Leica system used by Mrs. U. Waizmann at the Max-Planck Institute for Solid State Research in Stuttgart, the samples lie with the backside on an immobile sample holder. An irregular sample backside or dirt between the sample and its holder will translate into a non-perpendicular alignment of the sample surface and the electron beam gun. The change in the distance between the sample and the electron beam gun across the writing fields can cause a change in beam spot size and hence in the quality of the written patterns. Hence, these samples are not ideal to optimize subsequent processing steps. Still, using the already optimized gate production steps with adapted gate material thicknesses and angles, all samples with non-square geometries, as presented in chapter 7, were produced using patterns exposed by this system.

Since the two lithography systems use different acceleration voltages, the damage done by electrons entering the heterostructure during exposure was studied. The effect of the electron beam lithography on the mobility is less than 10% and no systematic dependence on the two different acceleration voltages is observed.

Since the total exposure time is proportional to the area being written, only the parts important for the measurement around the Hall bar and voltage probes are exposed. To be insensitive to alignment errors in the lithography, the pattern area was chosen to be 80 μm wide while the Hall bar width is only 20 μm.

C   The self-adapting illumination process

To obtain magnetotransport measurements at a continuous range of electron densities, a self-adapting illumination process was devised. This process is illustrated in Fig. A.2. In the beginning, an LED current variable is initialized to $I_{ON} = 10^{-7}$ A. The gate voltage is $V_G = 0.05$ V. It is lowered to zero during illumination. When the Hall voltage $V_{xy}|_{B=-0.05\mathrm{T}}$ settles, the electron density is estimated and a magnetotransport measurement is initiated if the desired density is reached or if the sample was already illuminated 10 times. In both cases, the LED current I_{ON} for the next illumination is decreased to avoid large increases in electron density. If both conditions are not met, the LED current I_{ON} is increased by 10%. The program stops when the LED current exceeds 100 mA.

Compared to manual illumination, much higher maximal densities are reached: Small LED currents are used repetitively over a long period of time to reach the target density, so excessive heating is avoided.
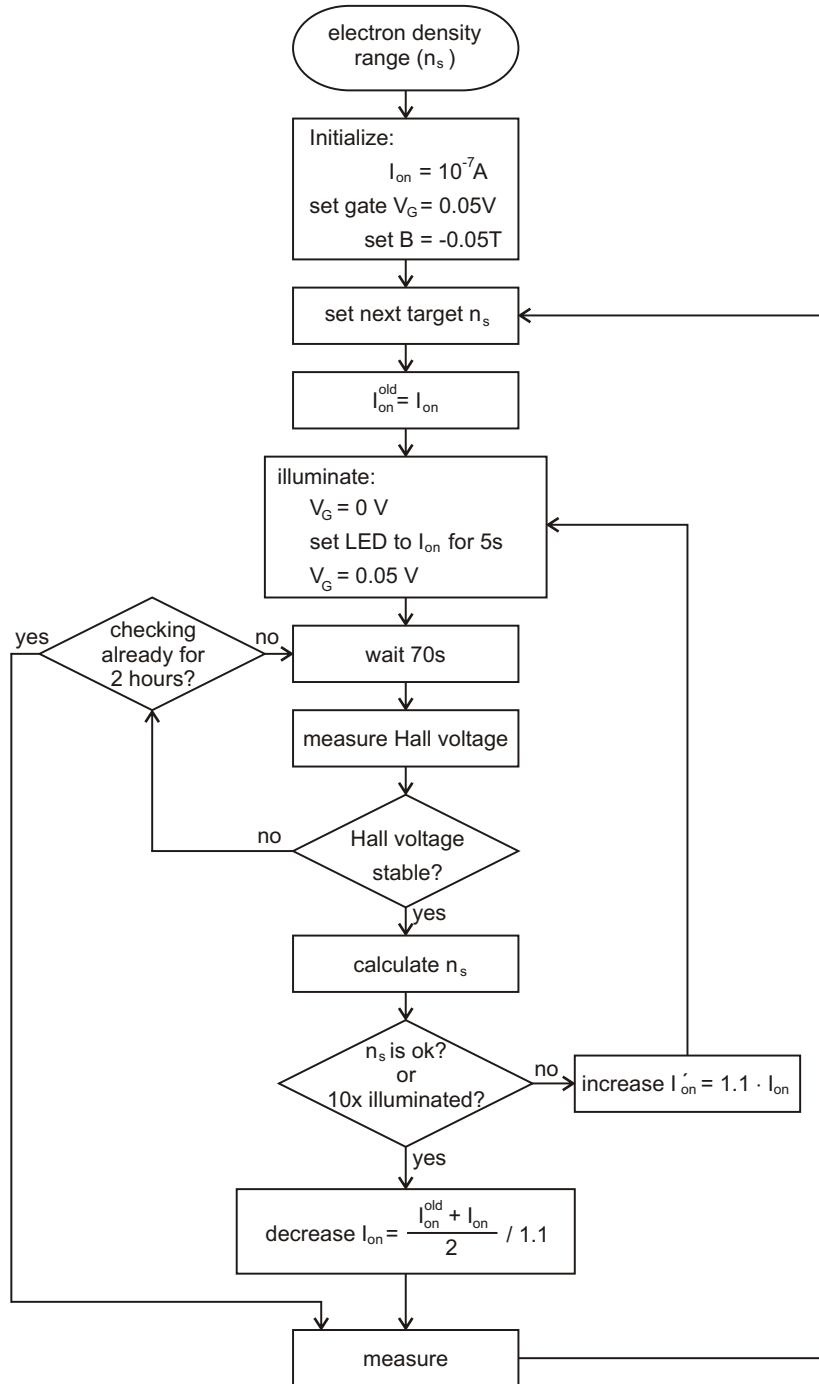
Figure A.2:
The automated LED illumination and measurement flowchart. The electron density is determined from a measurement of the Hall voltage at $B = -0.05$ T.

D   Fourier components important for the orbits and quantum interferences

To calculate the round-trip probability of a closed trajectory, we need the number of times $n_{\mathbf{q}}^{\text{tunnel}}$ an electron on this trajectory has to tunnel over a gap. Here, $\mathbf{q} = K_a \cdot (n_x, n_y)$ is the reciprocal lattice vector perpendicular to the Brillouin zone boundary the gap lies on. Gaps open up only for Fourier components $V_{\pm\mathbf{q}}$. Also the non-tunnel event counts $n_{\mathbf{q}}^{\text{non}-\text{tunnel}}$ are needed. Both $n_{\mathbf{q}}^{\text{tunnel}}$ and $n_{\mathbf{q}}^{\text{non}-\text{tunnel}}$ for the closed orbits of Fig. 6.6 are listed in table A.2. The upper part of the table is for an electron density of $n_{\mathrm{s}} = 4.24 \cdot 10^{11} \text{cm}^{-2}$, the lower part for $n_{\mathrm{s}} = 2.9 \cdot 10^{11} \text{cm}^{-2}$. For the numbers in brackets, $V_{K_a \cdot (n_x, n_y)}$ is zero, no gap is present and the electron does not need to tunnel.

Closed orbit	Non-tunnel (1,0)	(1,1)	Tunnel (1,0)	(1,1)	(2,0)	(2,1)	(2,2)
A	4			8	(8)	(8)	(8)
B	2		4	8	(8)	(12)	(8)
C	4		4	8	(8)	(16)	(8)
D			8	8	(8)	(16)	(8)
E	6		4	8	(8)	(20)	(8)
F	2		8	8	(8)	(20)	(8)
G	4		8	8	(8)	(24)	(8)
A	4			8	(8)	(8)	
B	2		4	8	(8)	(12)	(4)
C	4		4	8	(8)	(16)	(8)
D			8	8	(8)	(16)	(8)
E	6		4	8	(8)	(20)	(12)
F	2		8	8	(8)	(20)	(12)
G	4		8	8	(8)	(24)	(16)

Table A.2:
The non-tunnel counts, $n_{\mathbf{q}}^{\text{non}-\text{tunnel}}$, and tunnel counts, $n_{\mathbf{q}}^{\text{tunnel}}$, for the closed orbits (A-G) of Fig. 6.6. The reciprocal lattice vectors $\mathbf{q} = K_a \cdot (n_x, n_y)$ are given in units of K_a as column title. The upper half of the table is for an electron density of $n_{\mathrm{s}} = 4.24 \cdot 10^{11} \text{cm}^{-2}$, the lower half for $n_{\mathrm{s}} = 2.9 \cdot 10^{11} \text{cm}^{-2}$. For the numbers in brackets, the Fourier components $V_{K_a \cdot (n_x, n_y)}$ are zero, so no gap is present and the tunneling probability is 1.

Table A.3 lists the same counts for the quantum interferences (a-m) of Fig. 6.10. Here, additionally the positions of the interference points are given. Quantum interferences (a,b,c) include non-tunnel events or interference points on the second Brillouin zone boundary,

Quantum interference	Non-tunnel		Tunnel					Interference	
	$(1,0)$	$(1,1)$	$(1,0)$	$(1,1)$	$(2,0)$	$(2,1)$	$(2,2)$	$(1,0)$	$(1,1)$
a		1	2	2	(4)	(6)	(4)	2	
b		1	2	4	(4)	(10)	(4)	2	
c	1		3	5	(6)	(10)	(6)	1	1
d	2		2	8	(8)	(12)	(8)	2	
e			6	8	(8)	(16)	(8)	2	
f	2		6	8	(8)	(20)	(8)	2	
g	4		6	8	(8)	(24)	(8)	2	
h	4		2	8	(8)	(16)	(8)	2	
i	2		6	8	(8)	(20)	(8)	2	
j	6		2	8	(8)	(20)	(8)	2	
k	2		6	12	(12)	(20)	(12)	2	
l	4		6	12	(12)	(24)	(12)	2	
m	2		8	12	(12)	(24)	(12)	2	

Table A.3:
  The non-tunnel counts, $n_{\mathbf{q}}^{\mathrm{non-tunnel}}$, tunnel counts, $n_{\mathbf{q}}^{\mathrm{tunnel}}$, and interference positions for the quantum interferences (a-m) of Fig. 6.10. The electron density is $n_{\mathrm{s}} = 4.24 \cdot 10^{11} \mathrm{cm}^{-2}$. The reciprocal lattice vectors $\mathbf{q} = K_a \cdot (n_x, n_y)$ are given in units of K_a as column title. For the numbers in brackets, the Fourier components $V_{K_a \cdot (n_x, n_y)}$ are zero, so no gap is present and the tunneling probability is 1.

corresponding to a $\mathbf{q} = K_a \cdot (1,1)$. When the Fourier component $V_{K_a \cdot (1,1)}$ is zero, the total probability of all three quantum interferences goes to zero.

E   Estimate of modulation amplitudes in rectangular lattices

E.1   From the surface modulation

Since in Fig. 7.9 the commensurability oscillations of ρ_{xx} are apparently stronger than those of ρ_{yy}, the amplitude of the potential modulation in x direction should be larger than that of the potential modulation in y direction. To obtain a crude estimate, [124] argues as follows.

The GaAs surface of the heterostructure is assumed to be an equipotential, due to the well-known mid-gap pinning of the Fermi level by surface states. Etching the holes into the surface produces a periodically corrugated surface of constant potential. We crudely simulate this with a periodic potential

$$V(x,y) = V_B + \sum_{n,m} V_0 \, e^{-[(x-na)^2 + (y-mb)^2]/\sigma_{\mathrm{hl}}^2} \tag{E.3}$$

in the $z = 0$-plane (top surface). Here $V_B \approx 0.7\,\mathrm{eV}$ describes the Schottky barrier and $\sigma_{\mathrm{hl}} \approx 25\,\mathrm{nm}$ is the radius of the etched holes. The magnitude of this periodic component of the potential V_0 is estimated from the depth $d \approx 10\,\mathrm{nm}$ of the holes and the distance $D \approx 40\,\mathrm{nm}$ between the surface and the 2D electron system as $V_0 \sim V_B d/D$. Fourier expansion of the potential (E.3) yields for the Fourier coefficients of the external potential in the plane $z = D$ of the 2D electron system

$$V_{\mathbf{q}} \approx V_0 (\pi \sigma_{\mathrm{hl}}^2/ab) \exp(-qD - q^2 \sigma_{\mathrm{hl}}^2/4)\,, \tag{E.4}$$

with $q = |\mathbf{q}|$ and $\mathbf{q} = (n_x K_a, n_y K_b)$. Considering only the fundamental harmonics with $(n_x = \pm 1, n_y = 0)$ and $(n_x = 0, n_y = \pm 1)$, we obtain for the relevant modulation potential Eq. (7.1) with

$$V_x = 2\left[V_{\mathbf{q_x}}/\varepsilon(\mathbf{q_x})\right], \quad V_y = 2\left[V_{\mathbf{q_y}}/\varepsilon(\mathbf{q_y})\right], \tag{E.5}$$

where $\mathbf{q_x} = (K_a, 0)$, $\mathbf{q_y} = (0, K_b)$, and the dielectric constant $\varepsilon(\mathbf{q}) = 1 + 2/(a_B^\star q)$. Here $a_B^\star \approx 10\,\mathrm{nm}$ is the effective Bohr radius. It describes the static screening by the 2D electron system (for zero and small B). Putting in numbers, we obtain $V_x \sim 1.0\,\mathrm{meV} \sim 7\% E_F$ and $V_y \sim 0.6\,\mathrm{meV} \sim 4\% E_F$, with $E_F \approx 15.7\,\mathrm{meV}$ for a 2D electron density of $4.4 \cdot 10^{11}\mathrm{cm}^{-2}$. These modulation strengths are of a reasonable order of magnitude, although the ratio $V_x/V_y \sim 1.7$ is somewhat larger than that used in the discussion of Fig. 7.9. The weak points of this estimate are the crude ansatz of Eq. (E.3) and the neglect of the effect of the "short illumination" of the sample at $4\,\mathrm{K}$, which may change the

charge distribution in the Si-doped layer and, thereby, the screening properties. Additional screening will reduce the values of V_x and V_y, but probably also the ratio V_x/V_y.

E.2   From the amplitude of commensurability oscillations

At present, no theoretical calculation on 2D superlattices is available to directly extract the potential amplitudes from the magnitude of the commensurability oscillations. Referring back to Fig. 7.9, one can see that for some of the commensurability oscillation peaks, the effective potential is close to 1D. Although this quasi one-dimensionality refers only to the effective potential, which according to Eq. (7.2) describes approximately the guiding center motion [109], we will use such situations to estimate the modulation strengths.

Analytic forms of the magnetic field dependence of the commensurability oscillations for 1D superlattices have been proposed by Mirlin and Wölfle [117]. They took into account the effect of small angle scattering (which is a characteristic of the scattering due to remote ionized impurities) on the decay of commensurability oscillations with decreasing magnetic field. From the data of Fig. 7.9, we use the height $\Delta\rho$ of the commensurability oscillation peak between the $k_a = 4$ and 5 minima to estimate the potential amplitude associated with the 136 nm period and the $k_b = 6$ and 7 minima for the potential amplitude associated with the 103 nm period, respectively. For this magnetic field range Eq. (49) of Ref. [117],

$$\frac{\Delta\rho}{\rho_0} = \frac{\eta_V^2}{4} \left(\frac{2\pi R_c}{a}\right) \omega_c \tau_{tr} \left[1 + 2e^{-\pi/(\omega_c\tau_0)} \sin\left(\frac{4\pi R_c}{a}\right)\right], \qquad (E.6)$$

is appropriate. The potential amplitude V_0 can be calculated from $\eta_V = V_0/E_F$. In Eq. (E.6) $\Delta\rho$ is the deviation of the resistivity from the Drude zero field resistivity ρ_0 and $\omega_c = eB/m$ is the cyclotron frequency. The classical transport (momentum relaxation) time $\tau_{tr} \approx 20$ ps, defined by the Drude conductivity $\rho_0^{-1} = e^2 n_{el} \tau_{tr}/m$, is calculated from the mobility $\mu \approx 0.55 \cdot 10^6$ cm^2/Vs of the sample. For a high-mobility 2D electron system in a GaAs sample it may be much larger than the total (quantum) scattering time τ_0, defined by the imaginary part $\hbar/2\tau_0$ of the single-electron self-energy [125]. Unfortunately we know little about the ratio τ_{tr}/τ_0 for our modulated samples. Taking as a reasonable estimate $\tau_{tr}/\tau_0 \approx 13$ [126], we obtain $\tau_0 \approx 1.5$ ps, and $q\lambda = 26$ for the scaled mean free path. This value has been used in Fig. 7.9 and in the discussion in connection with the "flattening" in Fig. 7.11. The potential modulation amplitudes obtained from Eq. (E.6) are then $V_x = 5.9\% \ E_F$ and $V_y = 3.5\% \ E_F$, with $V_x/V_y = 1.7$.

E.3   From the positive magnetoresistance

In 1D superlattices the modulation amplitude can be estimated from the saturation field B_0 of the positive magnetoresistance at low magnetic fields as described in section 3.2.5. Semiclassical calculations have shown that for the small V_0 present here the positive magnetoresistance stays the same in amplitude and shape for a symmetric 2D modulation [112]. This motivates the estimate of V_0 even for the 2D modulation case using formula 3.20. We find for the data of Fig. 7.9 $V_x = 4.8\%$ and $V_y = 3.8\%$ of the Fermi energy, with $V_x/V_y \approx 1.3$.

Since all the mentioned estimates in this appendix yield modulation amplitudes of the same order of magnitude, we believe that our choice of $V_x = 5.6\%$ E_F and $V_y = 3.9\%$ E_F with ratio $V_x/V_y = 1.44$ as model parameters is reasonable for a qualitative understanding of the experimental results. We also use this insight to motivate our choice of formula 3.20 to estimate V_0 of square modulation potentials in section 4.4.

F   Software packages used

Two C++ software packages were used in chapter 6 for the Monte Carlo simulations:

LEDA [2] was used for its *leda_real* type. This type can represent results of square roots without rounding error and is used for all coordinates, angles and areas in the problem. This allows even after many calculation steps an exact comparison of two areas to decide whether they are equal or not. The collection of correct statistics for the trajectories found in the Monte Carlo simulation would not be possible with a standard floating point number which is clipped internally after a finite number of digits.

The open source CGAL [1] library provides access to general geometric algorithms from computational geometry. It is a collaborative effort of several sites in Europe and Israel. From this library the geometric primitives such as points, vectors, lines and circles were used. It allows to query intersections and neighbor relations of points, segments and areas. The whole library had to be extended however to exploit the circular boundary condition present in the problem in this work.

The final C++ code for the Monte Carlo simulation excluding the libraries was 5000 lines long.

Bibliography

[1] CGAL-2.4, *Computational Geometry Algorithms Library* (Cgal collaboration, http://www.cgal.org, 2002).

[2] LEDA-4.2, *Library of Efficient Data types and Algorithms* (Algorithmic Solutions Software GmbH, http://www.algorithmic-solutions.com, 2001).

[3] G. Bernstein and D. K. Ferry, J. Vac. Sci. Technol. B **5**, 964 (1987).

[4] R. R. Gerhardts, D. Weiss, and U. Wulf, Phys. Rev. B **43**, 5192 (1991).

[5] C. W. J. Beenakker and H. van Houten, in *Semiconductor Heterostructures and Nanostructures*, Vol. 44 of *Solid State Physics*, edited by H. Ehrenreich and D. Turnbull (Academic Press, San Diego, 1991), .

[6] L. Onsager, Phil. Mag. **43**, 1006 (1952).

[7] L. Shubnikov and W. J. de Haas, Leiden Comm. **207a-d,210a**, (1930).

[8] C. Albrecht, J. H. Smet, D. Weiss, K. von Klitzing, R. Hennig, M. Langenbuch, M. Suhrke, U. Rössler, V. Umansky, and H. Schweizer, Phys. Rev. Lett. **83**, 2234 (1999).

[9] R. A. Webb, S. Washburn, C. P. Umbach, and R. B. Laibowitz, Phys. Rev. Lett. **54**, 2696 (1985).

[10] R. W. Stark and C. B. Friedberg, Phys. Rev. Lett. **26**, 556 (1971).

[11] D. Weiss, K. von Klitzing, K. Ploog, and G. Weimann, Europhys. Lett. **8**, 179 (1989).

[12] D. Weiss, K. von Klitzing, K. Ploog, and G. Weimann, in *High Magnetic Fields in Semiconductor Physics II*, Vol. 87 of *Springer Series in Solid-State Science*, edited by G. Landwehr (Springer Verlag, Berlin, 1989), p. 357.

[13] R. R. Gerhardts, D. Weiss, and K. von Klitzing, Phys. Rev. Lett. **62**, 1173 (1989).

[14] R. A. Deutschmann, W. Wegscheider, M. Rother, M. Bichler, G. Abstreiter, C. Albrecht, and J. H. Smet, Phys. Rev. Lett. **86**, 1857 (2001).

[15] P. G. Harper, Proc. R. Phys. Soc. (London) Ser. A **68**, 874 (1955).

[16] M. Y. Azbel, Sov. Phys. JETP **19**, 634 (1964).

[17] D. Langbein, Phys. Rev **180**, 633 (1969).

[18] A. Rauh, Phys. Stat. Solidi B **69**, K9 (1975).

[19] D. R. Hofstadter, Phys. Rev. B **14**, 2239 (1976).

[20] D. Pfannkuche and R. Gerhardts, Phys. Rev. B **46**, 12606 (1992).

[21] T. Schlösser, K. Ensslin, J. P. Kotthaus, and M. Holland, Europhys. Lett. **33**, 683 (1996).

[22] C. Albrecht, J. H. Smet, K. von Klitzing, D. Weiss, V. Umansky, and H. Schweizer, Phys. Rev. Lett. **86**, 147 (2001).

[23] D. Springsguth, R. Ketzmerick, and T. Geisel, Phys. Rev. B **56**, 2036 (1997).

[24] K. Ploog, Angew. Chem. **100**, 611 (1988).

[25] F. Stern and S. D. Sarma, Phys. Rev. B **30**, 840 (1984).

[26] V. Fock, Zeitschrift für Physik **47**, 446 (1928).

[27] P. W. Anderson, Phys. Rev. B **109**, 1492 (1958).

[28] R. B. Laughlin, Phys. Rev. B **23**, 5632 (1981).

[29] L. Onsager, Phys. Rev. **37**, 405 (1931).

[30] H. B. Casimir, Rev. Mod. Phys. **17**, 343 (1945).

[31] in *Statistical Physics*, No. 1 in *Course of Theoretical Physics V* (Pergamon Press, Oxford, 1997).

[32] P. Drude, Ann. Phys. **1**, 566 (1900).

[33] P. Drude, Ann. Phys. **3**, 369 (1900).

[34] R. R. Gerhardts, Z. Physik B **21**, 285 (1975).

[35] T. Ando, A. B. Fowler, and F. Stern, Rev. Mod. Phys. **54**, 437 (1982).

[36] A. Siddiki and R. R. Gerhardts, Phys. Rev. B **70**, 195335 (2004).

[37] D. Shoenberg, *Magnetic Oscillations in Metals* (University Press, Cambridge, 1984).

[38] K. von Klitzing, G. Dorda, and M. Pepper, Phys. Rev. Lett. **45**, 494 (1980).

[39] B. I. Halperin, Phys. Rev. B **25**, 2185 (1982).

[40] M. Büttiker, Phys. Rev. Lett. **57**, 1761 (1986).

[41] M. Büttiker, Phys. Rev. B **38**, 9375 (1988).

[42] E. Ahlswede, P. Weitz, J. Weis, K. von Klitzing, and K. Eberl, Physica B **298**, 562 (2001).

[43] R. W. Winkler, J. P. Kotthaus, and K. Ploog, Phys. Rev. Lett. **62**, 1177 (1989).

[44] C. Zhang and R. R. Gerhardts, Phys. Rev. B **41**, 12850 (1990).

[45] R. R. Gerhardts and C. Zhang, Phys. Rev. Lett. **64**, 1473 (1990).

[46] R. R. Gerhardts and C. Zhang, Surf. Science **229**, 92 (1990).

[47] M. Y. Azbel, Zh. Eksp. Teor. Fiz. **46**, 929 (1964).

[48] M. Kohmoto, Ann. Phys. **160**, 343 (1985).

[49] D. Pfannkuche and R. R. Gerhardts, Phys. Rev. B **46**, 12606 (1992).

[50] J. Zak, Phys. Rev. **134**, A1602 (1964).

[51] J. Zak, Phys. Rev. **134**, A1607 (1964).

[52] Y. Aharonov and D. Bohm, Phys. Rev. **115**, 485 (1959).

[53] N. A. Usov, Zh. Eksp. Theor. Fiz. **94**, 305 (1988), [Sov. Phys. JETP **67**, 2565 (1988)].

[54] G. Wannier, Phys. Stat. Solidi **88**, 757 (1978).

[55] R. R. Gerhardts, D. Pfannkuche, D. Weiss, and U. Wulf, in *High Magnetic Fields in Semiconductor Physics III*, Vol. 101 of *Springer Series in Solid-State Science*, edited by G. Landwehr (Springer-Verlag, Berlin, 1992), p. 359.

[56] J. P. Eisenstein, H. L. Störmer, V. Narayanamurti, A. Y. Cho, A. C. Gossard, and C. W. Tu, Phys. Rev. Lett. **55**, 875 (1985).

[57] S. A. J. Wiegers, L. P. Lévy, M. Y. Simmons, D. A. Ritchie, A. Cavanna, B. Etienne, G. Martinez, and P. Wyder, Phys. Rev. Lett. **79**, 3238 (1997).

[58] T. P. Smith, B. B. Goldberg, and P. J. Stiles, Phys. Rev. B **32**, 2696 (1985).

[59] D. Weiss, K. von Klitzing, and V. Mosser, in *Two-Dimensional Systems: Physics and New Devices*, Vol. 67 of *Springer Series in Solid-State Science*, edited by G. Bauer, F. Kuchar, and H. Heinrich (Springer Verlag, Berlin, 1986), p. 204.

[60] D. Weiss, A. Menschig, K. von Klitzing, and G. Weimann, Surf. Sci. **263**, 314 (1992).

[61] D. J. Thouless, M. Kohmoto, M. P. Nightingale, and M. den Nijs, Phys. Rev. Lett. **49**, 405 (1982).

[62] P. Středa, J. Phys. C **15**, L1299 (1982).

[63] P. Středa, J. Phys. C **15**, L717 (1982).

[64] M. Langenbuch, R. Hennig, M. Suhrke, U. Rössler, C. Albrecht, J. H. Smet, and D. Weiss, Physica E **6**, 565 (2000).

[65] N. W. Ashcroft and N. D. Mermin, *Solid State Physics* (Saunders College, Philadelphia, 1976).

[66] R. W. Stark and L. M. Falicov, Progress Low-Temp. Phys. **5**, 23 (1967).

[67] E. I. Blount, Phys. Rev. **126**, 1636 (1962).

[68] A. B. Pippard, Proc. Roy. Soc. **A270**, 1 (1962).

[69] J. R. Reitz, J. Phys. Chem. Solids **25**, 53 (1964).

[70] A. B. Pippard, Phil. Trans. Roy. Soc. **A265**, 317 (1964).

[71] W. G. Chambers, Phys. Rev. **140**, A135 (1865).

[72] A. B. Pippard, *Magnetoresistance in Metals* (Cambridge University Press, Cambridge, 1989).

[73] H. W. Capel, Physica **42**, 491 (1969).

[74] M. H. Cohen and L. M. Falicov, Phys. Rev. Lett. **7**, 231 (1961).

[75] P. Středa and A. H. MacDonald, Phys. Rev. B **41**, 11892 (1990).

[76] D. Weiss, Physica Scripta **T35**, 226 (1991).

[77] P. H. Beton, E. S. Alves, P. C. Main, L. Eaves, M. Dellow, M. Henini, O. H. Hughes, S. P. Beaumont, and C. D. W. Wilkonson, Phys. Rev. B **42**, 9229 (1990).

[78] P. H. Beton, M. W. Dellow, P. C. Main, E. S. Alves, L. Eaves, S. P. Beaumont, and C. D. W. Wilkonson, Phys. Rev. B **43**, 9980 (1991).

[79] V. Umansky, private correspondence.

[80] A. Piotrowska, A. Guivarch, and G. Pebus, Solid State Elec. **26**, 179 (1983).

[81] K. Tsubaki, H. Sakaki, J. Yoshino, and Y. Sekiguchi, Appl. Phys. Lett. **45**, 663 (1984).

[82] P. M. Mooney, J. Appl. Phys. **67**, R1 (1990).

[83] P. M. Mooney and T. N. Theis, Comments Condens. Matter Phys. **16**, 167 (1992).

[84] S. Chowdhury, C. J. Emeleus, B. Milton, E. Skuras, and A. R. Long, Phys. Rev. B **62**, R4821 (2000).

[85] C. J. Emeleus, B. Milton, A. R. Long, J. H. Davies, D. E. Petticrew, and M. C. Holland, Appl. Phys. Lett. **73**, 1412 (1998).

[86] I. Maximov, A. L. Bogdanov, and L. Montelius, J. Vac. Sci. Technol. B **15**, 2921 (1997).

[87] H. Arlinger, Leybold company, private correspondence.

[88] M. Shayegan, private correspondence.

[89] C. W. J. Beenakker and H. van Houten, in *Solid State Physics*, edited by H. Ehrenreich and D. Turnbull (Academic Press, Boston, 1991), p. 1.

[90] C. J. B. Ford, S. Washburn, M. Büttiker, C. M. Knödler, and J. M. Hong, Phys. Rev. Lett. **62**, 2724 (1989).

[91] D. Weiss, M. L. Roukes, A. Menschig, P. Grambow, K. von Klitzing, and G. Weimann, Phys. Rev. Lett. **66**, 2790 (1991).

[92] C. G. Smith, M. Pepper, R. Newbury, H. Ahmed, D. G. Hasko, D. C. Peacock, J. E. F. Frost, D. A. Titchie, G. A. C. Jones, and G. Hill, J. Phys.: Condensed Matter **2**, 3405 (1990).

[93] R. Ketzmerick, R. Fleischmann, and T. Geisel, Europhys. Lett. **3**, 219 (1994).

[94] H. Aoki, Surf. Sci. **263**, 137 (1992).

[95] M. Koshino and T. Ando, to be published (unpublished).

[96] H. J. Schellnhuber and G. M. Obermair, Phys. Rev. Lett. **45**, 276 (1980).

[97] G. M. Obermair and H. J. Schellnhuber, Phys. Rev. B **23**, 5185 (1981).

[98] G. M. Obermair, H. J. Schellnhuber, and A. Rauh, Phys. Rev. B **23**, 5191 (1981).

[99] I. Dana, Y. Avron, and J. Zak, J. Phys. C **18**, L679 (1985).

[100] J. E. Avron and L. G. Yaffe, Phys. Rev. Lett. **56**, 2084 (1986).

[101] M. Langenbuch, private correspondence.

[102] R. W. Stark and C. B. Friedberg, J. Low Temp. Phys. **14**, 111 (1974).

[103] R. W. Stark and C. B. Friedberg, J. Low Temp. Phys. **14**, 175 (1974).

[104] D. Morrison and R. W. Stark, J. Low Temp. Phys. **45**, 581 (1981).

[105] N. B. Sandesara and R. W. Stark, Phys. Rev. Lett. **53**, 1681 (1984).

[106] R. G. Chambers, Phys. Rev. Lett. **5**, 3 (1960).

[107] E. H. Lieb, Phys. Rev. Lett. **62**, 1201 (1989).

[108] C. W. J. Beenakker, Phys. Rev. Lett. **62**, 2020 (1989).

[109] R. R. Gerhardts and S. D. M. Zwerschke, Phys. Rev. B **64**, 115322 (2001).

[110] R. R. Gerhardts, Phys. Rev. B **45**, 3449 (1992).

[111] R. R. Gerhardts, Phys. Rev. B **53**, 11064 (1996).

[112] S. D. M. Zwerschke and R. R. Gerhardts, Physica B **298**, 353 (2001).

[113] D. E. Grant, A. R. Long, and J. H. Davies, Phys. Rev. B **61**, 13127 (2000).

[114] Y. Paltiel, D. Mahalu, H. Shtrikman, G. Bunin, and U. Meirav, Semicond. Sci. Technol. **12**, 987 (1997).

[115] S. Chowdhury, A. R. Long, E. Skuras, C. J. Emeleus, and J. H. Davies, Journal of the Korean Phys. Soc. **39**, 529 (2001).

[116] R. Menne and R. R. Gerhardts, Phys. Rev. B **57**, 1707 (1989).

[117] A. D. Mirlin and P. Wölfle, Phys. Rev. B **58**, 12986 (1998).

[118] J. Groß and R. R. Gerhardts, Phys. Rev. B **66**, 155321 (2002).

[119] I. A. Larkin and J. H. Davies, Phys. Rev. B **56**, 15242 (1997).

[120] J. H. Davies, D. E. Petticrew, and A. R. Long, Phys. Rev. B **58**, 10789 (1998).

[121] V. Numerics, *PV-Wave Command Language, Reference Volume 1* (Visual Numerics, Houston, Texas, 1993).

[122] E. O. Brigham, *The fast Fourier transform* (Prentice-Hall, Englewood Cliffs, New Jersey, 1974).

[123] V. Cizek, *Discrete Fourier transforms and their applicatios* (Adam Hilger, Bristol, England, 1986).

[124] R. Gerhardts, private correspondence.

[125] S. D. Sarma and F. Stern, Phys. Rev. B **32**, 8442 (1985).

[126] J. P. Harrang, R. J. Higgins, R. K. Goodall, P. R. Jay, M. Laviron, and P. Delescluse, Phys. Rev. B **32**, 8126 (1985).

Acknowledgments

Although a few words do not do justice to their contribution I would like to thank the following people for making this work possible.

- Prof. Dr. K. von Klitzing, for welcoming me into his group, the interest in the progress and results of this work, the good working environment and the financial support.

- Dr. J. H. Smet, my direct supervisor, for introducing me to the field of modulated 2D electron gases, giving me the chance to work independently, his numerous suggestions during the course of this work and the critical reading of the manuscript.

- Prof. Dr. M. Dressel, who kindly agreed to co-advise this thesis.

- Dr. V. Umansky (Weizmann Institute of Science, Israel) for supplying his high quality heterostructures which are the foundation for the present work.

- Dr. S. Ilani (Weizmann Institute of Science) and T. Reindl for ideas which improved the sample quality, M. Riek for help during the Hall bar fabrication, H. Gräbeldinger (IV Physikalisches Institut, Universität Stuttgart) and U. Waizmann for the high quality electron beam lithography.

- Dr. C. Albrecht for the introduction to cryogenic measurements at the institute.

- Dr. S. Chowdhury for inspiring me to finish the work on rectangular lattices.

- J. Meyer for the AFM images of samples with etched rectangular lattices.

- Prof. Dr. R. Ketzmerick (Computational Physics Group, Technical University Dresden) and B. Naundorf (Max-Planck Institute for Dynamics and Self-Organization, Göttingen) for their calculation of the Hofstadter spectrum for the Landau band coupled case.

- Prof. Dr. R. R. Gerhardts for being always open to discussions, estimating the modulation amplitudes and for his magnetotransport calculations of rectangular lattices.

- Dr. M. Langenbuch (Institut für Theoretische Physik, Universität Regensburg), for calculating the miniband structure under investigation.

- Dr. M. Grayson (Walter Schottky Institute, Munich), for providing crucial help, especially when it came to improvements in my oral presentations.

- Dr. J. Gross, Dr. S. Kraus and the EDV-Team for answering my numerous questions on Linux, as did Dr. U. Wilhelm and Dr. J. Schmid also with regard to Measkern.

- Dr. E. Ahlswede, Dr. M. Mayr, Dr. S. Bayrakci and Dr. O. Stern for a critical reading of the manuscript.

- and last but not least, all my friends and fellow PhD students in Stuttgart who have immeasurably improved the quality of my social life.

- My girlfriend Franziska Koch, for being patient with me during the final stage of this thesis and for commenting on the manuscript.

- My parents Ingrid and Dr. Wolfgang Geisler, for their neverending love and support.

Curriculum Vitae

Name	Martin Christoph Geisler
Geboren am	9. April 1973
Geburtsort	Viersen

9/1983 - 6/1992	Theodor-Heuss-Gymnasium in Radevormwald, Abitur
10/1992 - 5/1997	Studium der Physik an der Ruhr-Universität Bochum
9/1994 - 7/1995	Erasmus-Stipendium an der University of Sussex, Brighton, England
seit 2/1996	Stipendiat der Studienstiftung des deutschen Volkes
4/1996 - 5/1997	Diplomarbeit bei Prof. Dr. G. Wunner, Lehrstuhl Theoretische Physik I, Ruhr-Universität Bochum
6/1997	Diplom in Physik
6/1997- 8/1997	Wissenschaftlicher Mitarbeiter am Lehrstuhl Theoretische Physik I, Ruhr-Universität Bochum
9/1997-10/1998	Gastwissenschaftler in der Nano-Electronics Group von Prof. Dr. T. Sugano und Prof. Dr. Y. Aoyagi am Riken (Institut für physikalische und chemische Forschung), Japan
seit 11/1998	Anfertigung der vorliegenden Dissertation am Max-Planck Institut für Festkörperforschung, Stuttgart, Abteilung Prof. Dr. K. von Klitzing